

Properties of Mars' Dayside Low-Altitude Induced Magnetic Field and Comparisons with Venus

Susanne Byrd¹, Zachary Girazian², and Suranga Ruhunusiri¹

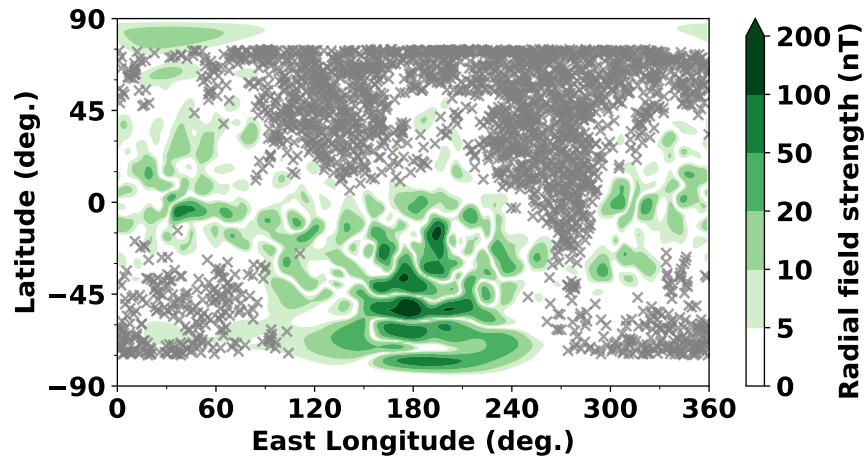
¹University of Iowa

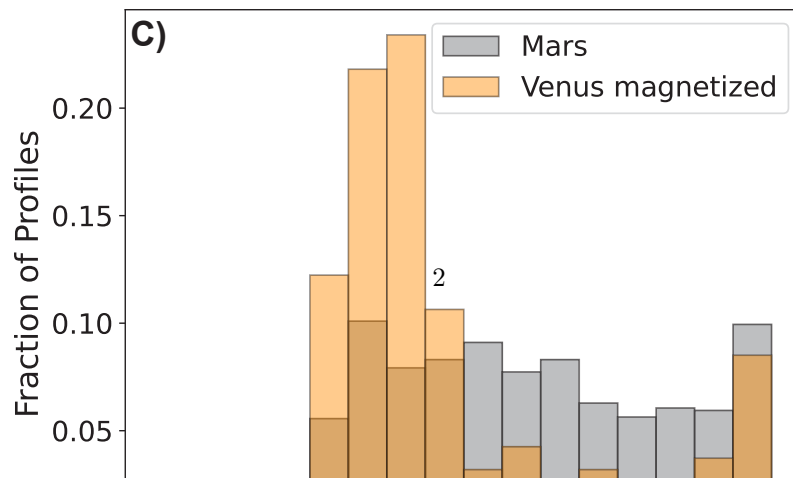
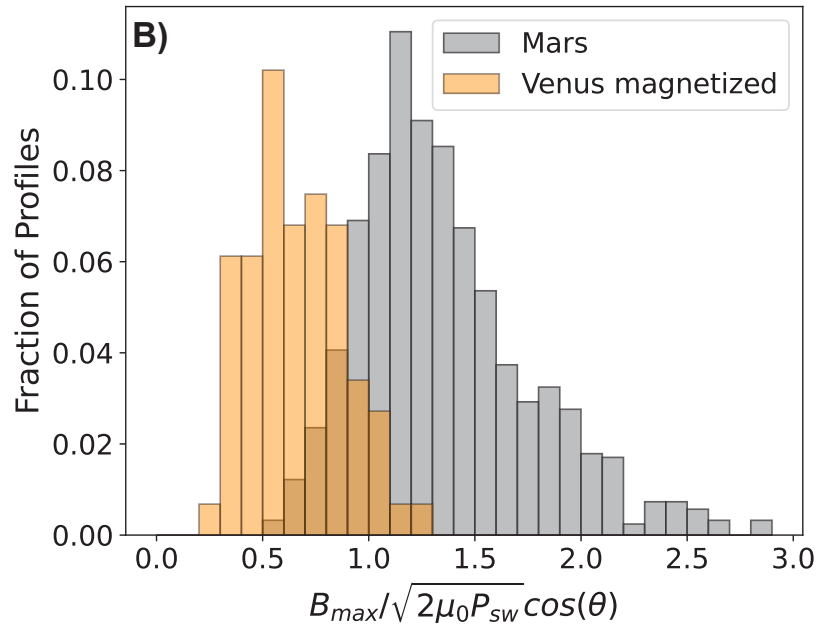
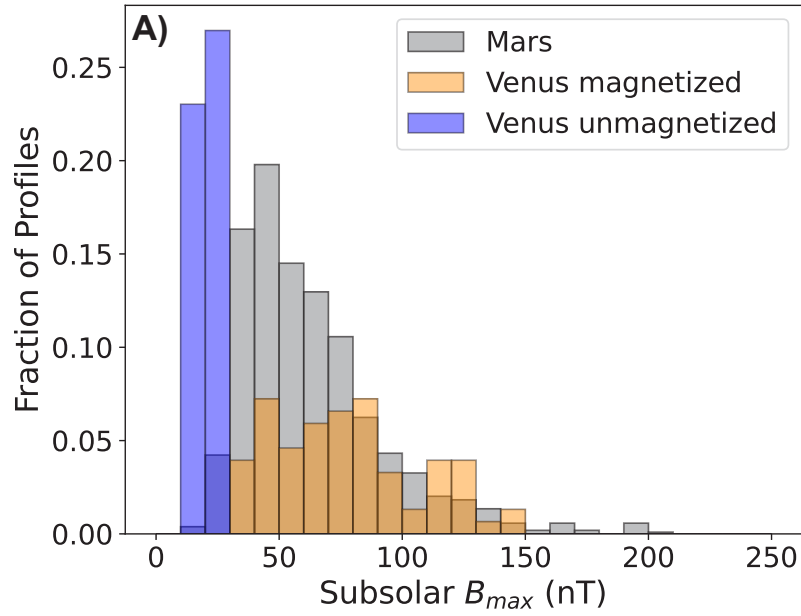
²The University of Iowa

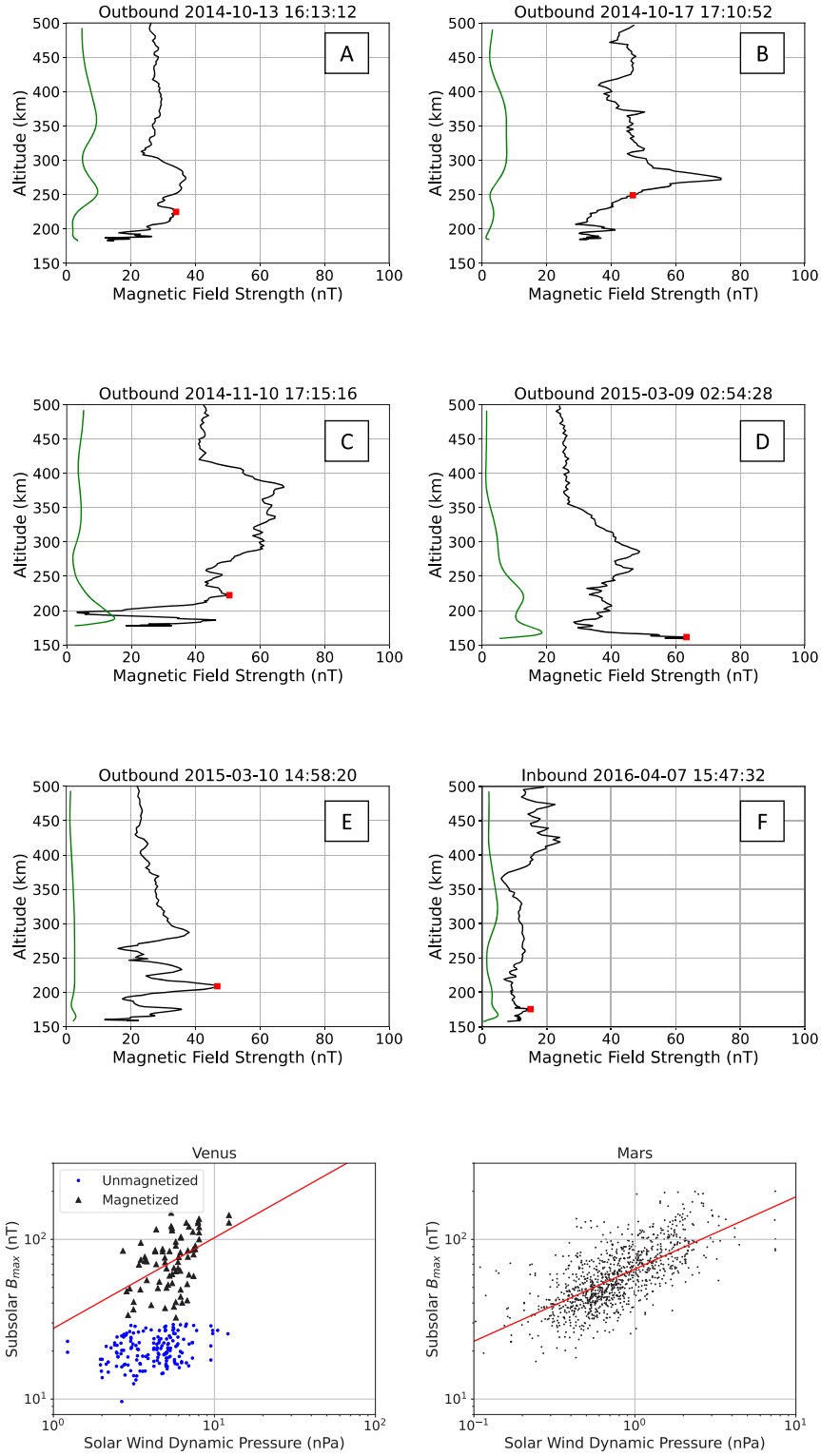
December 27, 2023

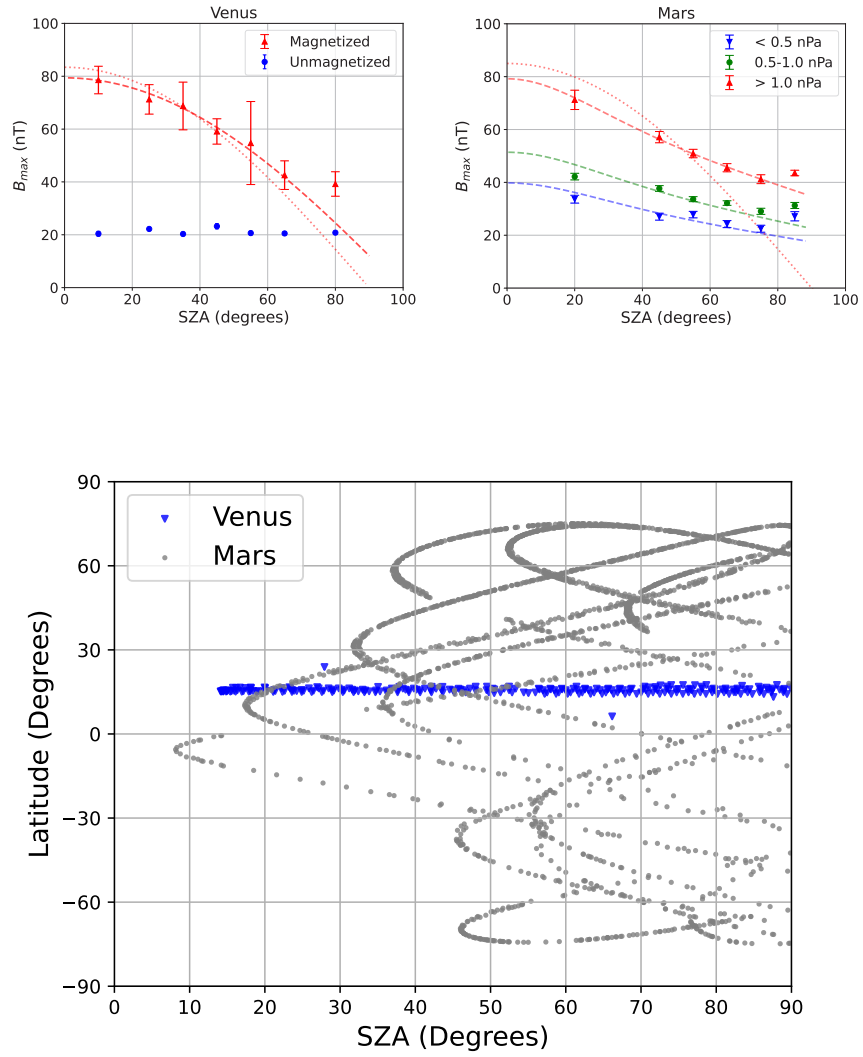
Abstract

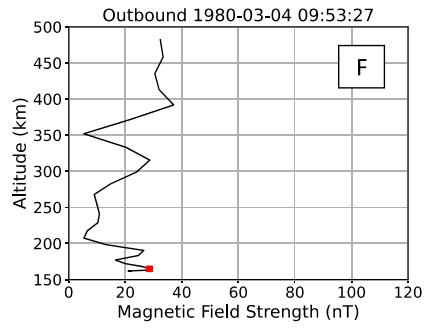
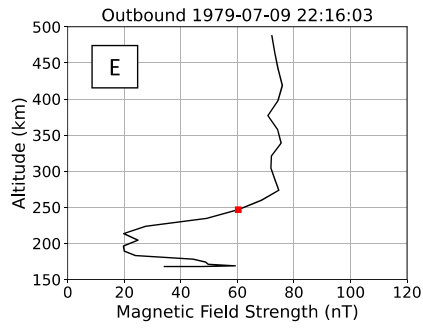
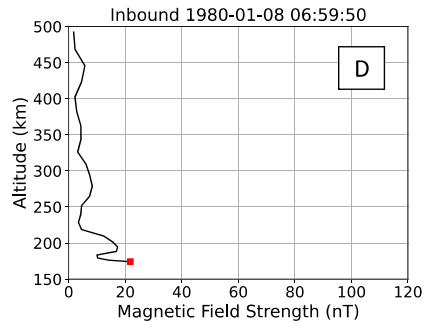
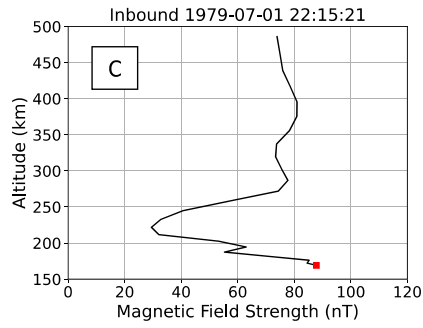
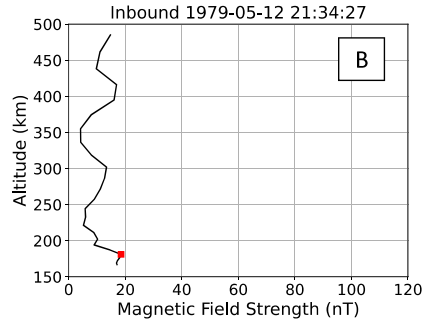
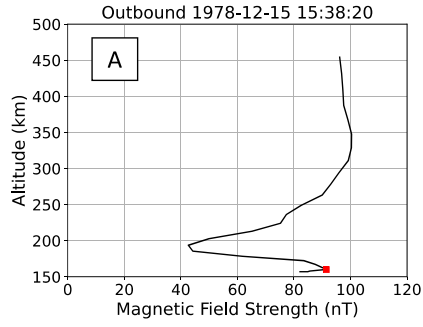
Mars and Venus have atmospheres but lack large-scale intrinsic magnetic fields. Consequently, the solar wind interaction at each planet results in the formation of an induced magnetosphere. Our work aims to compare the low-altitude (< 250 km) component of the induced magnetic field at Venus and Mars using observations from Pioneer Venus Orbiter (PVO) and Mars Atmosphere and Volatile Evolution (MAVEN). The observations from Mars are restricted to regions of weak crustal magnetism. At Venus, it has long been known the vertical structure of the induced magnetic field profiles have recurring features that enable them to be classified as either magnetized or unmagnetized. We find the induced field profiles at Mars are more varied, lack recurring features, and are unable to be classified in the same way. The solar zenith angle dependence of the low-altitude field strength at both planets is controlled by the shape of the magnetic pileup boundary. Also, because the ionospheric thermal pressure at Venus is often comparable to the solar wind dynamic pressure, the induced fields are weaker than required to balance the solar wind by themselves. By contrast, induced fields at Mars are stronger than required to achieve pressure balance. Lastly, we find the induced fields in the magnetized ionosphere of Venus have a weaker dependence on solar wind dynamic pressure than the induced fields at Mars. Our results point to planetary properties, such as planet-Sun distance, having a major effect on the properties of induced fields at nonmagnetized planets.











Properties of Mars' Dayside Low-Altitude Induced Magnetic Field and Comparisons with Venus

Susanne Byrd¹, Zachary Girazian¹, Suranga Ruhunusiri²

¹Department of Physics and Astronomy, University of Iowa, Iowa City, IA

²Laboratory for Atmospheric and Space Physics, University of Colorado, Boulder, Boulder, CO, USA

Key Points:

- Unlike Venus, the induced magnetic field profiles at Mars are unable to be categorized into magnetized and unmagnetized states.
- At both planets, the solar zenith angle dependence of the induced field strength is controlled by the shape of the magnetic pileup boundary.
- Induced fields at Mars are stronger than expected if assuming the fields form to achieve pressure balance with the oncoming solar wind.

Corresponding author: Susanne Byrd, susbyrd@uiowa.edu

Abstract

Mars and Venus have atmospheres but lack large-scale intrinsic magnetic fields. Consequently, the solar wind interaction at each planet results in the formation of an induced magnetosphere. Our work aims to compare the low-altitude (< 250 km) component of the induced magnetic field at Venus and Mars using observations from Pioneer Venus Orbiter (PVO) and Mars Atmosphere and Volatile Evolution (MAVEN). The observations from Mars are restricted to regions of weak crustal magnetism. At Venus, it has long been known the vertical structure of the induced magnetic field profiles have recurring features that enable them to be classified as either magnetized or unmagnetized. We find the induced field profiles at Mars are more varied, lack recurring features, and are unable to be classified in the same way. The solar zenith angle dependence of the low-altitude field strength at both planets is controlled by the shape of the magnetic pileup boundary. Also, because the ionospheric thermal pressure at Venus is often comparable to the solar wind dynamic pressure, the induced fields are weaker than required to balance the solar wind by themselves. By contrast, induced fields at Mars are stronger than required to achieve pressure balance. Lastly, we find the induced fields in the magnetized ionosphere of Venus have a weaker dependence on solar wind dynamic pressure than the induced fields at Mars. Our results point to planetary properties, such as planet-Sun distance, having a major effect on the properties of induced fields at nonmagnetized planets.

1 Introduction

A magnetosphere is a region of space around a planetary body where charged particles are deflected by the body's magnetic field. For bodies with active intrinsic field generation, this region is usually large (e.g., ~ 10 planetary radii on the sun-facing side for Earth). For bodies without active intrinsic field generation, this region is smaller (< 1 planetary radii) and an induced magnetosphere forms as the magnetic field of the solar wind interacts with the electrically conductive ionosphere (Bertucci et al., 2011). As it encounters the obstacle, an electric current is induced in the ionosphere (Daniell Jr & Cloutier, 1977; Ramstad, 2020). The induced magnetosphere that results from this interaction tends to balance the dynamic pressure from the oncoming solar wind (Luhmann et al., 2004). Typically, an induced field is much weaker than an intrinsic global field. Induced magnetospheres occur on bodies that have an atmosphere but lack a dynamo-generated global magnetic field. Both Venus and Mars fall into this category as unmagnetized planets containing atmospheres, and thus both planets have induced magnetospheres. In this paper, we focus on understanding and comparing the structure and variability of the low-altitude (< 250 km) induced magnetic fields of Venus and Mars.

The Pioneer Venus Orbiter (PVO) is the only spacecraft to have consistently measured the low-altitude induced magnetic fields at Venus. Analyses of the PVO data confirmed that Venus has a magnetic field induced solely by interaction with the solar wind (Luhmann & Russell, 1983). They also found most vertical profiles of the induced magnetic field strength can, based on their features, be classified as either magnetized or unmagnetized (Luhmann et al., 1980; Luhmann & Cravens, 1991). When the solar wind pressure exceeds the peak ionospheric thermal pressure, the planet's induced field is classified as being in a magnetized state. In the magnetized state, the vertical profile contains a local minimum near 200 km and a local maximum near 170 km with peak field strengths up to 150 nT. Alternatively, when the solar wind pressure is less than the peak ionospheric thermal pressure, the ionosphere is in an unmagnetized state (Luhmann & Cravens, 1991). In the unmagnetized state, the ionosphere excludes most of the external field and the low-altitude induced field strength is weaker (< 30 nT). These profiles lack distinct maxima or minima at low altitudes, but instead contain many small-scale (~ 10 km) spikes characterized as flux ropes (Elphic et al., 1980; Phillips et al., 1984a; Elphic & Russell, 1983).

Some basic characteristics of the low-altitude field strengths in the magnetized ionosphere of Venus have also been reported. The low-altitude field strength was found to decrease with increasing solar zenith angle (SZA) (Luhmann & Cravens, 1991). Additionally, the field strength was found to increase with increasing solar wind dynamic pressure (Luhmann et al., 1980; Kar & Mahajan, 1987). Both of these variations are expected if pressure balance is satisfied across the near-space environment and the induced field is required to balance the dynamic pressure of the oncoming solar wind (Luhmann & Cravens, 1991; Sánchez-Cano et al., 2020). Starting in the pristine solar wind and moving inward, the dominant pressure terms are as follows: the dynamic pressure in the solar wind, the plasma thermal pressure in the sheath, the magnetic pressure in the magnetic pileup region, and the sum of the plasma thermal pressure and induced magnetic pressure below the magnetic pileup boundary. Essentially, the perpendicular component of the solar wind dynamic pressure is ultimately converted into magnetic pressure in the magnetic pileup region.

Mars Global Surveyor (MGS) provided the first comprehensive magnetic field measurements at Mars, discovering the total field is a combination of induced fields and crustal fields that are scattered across the planet (Connerney et al., 2001; Brain, 2003). However, MGS was unable to measure the induced magnetic field at low altitudes. Arriving at Mars in 2014, the Mars Atmosphere and Volatile EvolutioN (MAVEN) mission became the first spacecraft to routinely measure low-altitude magnetic fields. Recently, Fang et al. (2023) analyzed low-altitude magnetic field data from MAVEN. They found the induced field strength on the dayside is usually around 15-50 nT, decreases with increasing SZA, and increases with increasing solar wind dynamic pressure. Huang et al. (2023) found the vertical profiles often resemble a reversed “L”: above ~ 200 km the field has a constant value, and below ~ 200 km the field abruptly decreases in strength. Several studies have also examined the ubiquitous small scale features (10-50 km) present in the observed magnetic field profiles, including waves, slabs, flux ropes, and flux tubes (Hamil et al., 2022; Bowers et al., 2021; Cravens et al., 2023). These structures are thought to form through a variety of processes such as variations in the upstream solar wind, global plasma dynamics, and plasma instabilities.

Models have been used in attempt to reproduce the observed low-altitude magnetic field profiles at both planets. For Venus, models from the PVO era (Cloutier, 1984; Cravens et al., 1984; Luhmann et al., 1984; Shinagawa & Cravens, 1988; Luhmann & Cravens, 1991) and more recent iterations (Y. Ma et al., 2020, 2023), have been quite successful at reproducing the observed large-scale magnetic fields present in the magnetized ionosphere. They are able to reproduce several features of the magnetized profiles, including the local minimum near 200 km and the local maximum near 170 km (Cravens et al., 1984; Phillips et al., 1984b; Cloutier, 1984; Shinagawa & Cravens, 1988). Similar models for the induced field at Mars have been somewhat successful at reproducing the observed profiles (Shinagawa & Cravens, 1989; Y. J. Ma et al., 2017; Fang et al., 2018; Huang et al., 2023). Generally, however, the observed induced field profiles at Mars have more small-scale features that models are unable to fully reproduce.

In these models, the evolution of the induced magnetic field, B_{ind} , is described by the magnetic diffusion equation (Luhmann & Cravens, 1991):

$$\frac{\partial B_{ind}}{\partial t} = \nabla \times (u \times B_{ind}) - \nabla \times (\eta_m \nabla \times B_{ind}) \quad (1)$$

where t is time, u is the plasma flow speed, and η_m is the magnetic diffusivity. The first term in Equation 1 represents the convection of magnetic flux with plasma flow. The second term represents the diffusion or dissipation of the magnetic field as the electrical currents associated with the field are dampened through collisions (Luhmann & Cravens, 1991). At the top of the ionosphere, which is sometimes called the magnetic pileup bound-

ary or ionopause (Espley, 2018), densities are so low that the first term dominates and the draped solar wind field is convected into the ionosphere by downward flowing plasma. As the field is convected downward, the diffusion term eventually takes over as increased ion-neutral collisions between the induced current and neutral molecules causes the field to dissipate. The vertical structure of the induced magnetic field profile is, to first order, controlled by these processes. An interesting aspect of this picture is that variations in upstream solar wind conditions, such as a change in dynamic pressure, will not have an immediate affect in the low-altitude induced field because the effects take time to propagate through the sheath and into the ionosphere (Luhmann et al., 1984; Y. Ma et al., 2020; Hamil et al., 2022; Cravens et al., 2023).

In this work, our aim is to compare the structure and variability of the low-altitude induced magnetic fields at Venus and Mars. Our focus is on large scale structures as opposed to the small-scale structures like flux ropes. Our primary goals are to (1) investigate if the vertical structure of the induced magnetic field profiles at Mars can, like at Venus, be classified as magnetized or unmagnetized; (2) compare the induced field strengths at each planet and investigate if they are consistent with pressure balance, and (3) determine if the low-altitude induced magnetic field strengths vary with SZA and solar wind dynamic pressure in similar ways.

2 Data and Method

2.1 Pioneer Venus Orbiter

PVO collected the bulk of its low-altitude in situ measurements between December 1978 and July 1980 when its orbital period was 24 hours, and periapsis altitude was maintained near 160 km for nearly 700 orbits (Brace & Kliore, 1991). During this time, the periapsis segment evolved to cover a wide range of local times and solar zenith angles, but stayed near mid-latitudes throughout (10°S-40°N).

For magnetic field data, we use the low resolution magnetometer (OMAG) observations that have 12-second time resolution (C. T. Russell et al., 1980). The files contain the magnetic field vector, spacecraft altitude, solar zenith angle, and latitude of each observation. Each orbit is split into an inbound and outbound segment and the observations are trimmed to only include altitudes below 500 km. For upstream solar wind data, we use the upstream measurements from PVO that were obtained when PVO was located outside the bow shock. The IMF vector was measured by OMAG and the solar wind density and velocity were measured by the Plasma Analyzer instrument (Intriligator et al., 1980). The data are provided as hourly averages but we assign a single value to each half-orbit (inbound and outbound) by taking the solar wind measurement closest in time to the low-altitude magnetic field (periapsis) measurement. Periapsis segments without a solar wind measurement within 10 hours were not included. The dataset provides solar wind proton densities and velocities from which we calculate the dynamic pressure using $P_{sw} = \rho V^2$ where P_{sw} is the solar wind dynamic pressure, ρ is the solar wind mass density, and V is the bulk flow velocity.

2.2 MAVEN

The Mars low-altitude in situ measurements cover October 2014 through August 2020 when MAVEN's orbital period was 4.5 hours and periapsis altitude varied between \sim 150-200 km. A handful of the observations come from times when periapsis was lowered down to \sim 125 km for week-long “deep dip” campaigns (Jakosky et al., 2015). The location of MAVEN's periapsis segment slowly evolves throughout the mission, covering a wide range of latitudes, local times, and SZAs. For magnetic field data, we use the Key Parameter (KP) data products. The KP data are a bundle that includes measurements from every MAVEN in situ instrument along with spacecraft ephemeris informa-

163 tion, all on a uniformly sampled 4-second time grid. The KP files are compiled from the
 164 instrument’s fully calibrated Level 2 data products. As with the Venus data, each or-
 165 bit is split into an inbound and outbound segment and trimmed to only include obser-
 166 vations at an altitude below 500 km.

167 For solar wind data, we use observations from MAVEN’s Magnetometer (MAG)
 168 and Solar Wind Ion Analyzer (SWIA) that were obtained while MAVEN was outside the
 169 bowshock. The data are derived using the method described in (Halekas et al., 2017),
 170 which provides averages of solar wind properties for each orbit. The SWIA observations
 171 contain the solar wind proton density and velocity which are used to calculate the so-
 172 lar wind dynamic pressure. Periapsis segments without a solar wind measurement within
 173 10 hours were not included. However, many of the orbits do not have upstream solar wind
 174 measurements within 10 hours of the periapsis observations. To fill these gaps, we use
 175 the Ruhunusiri et al. (2018) solar wind proxy model, which predicts upstream solar wind
 176 conditions based on MAVEN observations in the sheath. Of the 2625 MAVEN profiles
 177 in the final dataset, 1151 were assigned upstream conditions based on SWIA observa-
 178 tions, 1069 were assigned from the proxy model, and 405 could not be assigned.

179 **2.3 Caveats**

180 When comparing results derived from the MAVEN and PVO observations, several
 181 differences between the two datasets must be considered. First, the PVO data were ob-
 182 tained during the maximum of Solar Cycle 21 (Brace & Kliore, 1991), while the MAVEN
 183 data were obtained during the declining phase of the rather weak Solar Cycle 24 (Lee
 184 et al., 2017). Second, the PVO periapsis is confined to mid-latitudes, while the MAVEN
 185 periapsis covers latitudes between 75° N and 75° S (see Figure 1). Additionally, because
 186 the spacecraft moves both vertically and horizontally during each periapsis pass, the struc-
 187 tures we observe in the magnetic field profiles may not strictly be in the vertical direc-
 188 tion.

189 Differences between the planets themselves must also be kept in mind when com-
 190 paring results from the two planets. For example, Mars has rather pronounced seasons
 191 due to its eccentric orbit and 25° axial tilt, while Venus has no seasons because of its cir-
 192 cular orbit and $< 3^\circ$ axial tilt. Other differences to consider include, but are not lim-
 193 ited to, planetary rotation rate, the presence of crustal magnetic fields at Mars but not
 194 Venus, planetary size, and planet-Sun distance.

195 **2.4 Method**

196 The vertical structure of the induced magnetic field profiles at Venus can gener-
 197 ally be categorized into one of two states: ”magnetized” or ”unmagnetized”. We cate-
 198 gorize the Venus profiles in this manner based on the descriptions in Luhmann and Cravens
 199 (1991). If the global minimum of a trimmed magnetic field profile is below 300 km, and
 200 the profile has low-altitude (< 250 km) maximum field strength greater than 30 nT, it
 201 is classified as magnetized. If a profile has a low-altitude magnetic field strength greater
 202 than 50 nT, it is also classified as magnetized. Alternatively, If a profile has a low-altitude
 203 maximum field strength less than 30 nT, it is classified as unmagnetized. A small num-
 204 ber of profiles remain categorized because they do not match either criteria.

205 Figure 3 shows six examples of Venus magnetic field profiles observed by PVO. The
 206 examples in the left column show magnetized profiles. They contain a peak below 200
 207 km, a wide minimum near 200-250 km, and a nearly-constant topside. These features
 208 are all absent in unmagnetized profiles, examples of which are shown in the right col-
 209 umn of Figure 3. Instead, the unmagnetized profiles are nearly featureless, lacking dis-
 210 tinct maxima or minima, and have weaker field strengths at nearly all altitudes.

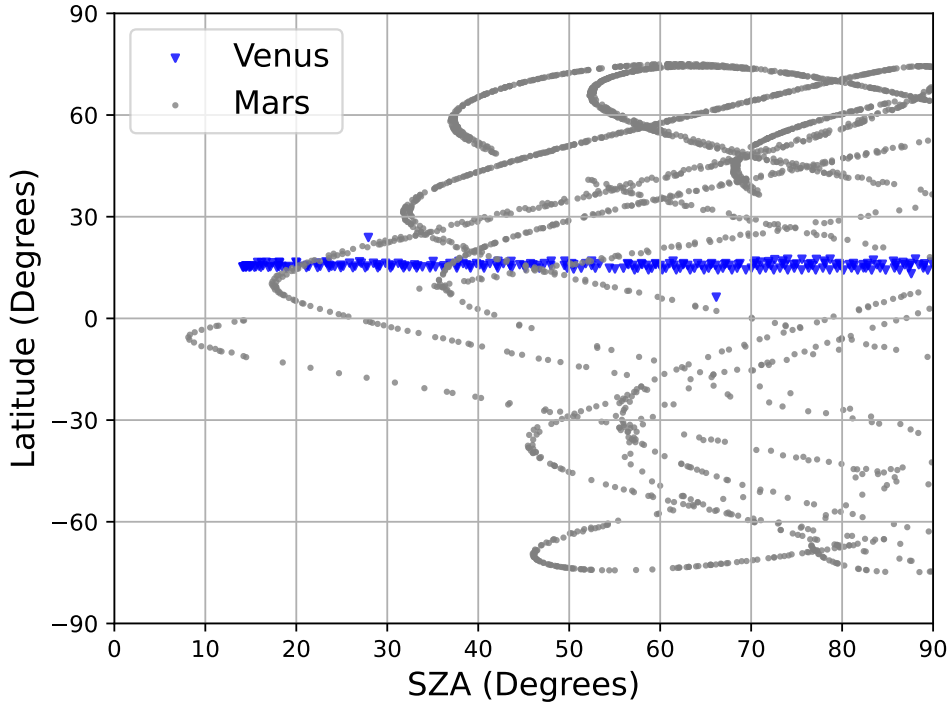


Figure 1: The latitudes and solar zenith angles at periapsis for the orbits used in this study, demonstrating the observational coverage of PVO (blue triangles) and MAVEN (gray circles) are quite different.

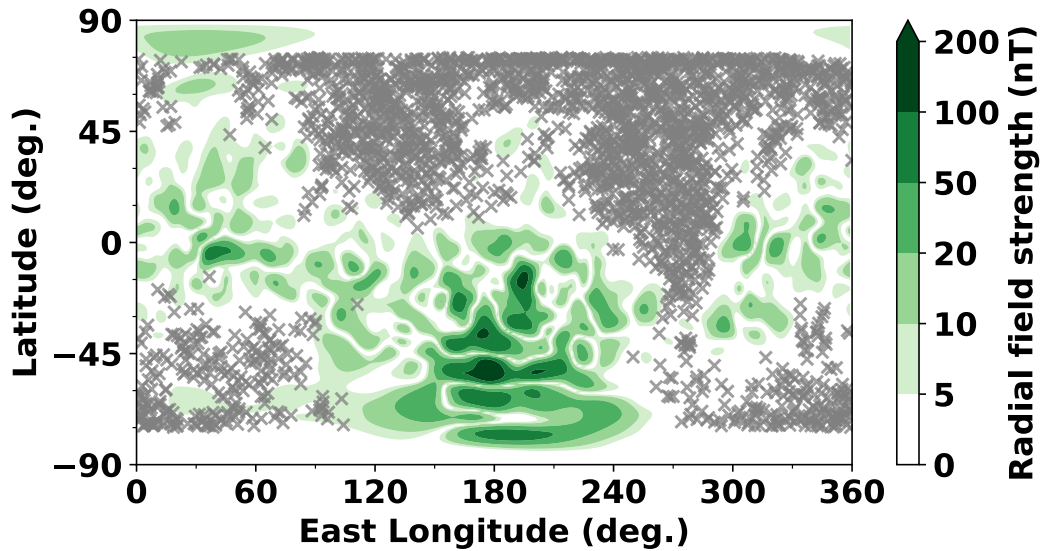


Figure 2: Locations of the MAVEN observations used in our analysis. Grey X's show locations of low-altitude maximum magnetic field strengths (B_{max}) for each inbound and outbound profile. Green contours are a map of the Martian radial crustal field strength at 400 km (Morschhauser et al., 2014). These locations are chosen because they are from weak crustal field regions, making them more comparable to Venus.

Figure 4 shows six examples of magnetic field profiles observed by MAVEN. These profiles are much more complicated than profiles from Venus and they lack recognizable features that would allow them to be sorted easily into two categories. This issue will be explored further in Section 3.1.

Since we are interested in comparing the strength and variability of the low-altitude induced fields at Venus and Mars, we focus our analysis on the maximum magnetic field strength below 250 km altitude (B_{max}). To derive B_{max} for both inbound and outbound segments of an orbit, we locate the maximum field strength below 250 km. This altitude cutoff of 250 km was chosen because it will capture the low-altitude peaks around 170 km in the magnetized profiles at Venus (Luhmann & Cravens, 1991), and be flexible enough to capture peaks in the Mars profiles at a wide range of altitudes. The B_{max} derived from each Venus profile is marked in Figure 3. For magnetized profiles, B_{max} is the field strength at the location of the low-altitude peak near 170 km. For unmagnetized profiles, B_{max} is the maximum field strength below 250 km, but is not at the location of any specific feature. The same method is used to extract B_{max} from the Mars profiles, which are marked in Figure 4. Since the vertical structure varies much more from profile to profile, the derived B_{max} is not extracted from a recurring distinct feature, as in the case of the magnetized Venus profiles.

We note that there are several cases when the location of the derived B_{max} is either at the bottom of the profile (periapsis) or at the top of the profile (near the top altitude cutoff of 250 km). For cases when the derived B_{max} is near the top of the profile, the low-altitude field strength never exceeds the field strength at 250 km. Examples of this case can be seen in Figures 3E and 4B. For these, B_{max} is likely overestimated because our method does not pick any low-altitude feature that has a local maximum below 250 km. For cases when B_{max} is near periapsis, the derived B_{max} likely underestimates the true local maximum in the low-altitude magnetic field profile because the true maximum may reside below periapsis where there are no observations. Examples of this case can be seen in Figure 3C and 4D. With these caveats in mind, we include these cases in our final dataset.

Another important consideration is the crustal magnetic fields at Mars that are not at Venus. We wish to remove these crustal fields from our analysis to enable a more direct comparison between the two planets, focusing solely on the induced component of the magnetic field. The Morschhauser et al. (2014) empirical model of crustal magnetic field strength is used to omit MAVEN observations where the crustal field strength is comparable to the induced field strength. More concretely, we exclude any profiles that have $B_{crust}/B_{max} > 0.2$ where B_{crust} is the crustal field strength at the location of B_{max} . Figure 2 shows the locations of B_{max} that remain after applying this crustal field filtering. It demonstrates the chosen B_{max} 's are confined to outside the crustal field regions.

To focus on the dayside interaction region, in our final dataset we only use profiles that have B_{max} at $SZA < 90^\circ$. In total, the final filtered dataset for Venus includes 475 magnetic field profiles of which 188 are categorized as magnetized, 260 as unmagnetized, and 27 as uncategorized. Of the 188 magnetized profiles, 39 have B_{max} at the bottom of the profile and 25 have B_{max} at the top altitude cutoff of 250 km. Of the 260 unmagnetized profiles, 6 have B_{max} at the bottom of the profile and 30 have B_{max} at 250 km. The final filtered dataset for Mars includes 2625 profiles. Of these, 220 have B_{max} at the bottom of the profile and 112 have B_{max} at the top altitude cutoff of 250 km.

3 Analysis

3.1 Categorizing the Magnetic Field Profiles

As discussed in Section 2.4 and shown in Figure 3, the induced magnetic field profiles at Venus have recurring vertical structures that can generally be categorized as ei-

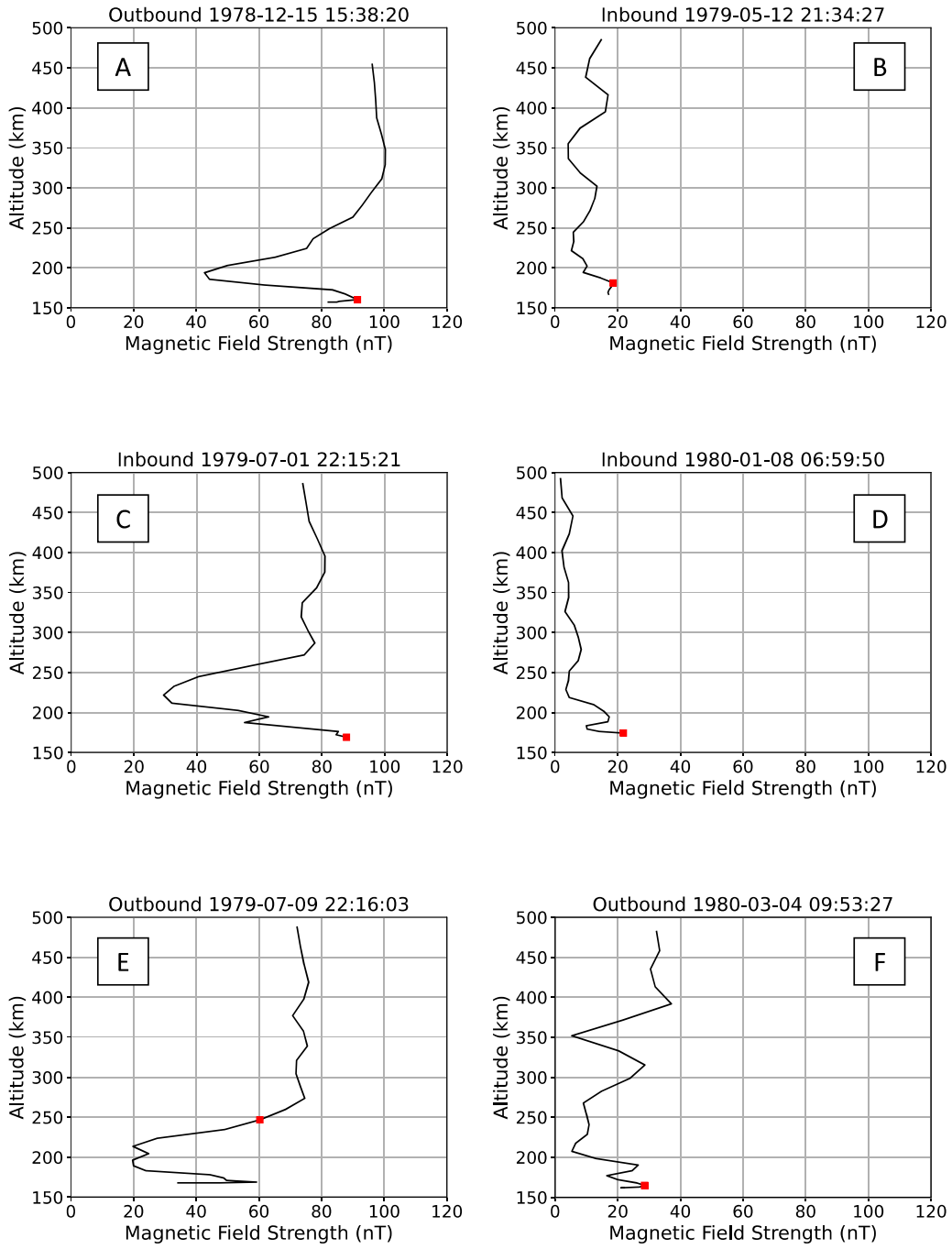


Figure 3: Examples of magnetic field profiles from Venus with magnetized states in the left column and unmagnetized states in the right column. The squares mark the derived B_{max} for each profile.

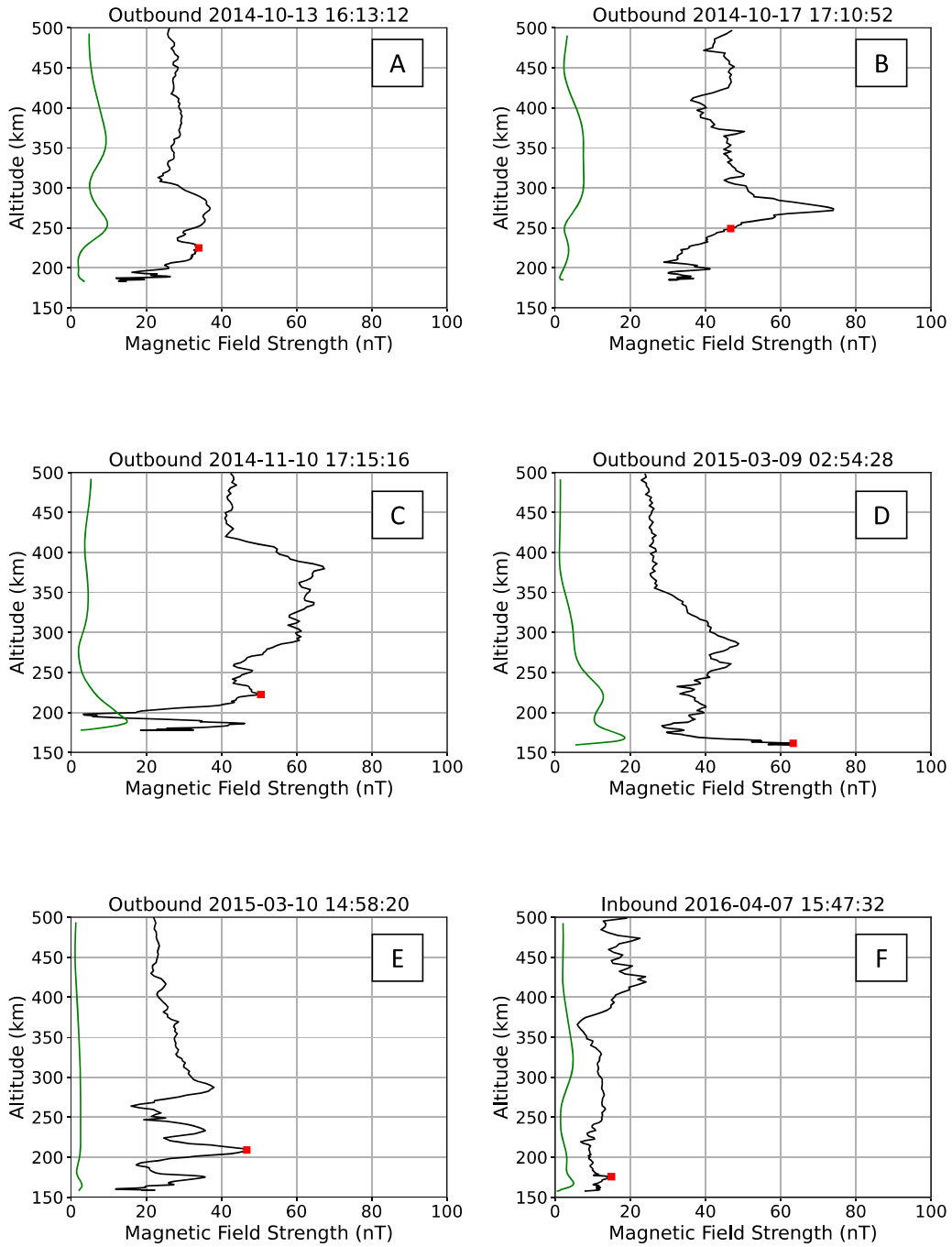


Figure 4: Examples of magnetic field profiles from Mars. The black lines are the measured magnetic field from MAVEN and the green lines are the crustal magnetic field strength from the Morschhauser et al. (2014) crustal field model. The red squares mark the derived B_{max} for each profile.

ther “magnetized” or “unmagnetize” (Luhmann & Cravens, 1991). Using our classification criteria, we find $\sim 40\%$ of the profiles can be classified as magnetized and $\sim 55\%$ can be classified as unmagnetized. These percentages are loosely consistent with the occurrence rates reported by Luhmann et al. (1980), who categorized 30% as magnetized and 70% as unmagnetized. However, they used somewhat different classification criteria.

We attempted to categorize the Mars profiles based on visual inspection but quickly found they could not be categorized into Venus-like magnetized and unmagnetized vertical structures. This is demonstrated in Figure 4, which shows the Mars profiles lack distinct features that would enable them to be easily categorized. In particular, they lack a consistent minimum near 300 km or a clear single low-altitude peak, features that are present in the Venus magnetized profiles. Instead, the Mars profiles are more varied and have more complex small-scale structures (tens of kilometers). These structures are present even when the crustal field component is much lower than induced field strength.

We conclude the vertical structure of the induced magnetic fields at Mars are too varied to be classified into simple magnetized and unmagnetized states. Further, it is generally accepted that Mars is magnetized more often than Venus, meaning the ionospheric thermal pressure is usually insufficient to exclude the external field from penetrating into the ionosphere (Zhang & Luhmann, 1992; Chu et al., 2021; Holmberg et al., 2019; Sánchez-Cano et al., 2020). Profiles resembling the magnetized ionosphere of Venus, such as the profile shown in Figure 4C, do exist but are quite rare.

Although the induced magnetic field profiles at Mars are unable to be categorized into simple states like at Venus, there are some reoccurring features that are worth reporting. First, the profiles often have a distinct prominent peak between 250-300 km. Examples of such profiles can be seen in Figure 4A, B, and D. Some profiles have many peaks, such as the one shown in Figure 4E. These multiple peaks at low altitudes may be due to a combination of both horizontal and vertical variations in the magnetic field strength (the spacecraft trajectory is not strictly vertical). Generally, magnetized profiles at Venus lack such a complicated structure.

Neither the complicated multi-peaked structures, nor a peak between 250-300 km were predicted by the earliest MHD models (Shinagawa & Cravens, 1989). More recent MHD studies that include the time-dependent effects of changing solar wind conditions do predict more complicated structures including a peak between 250-350 km (Y. J. Ma et al., 2014, 2017). The peaks are caused by vertical gradients in the downward plasma flow speed as a result of solar wind pressure variations on hour long timescales. Solar wind variations may be responsible for some of these small scale features (Cravens et al., 2023), but other processes such as plasma instabilities and global plasma dynamics likely play a role (Hamil et al., 2022).

3.2 Solar Zenith Angle Variations

To first order, we expect pressure balance to be maintained through the space environment. Given this assumption, the maximum induced magnetic field strength should depend on the solar wind dynamic pressure and the ionospheric thermal pressure. To achieve pressure balance, higher solar wind dynamic pressures should lead to stronger induced fields, while higher ionospheric thermal pressures should be able to exclude the solar wind field more efficiently, resulting in weaker induced fields. Mathematically, if pressure balance is satisfied throughout the low-altitude ionosphere then

$$P_{sw} \cos^2(\chi) = P_{th} + P_B \quad (2)$$

307 where $P_{sw}\cos^2\chi$ is the normal component of the solar wind dynamic pressure (Crider
 308 et al., 2003), χ is SZA, P_{th} is the ionospheric thermal pressure, and $P_B = B_{ind}^2/2\mu_o$
 309 is the induced magnetic field pressure. If we also assume $P_B \gg P_{th}$, which is often the
 310 case at Mars (Holmberg et al., 2019; Sánchez-Cano et al., 2020), then we expect the in-
 311 duced field strength to approximately follow

$$B_{ind} = (2\mu_o P_{sw})^{1/2} \cos(\chi) \quad (3)$$

312 where μ_o is the vacuum permeability. This equation predicts that, when magnetized ($P_B >$
 313 P_{th}), the induced magnetic field strength should be approximately proportional to co-
 314 sine of the SZA. We examine this prediction for both Venus and Mars.

315 Figure 5 shows B_{max} plotted against SZA for both planets. The Venus observa-
 316 tions are separated into their magnetized and unmagnetized classifications, but not sep-
 317 arated based on solar wind dynamic pressure because of data scarcity. The Mars obser-
 318 vations are sorted into groups based on solar wind dynamic pressure since the induced
 319 field will increase with increasing solar wind pressure (see Section 3.4). The data are binned
 320 along the SZA axis using uneven bin sizes so that each bin has a comparable number of
 321 data points.

322 At Venus the maximum field strengths of the unmagnetized profiles do not have
 323 a SZA dependence and are around 20 nT, which is consistent with previous studies (Elphic
 324 et al., 1984). The low field strengths are expected because, when unmagnetized, the ex-
 325 ternal magnetic field is excluded from the ionosphere by the high ionospheric thermal
 326 pressure, and thus the induced field strength is not expected to be driven by the solar
 327 wind pressure. In these cases $P_B \ll P_{th}$ so Eq. 3 is not applicable and we do not ex-
 328 pect any cosine dependence. In contrast, the maximum field strengths of the magnetized
 329 profiles decrease with increasing SZA up to a SZA of $\sim 65^\circ$. The bin-averaged maximum
 330 field strength decreases from ~ 80 nT near the subsolar point to ~ 40 nT near 65° SZA.
 331 This is consistent with previous work which has shown that this SZA trend is approx-
 332 imately satisfied in the magnetized Venus ionosphere, but the analysis was conducted
 333 with few observational data points (C. Russell et al., 1983).

334 Similarly, the maximum field strengths at Mars decrease from ~ 70 nT (35 nT) at
 335 the subsolar point to ~ 40 nT (25 nT) around 75° SZA during high (low) solar wind dy-
 336 namic pressure. There is also clear separation between the dynamic pressure bins, with
 337 higher maximum field strengths occurring during higher solar wind dynamic pressures,
 338 as predicted by Equation 3. The solar wind dynamic pressure trends at both planets will
 339 be further explored in Section 3.4.

340 The dotted lines shown in Figure 5 are fits to the data using SZA for χ in Equa-
 341 tion 3. Specifically, we fit the binned averages to $B_{max} = B_0 \cos(\chi)$ where B_0 is a fit
 342 parameter that represents the subsolar induced field strength. In both cases, the data
 343 are poorly fit. We suggest this deviation from the prediction is a consequence of SZA
 344 being only an approximation of the angle between the solar wind bulk flow velocity and
 345 the obstacle. We refit the data after replacing χ with θ , where θ is the angle between
 346 the solar wind flow and the MPB (Crider et al., 2003). For Venus we use the MPB shape
 347 found by Xu et al. (2021) and for Mars we use the MPB shape given in Vignes et al. (2000).
 348 The fits are markedly improved when using θ in place of SZA. It is especially apparent
 349 at Mars that the trend follows the shape of the MPB rather than of cosine of SZA. The
 350 fit parameter (B_0) for Venus is 79.5 ± 0.9 . The fit parameters for Mars are 79.2 ± 0.4 , 51.7 ± 2.0 ,
 351 and 40.1 ± 1.4 for the high, medium, and low solar cases, respectively.

352 From these two plots we conclude low-altitude maximum field strength follows the
 353 predicted cosine trend (Eq. 3) up to at least 60° when in a magnetized state, but only
 354 if the angle between the solar wind flow and the MPB is used (θ). However, near the ter-

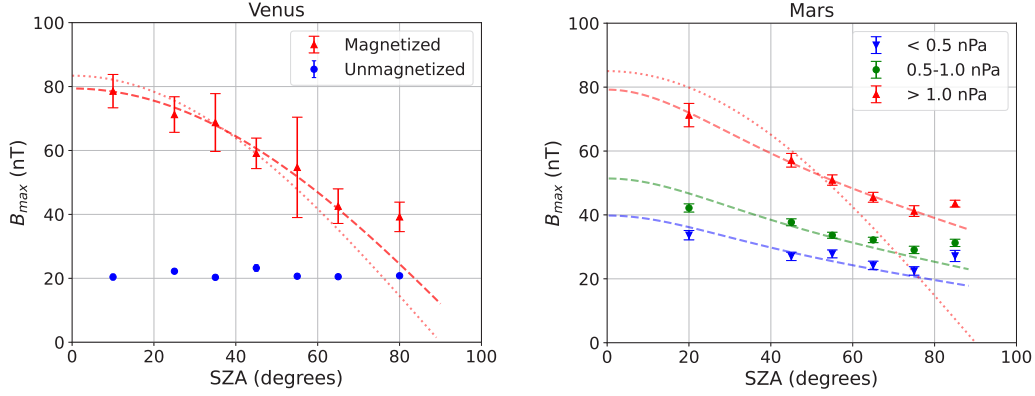


Figure 5: The solar zenith angle (SZA) variation of B_{max} for Venus (left) and Mars (right). The dotted lines are fits to $B_{max} = B_0 \cos(\chi)$ (see Equation 3) using SZA for χ . The dashed lines are fits using θ (the angle between the solar wind flow and the magnetic pileup boundary) in place of χ (Vignes et al., 2000; Xu et al., 2021). The Venus data are sorted into magnetized and unmagnetized cases while the Mars data are sorted into solar wind dynamic pressure bins. Error bars show the standard error in each bin. The solar zenith angle bins for Venus have edges at 0° , 20° , 30° , 40° , 50° , 60° , 70° , and 90° . The SZA bins for Mars have edges at 0° , 40° , 50° , 60° , 70° , 80° , and 90° .

355 minator B_{max} is higher than predicted at both planets. We currently do not have an ex-
 356 planation for this observed deviation.

3.3 Peak Magnetic Field Distributions

357
 358 In Figure 6A, we plot histograms of B_{max} with the Venus data separated into mag-
 359 netized and unmagnetized categories (Section 3.1). All the B_{max} values from Mars and
 360 all the magnetized B_{max} values from Venus are corrected to the subsolar point by di-
 361 viding them by $\cos(\theta)$. Only B_{max} values at $\text{SZA} < 60^\circ$ are included (Section 3.2). The
 362 histogram of the unmagnetized B_{max} values at Venus form a sharp peak around 20 nT,
 363 which is the typical magnitude of the induced field when unmagnetized. The histogram
 364 of the magnetized B_{max} values at Venus form a much wider distribution, but demon-
 365 strates the clear demarcation between magnetized and unmagnetized states. The mag-
 366 netized distribution has a mean of $77.8 (\pm 29.2)$ nT and a median of 75.7 nT. Compar-
 367 atively, the distribution of the Mars B_{max} values has a mean of $62.9 (\pm 29.4)$ nT and a
 368 median of 55.7 nT.

369 At the subsolar point, Equation 3 predicts $B_{max} = (2\mu_0 P_{sw})^{1/2}$ (Fang et al., 2023).
 370 Since P_{sw} scales as the inverse square of the planet-Sun distance, we expect larger B_{max}
 371 values at Venus than Mars, which is confirmed in Figure 6. Given the inverse square law,
 372 Equation 3 predicts $\frac{B_{max,Venus}}{B_{max,Mars}} \simeq \frac{1.5\text{AU}}{0.7\text{AU}} \simeq 2.1$. However, the observed ratio is only 1.2
 373 if using the means of the distributions (77.8 nT/ 62.9 nT), or 1.4 if using the medians (75.7
 374 nT/ 55.7 nT). If we account for the crustal field component at Mars, that is at most 20%
 375 of B_{max} (in most cases is less than 10% of B_{max}), then the observed ratio is at most 1.75
 376 ($1.4/0.8$), still implying the observed ratio is smaller than the prediction of 2.2.

377 To explore why the ratio is smaller than predicted, Figure 6B shows a comparison
 378 of the observed and predicted B_{max} . In particular, the histograms show the ratio between
 379 the observed B_{max} and the predicted B_{max} for each profile. Only observations with SZA
 380 $< 60^\circ$ are included. The Venus ratios are usually less than one, having a mean of 0.66

(± 0.22) nT. A possible explanation is that Equation 3 relies on two assumptions: (1) pressure balance throughout the space environment and (2) the ionospheric thermal pressure is negligible compared to the magnetic pressure. At Venus, the second assumption is often not satisfied (Luhmann et al., 1987) leading to a reduction in the induced field strength via Equation 2.

At Mars, the ratios are usually greater than one, with a mean of 1.38 (± 0.22) nT. If we consider a 20% crustal field component, the mean would decrease to at least 1.1, still implying the induced field strengths at Mars are somewhat larger than predicted by Equation 3. Since the second assumption is usually satisfied at Mars (Holmberg et al., 2019; Chu et al., 2021; Sánchez-Cano et al., 2020), it might be expected that Equation 3 is a good predictor of the maximum induced field strength. A possible explanation for why B_{max} is usually larger than the prediction is the presence of small-scale features in the magnetic field profile. These small scale features are much more prevalent at Mars than at Venus. They result in small-scale spikes and bumps that can lead to a higher B_{max} than predicted. These small scale structures arise from a variety of processes, such as waves, rotations, plasma instabilities (Hamil et al., 2022; Cravens et al., 2023).

Lastly, Figure 6c shows histograms of the altitude where B_{max} is observed. At Venus, the altitude of the low-altitude maximum induced field, when magnetized, is consistently around 170 km. There are rarer cases where the altitude of B_{max} is much higher, including a number of profiles with the altitude bin in the highest histogram bin near 250 km. These are the edge cases discussed in Section 3.3 and are profiles similar to Figure 3E. The peak altitude at Mars is typically between 160-200 km, but the distribution is much wider than the distribution at Venus. The distribution is likely wider because of seasonal variations in the upper atmosphere of Mars, which causes constant pressure levels to rise and fall over the year owing to the changing insolation from Mars' elliptical orbit.

3.4 Solar Wind Dynamic Pressure

It is expected that with increasing solar wind pressure, the induced field strength will increase. Assuming pressure balance across the magnetic pileup boundary and into the ionosphere, and negligible ionospheric thermal pressure, the induced field strength should vary as the square root of the solar wind dynamic pressure (Eq. 3). Previous work has shown that the magnetic field at the MPB does respond in this manner to solar wind dynamic pressure variations (Crider et al., 2003; Xu et al., 2021). Below the MPB, we still expect the induced field to increase with increasing dynamic pressure because the fields at the MPB are convected downward into the ionosphere.

Figure 7 shows the dependence B_{max} on solar wind dynamic pressure. The magnetized Venus data, and the Mars data, are corrected to the subsolar point by dividing them by $\cos(\theta)$ (see Section 3.2). The plot only contains data with $\text{SZA} < 60^\circ$. We fit a power law to the observations: $B_{max} = B_0 P_{sw}^n$ where B_0 is the best-fit subsolar B_{max} and n is the best-fit exponent. B_{max} increases with solar wind pressure for both Venus (when magnetized) and Mars with power law exponents $n = 0.57 \pm 0.13$ and $n = 0.45 \pm 0.02$ respectively. These are consistent with each other within error, however the Venus fit has significant uncertainty due to having much fewer data points and a more narrow range of solar wind pressure coverage compared to Mars. The R-squared value of the fits is 0.2 for Venus (magnetized) and 0.6 for Mars.

The coefficient B_0 of the power law fit for Venus (magnetized) is 27.7 ± 6.1 whereas the coefficient for Mars is 65.2 ± 0.7 . This implies that for a solar wind pressure of 1 nPa, Mars would have a higher induced field, which is expected since Venus tends to exclude the external magnetic field more effectively than Mars (consistent with figure 6c). However, Venus is more likely to experience higher solar wind dynamic pressure since it is closer to the Sun. As a result, the average B_{max} for Venus (when magnetized) is higher than at Mars (see Section 3.3).

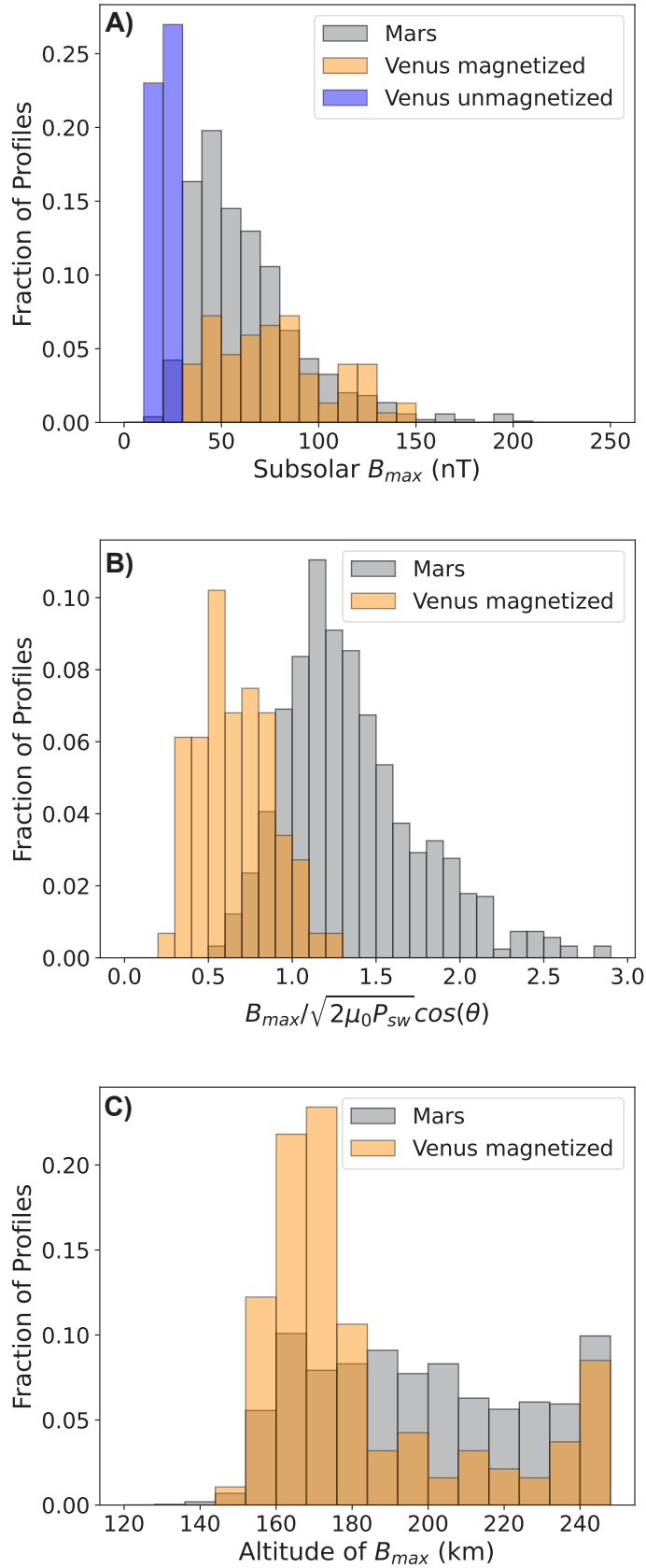


Figure 6: (A) Histograms of B_{max} , the maximum low-altitude field strength. (B) Ratios of the observed B_{max} and the B_{max} predicted by Equation 3. (C) Histograms of the altitude of B_{max} .

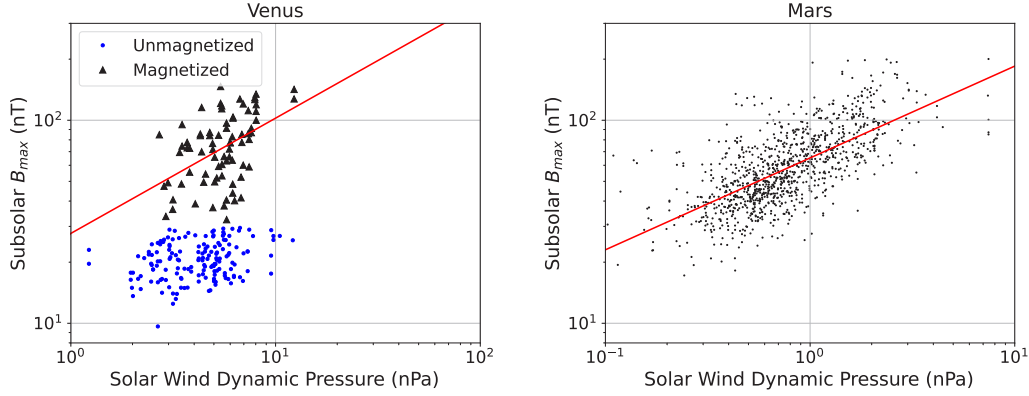


Figure 7: The variation of B_{max} with solar wind dynamic pressure for Venus (left) and Mars (right). For Venus, values derived from magnetized profiles are plotted as black triangles and values derived from unmagnetized profiles are plotted as blue circles. The red lines are power law fits with derived exponents of 0.57 ± 0.13 for Venus (magnetized) and 0.45 ± 0.02 for Mars.

432 The induced field strength of the unmagnetized ionosphere of Venus has virtually
 433 no dependence on solar wind dynamic pressure. The best-fit exponent is zero and the
 434 R-squared value is 0.01. This lack of dependence on solar wind pressure is expected be-
 435 cause, when unmagnetized, the solar wind magnetic field is excluded from low altitudes
 436 by the ionospheric thermal pressure.

437 4 Discussion and Conclusions

438 In this study, we compare low-altitude induced magnetic fields at Venus and Mars.
 439 Our main results are as follows:

- 440 1. The magnetic field profiles at Venus and Mars have different altitude structures.
 441 The magnetized profiles at Venus have distinct, identifiable features, namely a peak
 442 in magnetic field around 170 km, a wide minimum around 200 km, and a nearly
 443 constant topside above 250 km. But the Mars profiles lack these distinct, repeat-
 444 able large-scale features that would allow them to be classified into magnetized
 445 and unmagnetized categories like Venus.
- 446 2. The maximum low-altitude magnetic field strength (B_{max}) in the unmagnetized
 447 ionosphere of Venus has no dependence on SZA. The B_{max} in the magnetized iono-
 448 sphere of Venus, and the B_{max} at Mars, have a SZA dependence where $B_{max} \propto$
 449 $\cos(\theta)$ where θ is the angle between the solar wind velocity and the MPB normal
 450 vector (Eq. 3). However, at both planets, B_{max} is larger near the terminator than
 451 this trend predicts.
- 452 3. The mean Venus B_{max} (77.8 nT) is greater than the mean Mars B_{max} (62.9 nT)
 453 which is expected since Venus is exposed to higher solar wind pressures. When
 454 comparing B_{max} with the prediction from Eq. 3 — which is derived assuming pres-
 455 sure balance is maintained and $P_{th} \ll P_B$ — the B_{max} at Venus (magnetized)
 456 is lower than predicted by a factor of 0.66. The B_{max} at Mars, alternatively, is
 457 higher than predicted by a factor between 1.1 and 1.38.
- 458 4. When unmagnetized, Venus B_{max} has no dependence on solar wind dynamic pres-
 459 sure (P_{sw}). When magnetized, Venus B_{max} has a dependence of $B_{max} \propto (P_{sw})^{0.57 \pm 0.13}$,
 460 which is potentially consistent with the prediction from Equation 3 of an expo-

461 nent of 0.5. However, the fit is poor and the dynamic pressure can only account
 462 for 20% of the variation in B_{max} . The Mars B_{max} , in contrast, has a dependence
 463 of $B_{max} \propto (P_{sw})^{0.45 \pm 0.02}$, and the dynamic pressure can account for 60% of the
 464 variation in B_{max} .

465 The vertical structure of the magnetic field profiles at Mars is highly varied and
 466 inconsistent, in contrast with the Venus profiles which tend to have the same recurring
 467 large-scale features. A likely explanation is the ubiquitous presence of small-scale struc-
 468 tures in the magnetic field profiles at Mars, which are much less common in the mag-
 469 netized ionosphere of Venus. This explanation was also put forth by Huang et al. (2023)
 470 to explain the varied magnetic field profiles at Mars. They attributed the varied struc-
 471 tures to time-dependent variations in the up stream solar wind, such as variations in the
 472 solar wind dynamic pressure. The vertical structure of the Venus magnetic field profiles
 473 can be successfully reproduced by models, even under steady solar wind conditions (Luhmann
 474 et al., 1984; Cravens et al., 1984; Shinagawa & Cravens, 1988; Luhmann & Cravens, 1991).
 475 However, models have been less successful at reproducing the vertical structure of the
 476 Mars profiles. Additional physical processes likely need to be included to capture the small-
 477 scale structures (Hamil et al., 2022; Cravens et al., 2023).

478 We find both similarities and differences between the low-altitude magnetic field
 479 strengths. The main similarity arises between Mars and the magnetized ionosphere of
 480 Venus, providing further evidence that the ionosphere of Mars is magnetized most of the
 481 time (Sánchez-Cano et al., 2020). In particular, the low-altitude field strengths have the
 482 same SZA dependence, including higher than expected fields near the terminator. Fur-
 483 ther, at both planets the SZA variation of the low-altitude field strengths are modeled
 484 best when the angle between solar wind velocity and the normal vector of the MPB is
 485 used in Equation 3 (as opposed to SZA). In other words, since the low-altitude magnetic
 486 fields are convected downward from the MPB (Equation 1), the shape of the MPB con-
 487 trols how the strength of the low-altitude induced fields vary across the dayside iono-
 488 sphere.

489 Major differences include higher induced field strengths in the magnetized ionosphere
 490 of Venus (means of 77.8 nT vs. 62.9 nT), which is expected given Venus is exposed to
 491 higher solar wind dynamic pressures due to its proximity to the Sun. Additionally, when
 492 magnetized, the low-altitude field at Venus is weaker than predicted under the assump-
 493 tions of pressure balance and $P_{th} \ll P_B$ (Eq. 3). This is consistent with the fact that
 494 the assumption of $P_{th} \ll P_B$ is often unsatisfied at Venus because the ionospheric ther-
 495 mal pressure is often comparable to or greater than the solar wind dynamic pressure, es-
 496 pecially during the PVO observations at solar maximum (Luhmann, 1986; Zhang & Luh-
 497 mann, 1992). Consequently, the induced magnetic pressure does not have to be as large
 498 as the solar wind pressure to achieve pressure balance (Eq. 2).

499 In contrast, on Mars, low-altitude field strengths are higher than predicted by Equa-
 500 tion 3, even after accounting for possible contributions from crustal fields. One possi-
 501 ble explanation is again related to small scale features that are common at Mars but not
 502 at Venus. These observed small scale features may be either spatial (Hamil et al., 2022)
 503 or temporal (Huang et al., 2020) variations, and are likely driven by processes such as
 504 varying solar wind conditions, large-scale plasma dynamics, plasma instabilities, or cur-
 505 rent sheets (Hamil et al., 2022). The small scale features, such as the localized layers seen
 506 in Figure 4E, can increase the maximum low-altitude field strength so that is larger than
 507 predicted by Equation 3.

508 The increased presence of small-scale structures at Mars may be related to the con-
 509 vection and diffusion timescales, which characterize the time for the low-altitude induced
 510 fields to form and dissipate (Eq. 1). Recent calculations suggest the convection and dif-
 511 fusion timescales are on the order of a few hours at Venus (Y. Ma et al., 2020), but only
 512 on the order of tens of minutes at Mars (Huang et al., 2020). Given the timescales at

Mars can be shorter than the time it takes for MAVEN complete a low-altitude peria-
 sis pass (~ 10 minutes), it is possible some of the observed small-scale features are caused
 by temporal variations in the upstream solar wind, as suggested by Huang et al. (2020).
 However, these calculations are somewhat uncertain because they are strongly controlled
 by vertical plasma velocities, which are small (tens of m/s) and have not been directly
 measured (Y. Ma et al., 2020).

Taken together, our results reveal some interesting similarities and differences be-
 tween the induced magnetic fields at Venus and Mars. They point to how planetary prop-
 erties, such as planet-Sun distance, can affect the structure and variability of induced
 fields at unmagnetized planets. Being closer to the Sun, Venus has a higher ionospheric
 thermal pressure that is often comparable to or greater than the solar wind dynamic pres-
 sure (at least at solar maximum during the PVO observations). Consequently, it exhibits
 a dichotomy of magnetized and unmagnetized states, and in each state the induced field
 strength has a different dependence on SZA and solar wind dynamic pressure. Mars, be-
 ing further from the Sun, has a lower ionospheric thermal pressure (from reduced solar
 EUV flux) and so the ionosphere is magnetized most of the time and does not exhibit
 a dichotomy of states. Further, the shape of the MPB controls the SZA variation of the
 induced fields at both planets, when in a magnetized state. This work focuses exclusively
 on weak crustal field regions at Mars, and future work focusing on strong crustal fields
 regions may reveal even more interesting differences between the low-altitude induced
 magnetic fields at Venus and Mars.

5 Open Research

The data used in this work are publicly archived. The Venus magnetometer data
 can be found at <https://pds-ppi.igpp.ucla.edu/search/view/?f=yes&id=pds://PPI/PVO-V-OMAG-4--SCCOORDS-24SEC-V2.0> and the Venus upstream solar wind data
 can be found at <https://cdaweb.gsfc.nasa.gov/cgi-bin/eval1.cgi>. The Mars Key
 Parameters data can be found at <https://lasp.colorado.edu/maven/sdc/public/data/sci/kp/> and the Mars upstream solar wind data can be found at <https://homepage.physics.uiowa.edu/~jhalekas/drivers.html>. The derived maximum low-altitude
 magnetic field strengths are publicly archived at <https://zenodo.org/uploads/10278080>
 for both Venus and Mars.

Acknowledgments

This work was supported by NASA grant 80NSSC21K0147 which was funded through
 the Solar System Workings program. S. Byrd received additional support from the NASA
 Iowa Space Grant Consortium and the John and Elsie Mae Ferentz Undergraduate Re-
 search Fund.

References

- Bertucci, C., Duru, F., Edberg, N., Fraenz, M., Martinecz, C., Szego, K., & Vais-
 berg, O. (2011). The induced magnetospheres of Mars, Venus, and Titan. *Space Sci. Rev.*, *162*, 113–171.
- Bowers, C. F., Slavin, J. A., DiBraccio, G. A., Poh, G., Hara, T., Xu, S., &
 Brain, D. A. (2021). MAVEN Survey of Magnetic Flux Rope Proper-
 ties in the Martian Ionosphere: Comparison With Three Types of For-
 mation Mechanisms. *Geophys. Res. Lett.*, *48*(10), e2021GL093296. doi:
<https://doi.org/10.1029/2021GL093296>
- Brace, L. H., & Kliore, A. J. (1991). The structure of the Venus ionosphere. *Space
 Sci. Rev.*, *55*, 81–163. doi: 10.1007/BF00177136
- Brain, D. A. (2003). Martian magnetic morphology: Contributions from the solar

- 561 wind and crust. *Journal of Geophysical Research*, 108(A12), 1424. doi: 10.
562 .1029/2002JA009482
- 563 Chu, F., Girazian, Z., Duru, F., Ramstad, R., Halekas, J., Gurnett, D. A., . . . Kopf,
564 A. J. (2021). The dayside ionopause of Mars: Solar wind interaction, pressure
565 balance, and comparisons with Venus. *Journal of Geophysical Research: Plan-*
566 *ets*, 126(11), e2021JE006936. doi: <https://doi.org/10.1029/2021JE006936>
- 567 Cloutier, P. A. (1984). Formation and dynamics of large-scale magnetic structures
568 in the ionosphere of Venus. *Journal of Geophysical Research: Space Physics*,
569 89(A4), 2401-2405.
- 570 Connerney, J. E. P., Acuña, M. H., Wasilewski, P. J., Kletetschka, G., Ness, N. F.,
571 Rème, H., . . . Mitchell, D. L. (2001). The global magnetic field of Mars
572 and implications for crustal evolution. *Geophysical Research Letters*, 28(21),
573 4015–4018. doi: 10.1029/2001GL013619
- 574 Cravens, T. E., Hamil, O., Renzaglia, A., Ledvina, S. A., & Howard, S. K. (2023).
575 Fourier analysis of magnetic fields in the ionosphere of Mars. *Journal of Geo-*
576 *physical Research: Space Physics*, 128(4), e2022JA031044.
- 577 Cravens, T. E., Shinagawa, H., & Nagy, A. F. (1984). The evolution of large-scale
578 magnetic fields in the ionosphere of Venus. *Geophysical Research Letters*,
579 11(3), 267–270. doi: 10.1029/GL011i003p00267
- 580 Crider, D. H., Vignes, D., Krymskii, A. M., Breus, T. K., Ness, N. F., Mitchell,
581 D. L., . . . Acuña, M. H. (2003). A proxy for determining solar wind dynamic
582 pressure at Mars using Mars Global Surveyor data. *J. Geophys. Res.*, 108,
583 1461, 10.1029/2003JA009875. doi: 10.1029/2003JA009875
- 584 Daniell Jr, R., & Cloutier, P. (1977). Distribution of ionospheric currents induced
585 by the solar wind interaction with Venus. *Planetary and Space Science*, 25(7),
586 621–628.
- 587 Elphic, R. C., Brace, L. H., Theis, R. F., & Russell, C. T. (1984). Venus dayside
588 ionospheric conditions - Effects of ionospheric magnetic field and solar EUV
589 flux. *Geophys. Res. Lett.*, 11, 124–127. doi: 10.1029/GL011i002p00124
- 590 Elphic, R. C., & Russell, C. T. (1983). Magnetic flux ropes in the Venus ionosphere:
591 Observations and models. *Journal of Geophysical Research: Space Physics*,
592 88(A1), 58-72. doi: 10.1029/JA088iA01p00058
- 593 Elphic, R. C., Russell, C. T., Slavin, J. A., & Brace, L. H. (1980). Observations
594 of the dayside ionopause and ionosphere of Venus. *Journal of Geophysical Re-*
595 *search*, 85(A13), 7679. doi: 10.1029/JA085iA13p07679
- 596 Espley, J. R. (2018). The martian magnetosphere: Areas of unsettled terminol-
597 ogy. *Journal of Geophysical Research: Space Physics*, 123(6), 4521-4525. doi:
598 10.1029/2018JA025278
- 599 Fang, X., Ma, Y., Luhmann, J., Dong, Y., Brain, D., Hurley, D., . . . Jakosky, B.
600 (2018). The Morphology of the Solar Wind Magnetic Field Draping on the
601 Dayside of Mars and Its Variability. *Geophysical Research Letters*, 45(8),
602 3356–3365. doi: <https://doi.org/10.1002/2018GL077230>
- 603 Fang, X., Ma, Y., Luhmann, J., Dong, Y., Halekas, J., & Curry, S. (2023). Mars
604 global distribution of the external magnetic field and its variability: Maven
605 observation and MHD prediction. *Journal of Geophysical Research: Space*
606 *Physics*, 128(9), e2023JA031588. doi: 10.1029/2023JA031588
- 607 Halekas, J. S., Ruhunusiri, S., Harada, Y., Collinson, G., Mitchell, D. L., Mazelle,
608 C., . . . Jakosky, B. M. (2017, January). Structure, dynamics, and seasonal
609 variability of the Mars-solar wind interaction: MAVEN Solar Wind Ion An-
610 alyzer in-flight performance and science results. *Journal of Geophysical Re-*
611 *search: Space Physics*, 122(1), 547–578. doi: 10.1002/2016JA023167
- 612 Hamil, O., Cravens, T. E., Renzaglia, A., & Andersson, L. (2022). Small scale
613 magnetic structure in the induced martian ionosphere and lower magnetic
614 pile-up region. *Journal of Geophysical Research: Space Physics*, 127(4),
615 e2021JA030139. doi: <https://doi.org/10.1029/2021JA030139>

- 616 Holmberg, M. K. G., André, N., Garnier, P., Modolo, R., Andersson, L., Halekas,
617 J., ... Mitchell, D. L. (2019). MAVEN and MEX Multi-instrument Study
618 of the Dayside of the Martian Induced Magnetospheric Structure Revealed by
619 Pressure Analyses. *Journal of Geophysical Research: Space Physics*, *124*(11),
620 8564–8589. doi: 10.1029/2019JA026954
- 621 Huang, J.-P., Cui, J., Hao, Y.-Q., Guo, J.-P., Wu, X.-S., Niu, D.-D., & Wei, Y.
622 (2020). Solar and Magnetic Control of Minor Ion Peaks in the Dayside Mar-
623 tian Ionosphere. *Journal of Geophysical Research: Space Physics*, *125*(8),
624 e2020JA028254. doi: <https://doi.org/10.1029/2020JA028254>
- 625 Huang, J.-P., Hao, Y.-Q., Lu, H.-Y., & Cui, J. (2023). Variability of draped inter-
626 planetary magnetic field in the subsolar martian ionosphere. *The Astrophysical*
627 *Journal*, *955*(1), 48.
- 628 Intriligator, D. S., Wolfe, J. H., & Mihalov, J. D. (1980, January). The Pi-
629 oneer Venus Orbiter Plasma Analyzer Experiment. *IEEE Transactions*
630 *on Geoscience and Remote Sensing*, *GE-18*(1), 39–43. doi: 10.1109/
631 TGRS.1980.350258
- 632 Jakosky, B. M., Lin, R. P., Grebowsky, J. M., Luhmann, J. G., Mitchell, D. F., Beu-
633 telschies, G., ... Zurek, R. (2015, December). The Mars Atmosphere and
634 Volatile Evolution (MAVEN) Mission. *Space Science Reviews*, *195*(1-4), 3–48.
635 doi: 10.1007/s11214-015-0139-x
- 636 Kar, J., & Mahajan, K. K. (1987). On the response of ionospheric magnetisation
637 to solar wind dynamic pressure from pioneer venus measurements. *Geophysical*
638 *Research Letters*, *14*(5), 507–510. doi: 10.1029/GL014i005p00507
- 639 Lee, C. O., Hara, T., Halekas, J. S., Thiemann, E., Chamberlin, P., Eparvier, F.,
640 ... Jakosky, B. M. (2017, March). MAVEN observations of the solar cycle
641 24 space weather conditions at Mars. *Journal of Geophysical Research: Space*
642 *Physics*, *122*(3), 2768–2794. doi: 10.1002/2016JA023495
- 643 Luhmann, J. G. (1986, September). The solar wind interaction with Venus. *Space*
644 *Science Reviews*, *44*(3), 241–306. doi: 10.1007/BF00200818
- 645 Luhmann, J. G., & Cravens, T. E. (1991). Magnetic fields in the ionosphere of
646 Venus. *βr*, *55*, 201–274. doi: 10.1007/BF00177138
- 647 Luhmann, J. G., Elphic, R. C., Russell, C. T., Mihalov, J. D., & Wolfe, J. H. (1980,
648 November). Observations of large scale steady magnetic fields in the dayside
649 Venus ionosphere. *Geophysical Research Letters*, *7*(11), 917–920. doi: 10.1029/
650 GL007i011p00917
- 651 Luhmann, J. G., Ledvina, S. A., & Russell, C. T. (2004). Induced magneto-
652 spheres. *Advances in Space Research*, *33*(11), 1905–1912. doi: 10.1016/
653 j.asr.2003.03.031
- 654 Luhmann, J. G., & Russell, C. T. (1983). Magnetic fields in the ionospheric holes
655 of venus: Evidence for an intrinsic field? *Geophysical Research Letters*, *10*(5),
656 409–411. Retrieved from [https://agupubs.onlinelibrary.wiley.com/
657 doi/abs/10.1029/GL010i005p00409](https://agupubs.onlinelibrary.wiley.com/doi/abs/10.1029/GL010i005p00409) doi: [https://doi.org/10.1029/
658 GL010i005p00409](https://doi.org/10.1029/
658 GL010i005p00409)
- 659 Luhmann, J. G., Russell, C. T., & Elphic, R. C. (1984). Time scales for the de-
660 cay of induced large-scale magnetic fields in the venus ionosphere. *Journal of*
661 *Geophysical Research: Space Physics*, *89*(A1), 362–368. doi: [https://doi.org/10
662 .1029/JA089iA01p00362](https://doi.org/10
662 .1029/JA089iA01p00362)
- 663 Luhmann, J. G., Russell, C. T., Scarf, F. L., Brace, L. H., & Knudsen, W. C.
664 (1987). Characteristics of the Marslike limit of the Venus-solar wind in-
665 teraction. *Journal of Geophysical Research*, *92*(A8), 8545. doi: 10.1029/
666 JA092iA08p08545
- 667 Ma, Y., Combi, M. R., Tenishev, V., Shou, Y., & Bougher, S. (2023). The effects
668 of the upper atmosphere and corona on the solar wind interaction with venus.
669 *Journal of Geophysical Research: Space Physics*, *128*(4), e2022JA031239.
670 (e2022JA031239 2022JA031239) doi: <https://doi.org/10.1029/2022JA031239>

- 671 Ma, Y., Toth, G., Nagy, A., Luhmann, J., & Russell, C. (2020). Formation and Evo-
672 lution of the Large-Scale Magnetic Fields in Venus' Ionosphere: Results From
673 a Three Dimensional Global Multispecies MHD Model. *Geophysical Research*
674 *Letters*, *47*(11), e2020GL087593. doi: 10.1029/2020GL087593
- 675 Ma, Y. J., Fang, X., Nagy, A. F., Russell, C. T., & Toth, G. (2014). Martian iono-
676 spheric responses to dynamic pressure enhancements in the solar wind. *J. Geo-*
677 *phys. Res.*, *119*(2), 1272–1286. doi: 10.1002/2013JA019402
- 678 Ma, Y. J., Russell, C. T., Fang, X., Dong, C. F., Nagy, A. F., Toth, G., ... Jakosky,
679 B. M. (2017). Variations of the Martian plasma environment during the ICME
680 passage on 8 March 2015: A time-dependent MHD study. *J. Geophys. Res.*,
681 *122*(2), 1714–1730. doi: 10.1002/2016JA023402
- 682 Morschhauser, A., Lesur, V., & Grott, M. (2014, June). A spherical harmonic
683 model of the lithospheric magnetic field of Mars. *Journal of Geophysical Re-*
684 *search: Planets*, *119*(6), 1162–1188. Retrieved 2019-12-04, from [http://](http://doi.wiley.com/10.1002/2013JE004555)
685 doi.wiley.com/10.1002/2013JE004555 doi: 10.1002/2013JE004555
- 686 Phillips, J. L., Luhmann, J. G., & Russell, C. T. (1984a). Growth and maintenance
687 of large-scale magnetic fields in the dayside Venus ionosphere. *Journal of*
688 *Geophysical Research: Space Physics*, *89*(A12), 10676–10684. Retrieved from
689 [https://agupubs-onlinelibrary-wiley-com.proxy.lib.uiowa.edu/doi/](https://agupubs-onlinelibrary-wiley-com.proxy.lib.uiowa.edu/doi/abs/10.1029/JA089iA12p10676)
690 [abs/10.1029/JA089iA12p10676](https://agupubs-onlinelibrary-wiley-com.proxy.lib.uiowa.edu/doi/abs/10.1029/JA089iA12p10676) doi: 10.1029/JA089iA12p10676
- 691 Phillips, J. L., Luhmann, J. G., & Russell, C. T. (1984b). Growth and mainte-
692 nance of large-scale magnetic fields in the dayside venus ionosphere. *Journal*
693 *of Geophysical Research: Space Physics*, *89*(A12), 10676–10684. doi: 10.1029/
694 [JA089iA12p10676](https://doi.org/10.1029/JA089iA12p10676)
- 695 Ramstad, R. (2020). The global current systems of the Martian induced magneto-
696 sphere. *Nature Astronomy*, *4*, 7.
- 697 Ruhunusiri, S., Halekas, J. S., Espley, J. R., Eparvier, F., Brain, D., Mazelle, C., ...
698 Jakosky, B. M. (2018). An Artificial Neural Network for Inferring Solar Wind
699 Proxies at Mars. *Geophysical Research Letters*, *45*(20), 10,855–10,865. doi:
700 [10.1029/2018GL079282](https://doi.org/10.1029/2018GL079282)
- 701 Russell, C., Luhmann, J., & Elphic, R. (1983). The properties of the low altitude
702 magnetic belt in the venus ionosphere. *Advances in Space Research*, *2*(10), 13–
703 16.
- 704 Russell, C. T., Snare, R. C., Means, J. D., & Elphic, R. C. (1980). Pioneer venus
705 orbiter fluxgate magnetometer. *IEEE Transactions on Geoscience and Remote*
706 *Sensing, GE-18*(1), 32–35. doi: 10.1109/TGRS.1980.350256
- 707 Shinagawa, H., & Cravens, T. E. (1988). A one-dimensional multispecies magneto-
708 hydrodynamic model of the dayside ionosphere of Venus. *Journal of Geophys-*
709 *ical Research*, *93*(A10), 11263. doi: 10.1029/JA093iA10p11263
- 710 Shinagawa, H., & Cravens, T. E. (1989, June). A one-dimensional multispecies
711 magnetohydrodynamic model of the dayside ionosphere of Mars. *Journal*
712 *of Geophysical Research: Space Physics*, *94*(A6), 6506–6516. Retrieved
713 2019-12-04, from <http://doi.wiley.com/10.1029/JA094iA06p06506> doi:
714 [10.1029/JA094iA06p06506](https://doi.org/10.1029/JA094iA06p06506)
- 715 Sánchez-Cano, B., Narvaez, C., Lester, M., Mendillo, M., Mayyasi, M., Holmstrom,
716 M., ... Durward, S. (2020). Mars' ionopause: A matter of pressures. *Jour-*
717 *nal of Geophysical Research: Space Physics*, *125*(9), e2020JA028145. doi:
718 <https://doi.org/10.1029/2020JA028145>
- 719 Vignes, D., Mazelle, C., Rme, H., Acuña, M. H., Connerney, J. E. P., Lin, R. P.,
720 ... Ness, N. F. (2000). The solar wind interaction with mars: Locations and
721 shapes of the bow shock and the magnetic pile-up boundary from the obser-
722 vations of the mag/er experiment onboard mars global surveyor. *Geophysical*
723 *Research Letters*, *27*(1), 49–52. doi: <https://doi.org/10.1029/1999GL010703>
- 724 Xu, Q., Xu, X., Zhang, T. L., Rong, Z. J., Wang, M., Wang, J., ... Luo, L. (2021).
725 The Venus Express observation of Venus' induced magnetosphere boundary

726 at solar maximum. *Astron. Astrophys.*, 652, A113. doi: 10.1051/0004-6361/
727 202141391
728 Zhang, M. H. G., & Luhmann, J. G. (1992). Comparisons of peak ionosphere pres-
729 sures at Mars and Venus with incident solar wind dynamic pressure. *J. Geo-*
730 *phys. Res.*, 97, 1017–1025. doi: 10.1029/91JE02721

Figure 1.

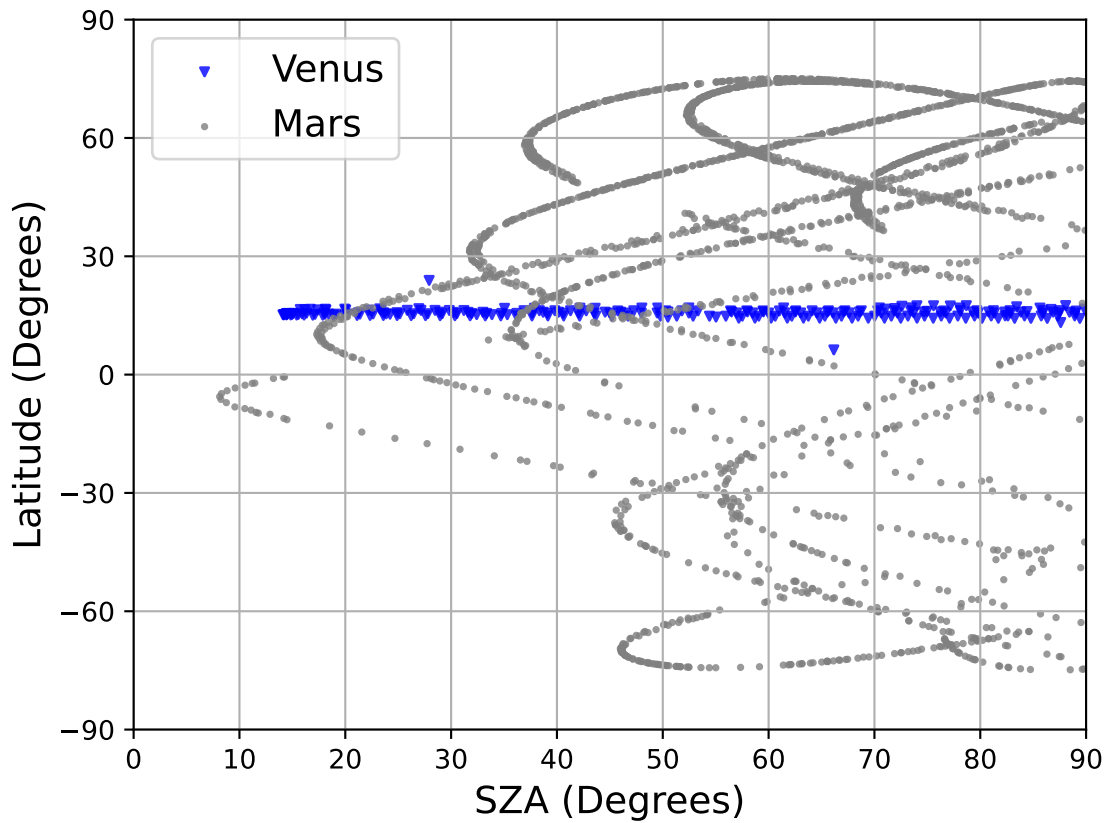


Figure 2.

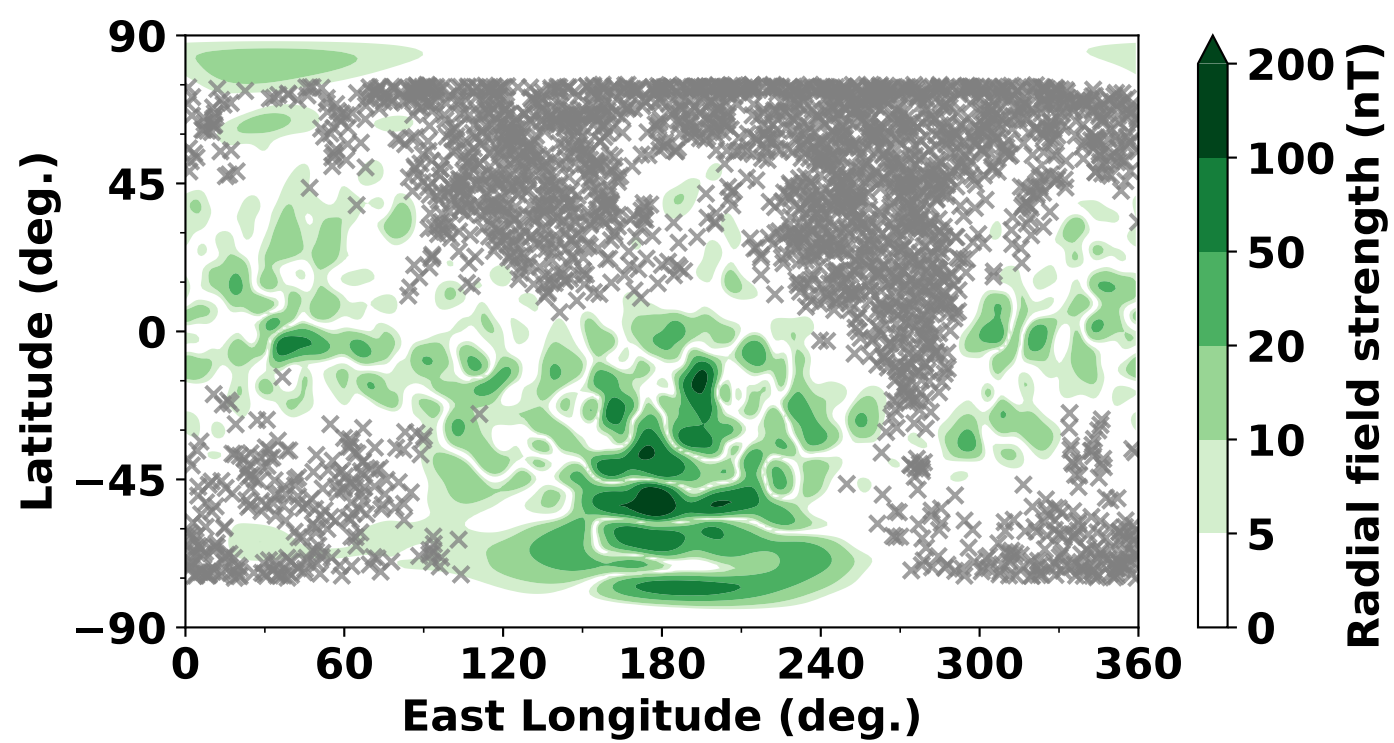
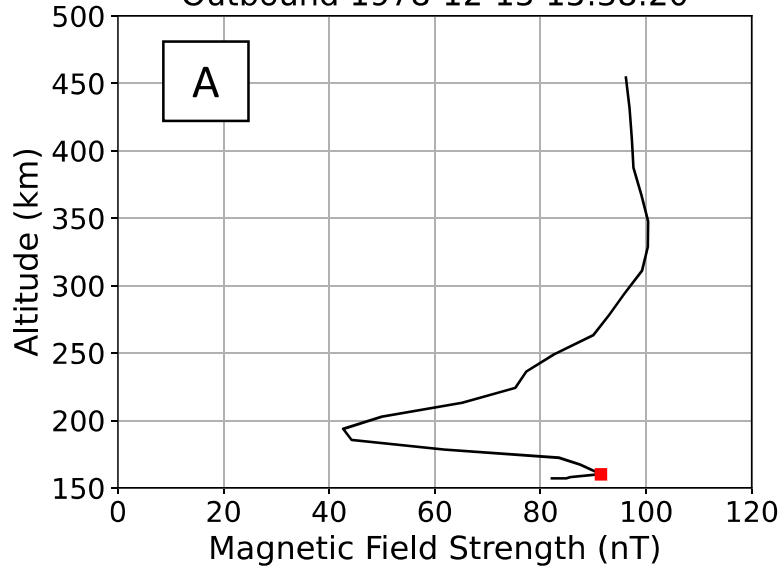
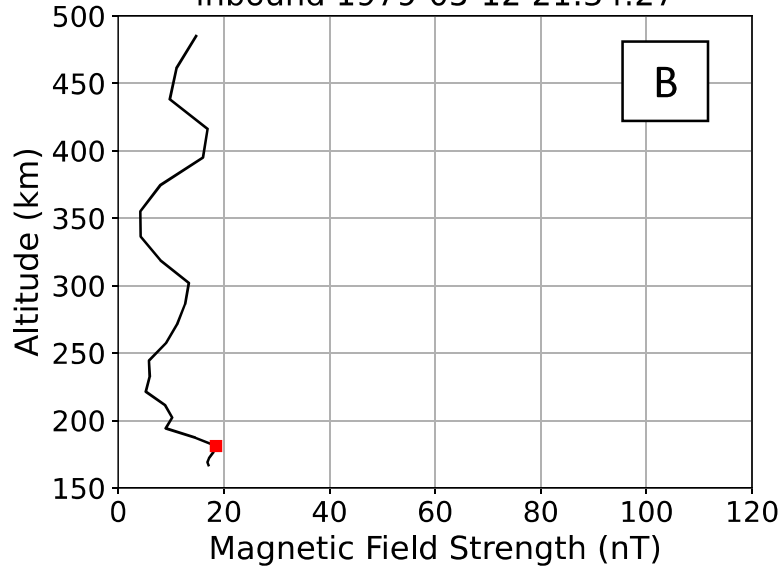


Figure 3.

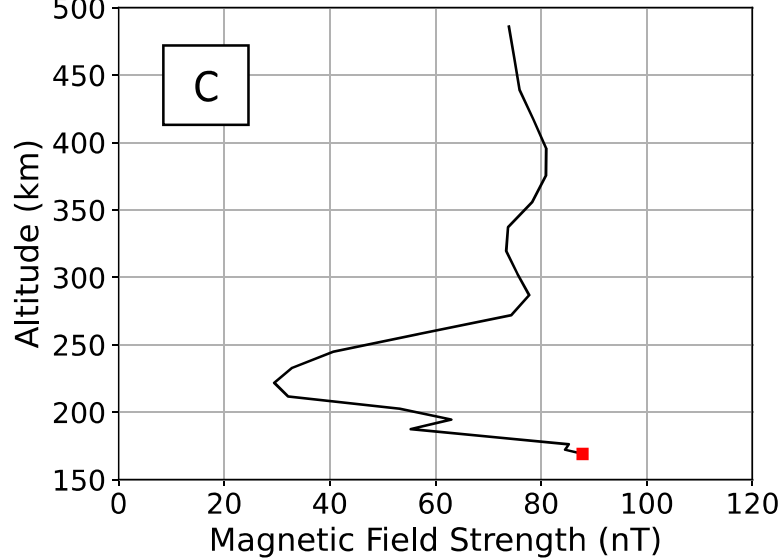
Outbound 1978-12-15 15:38:20



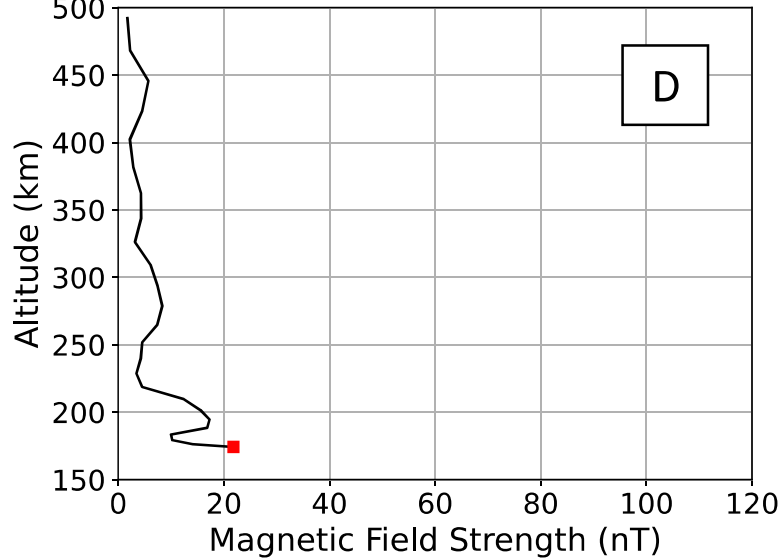
Inbound 1979-05-12 21:34:27



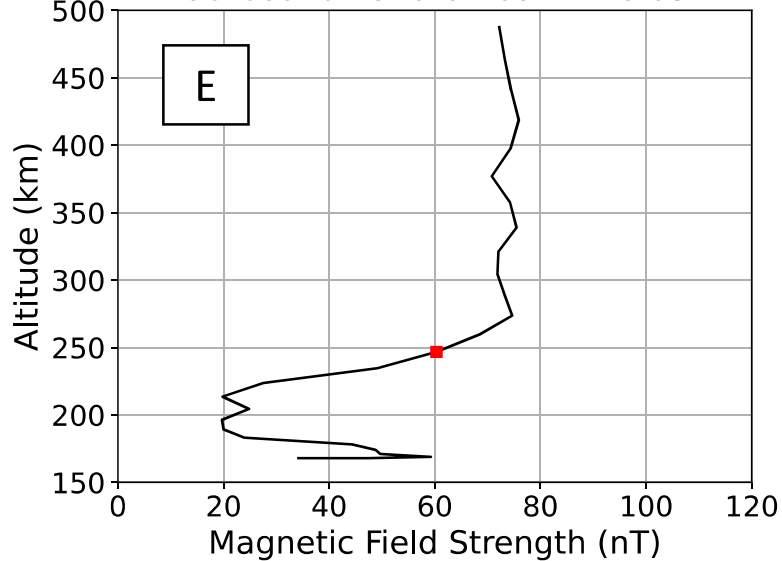
Inbound 1979-07-01 22:15:21



Inbound 1980-01-08 06:59:50



Outbound 1979-07-09 22:16:03



Outbound 1980-03-04 09:53:27

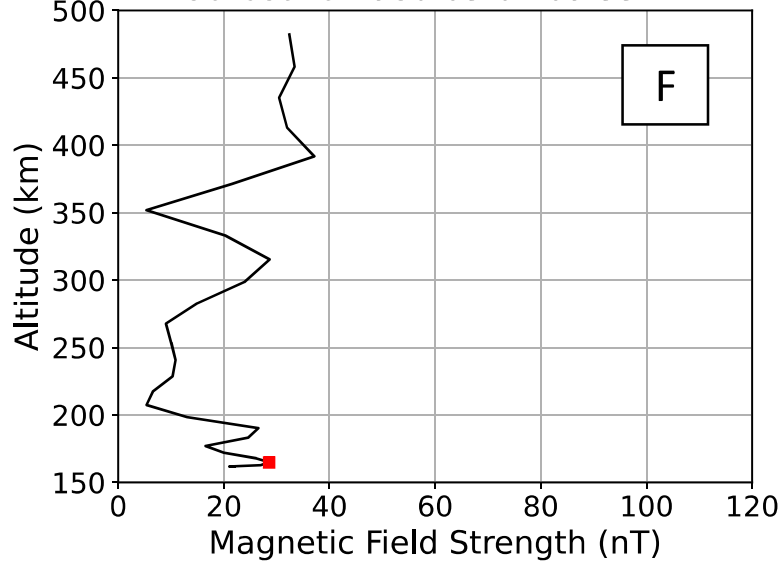
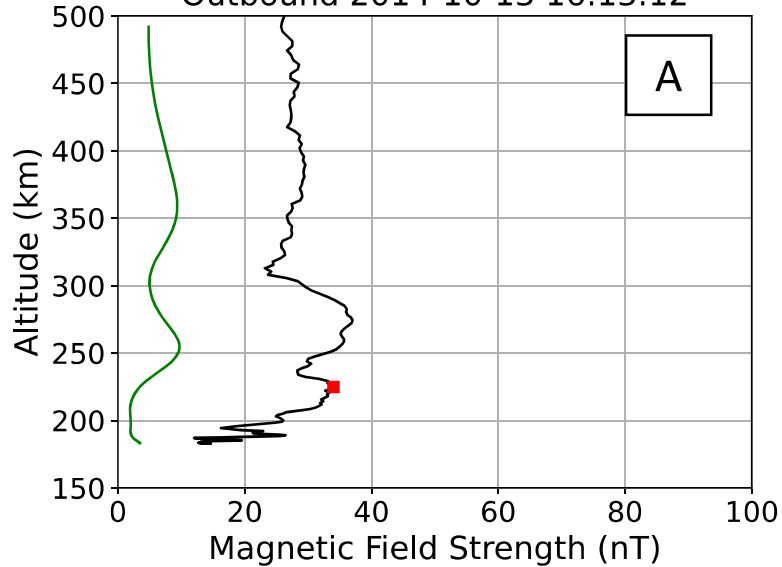
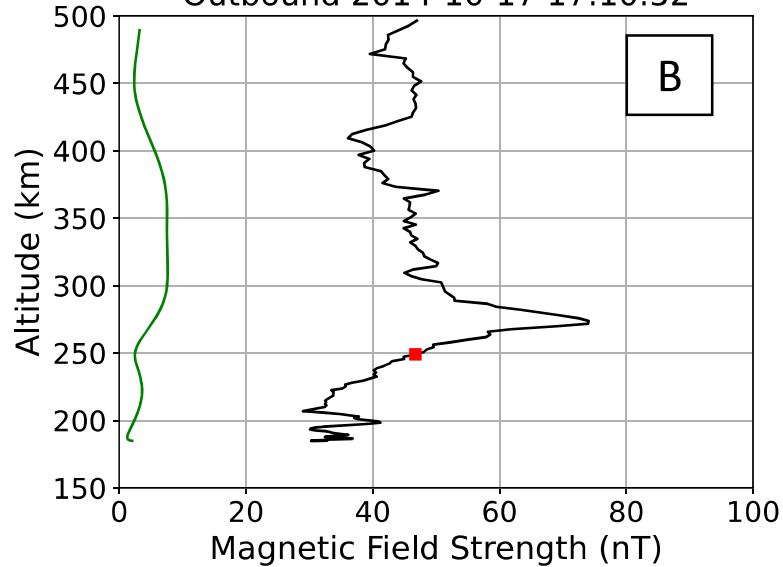


Figure 4.

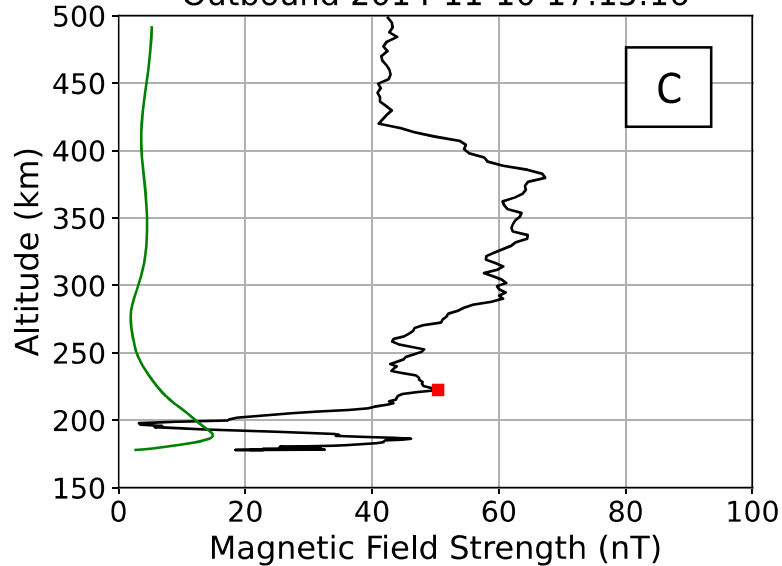
Outbound 2014-10-13 16:13:12



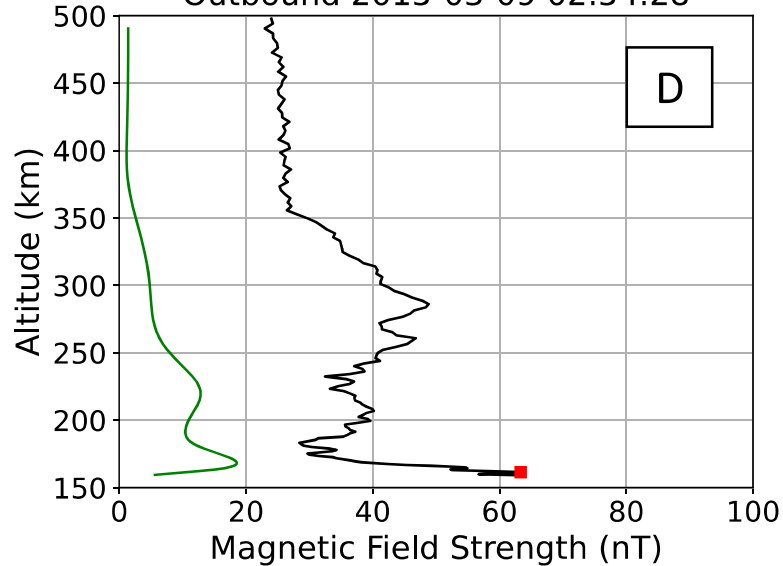
Outbound 2014-10-17 17:10:52



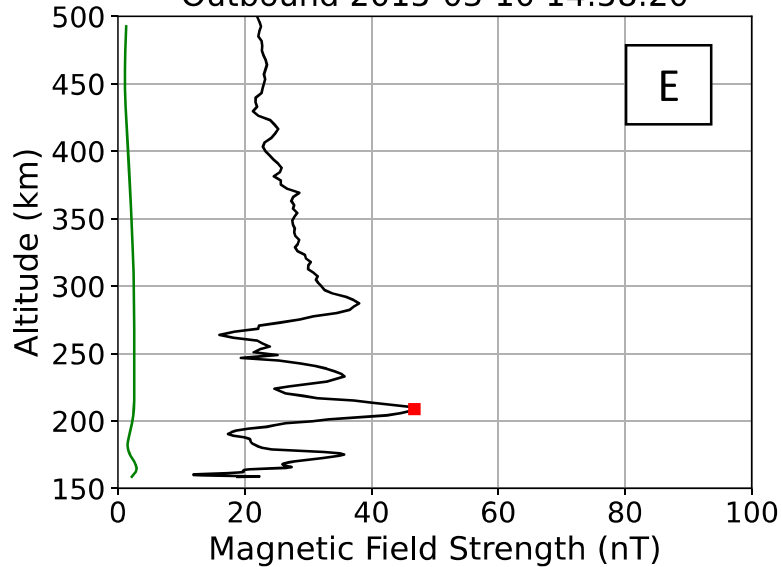
Outbound 2014-11-10 17:15:16



Outbound 2015-03-09 02:54:28



Outbound 2015-03-10 14:58:20



Inbound 2016-04-07 15:47:32

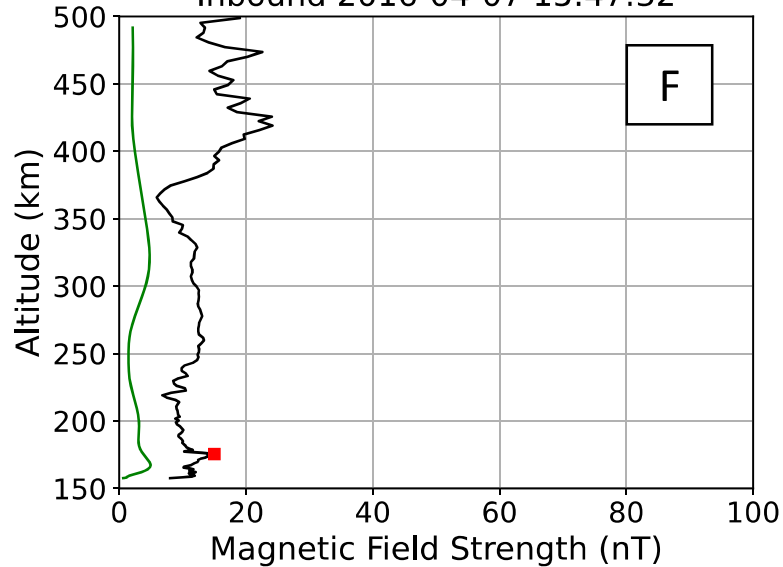
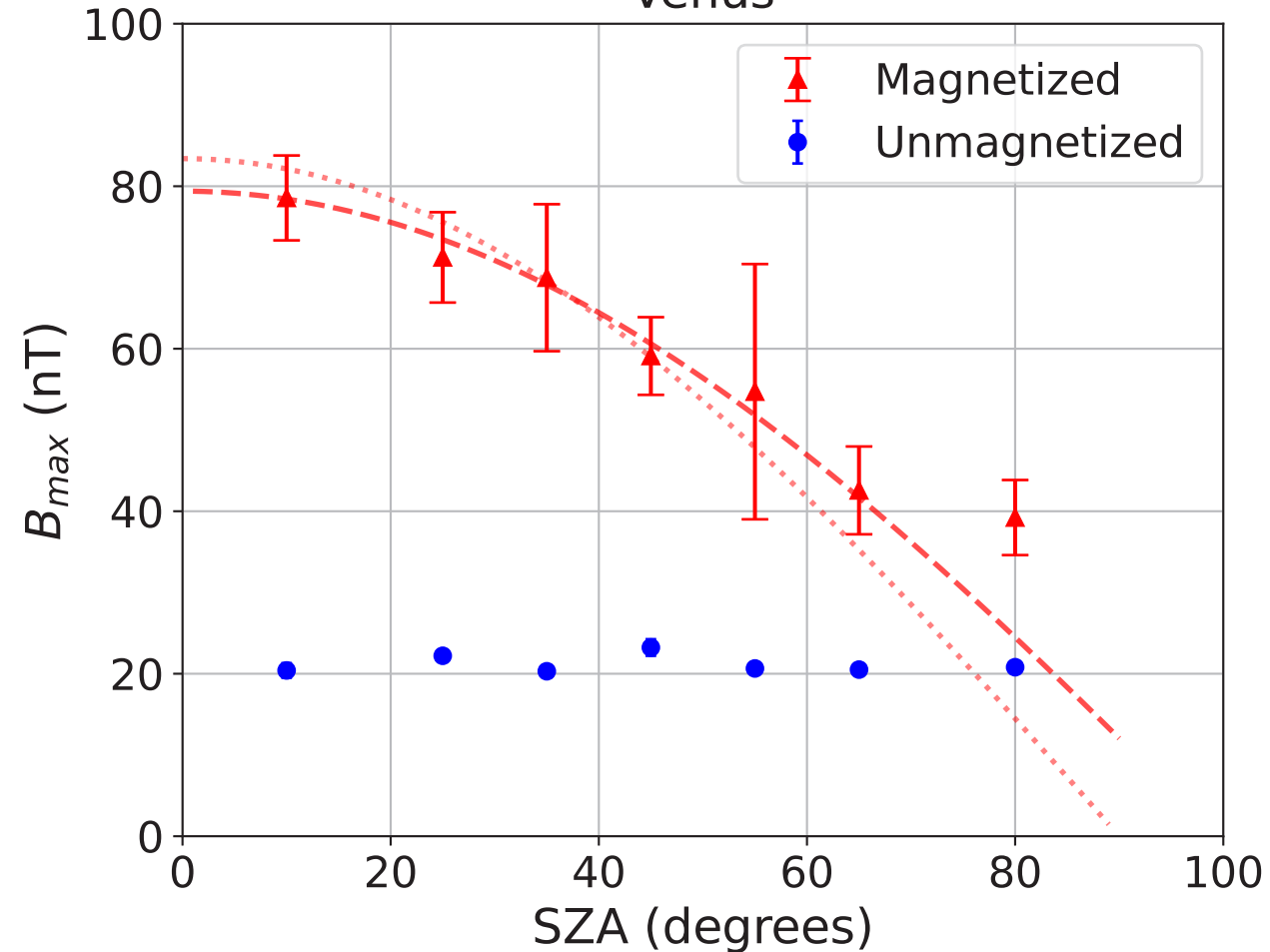


Figure 5.

Venus



Mars

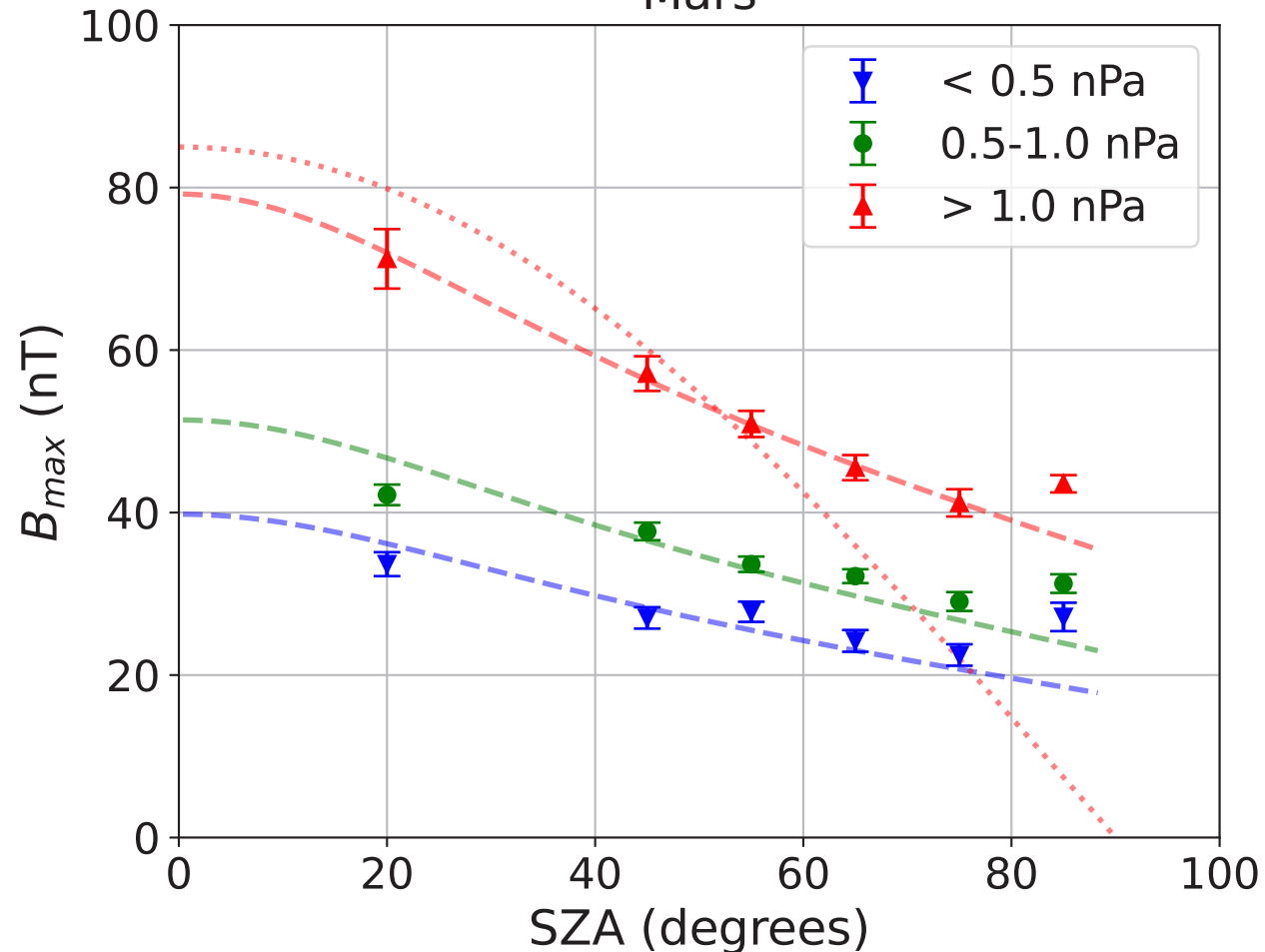


Figure 6.

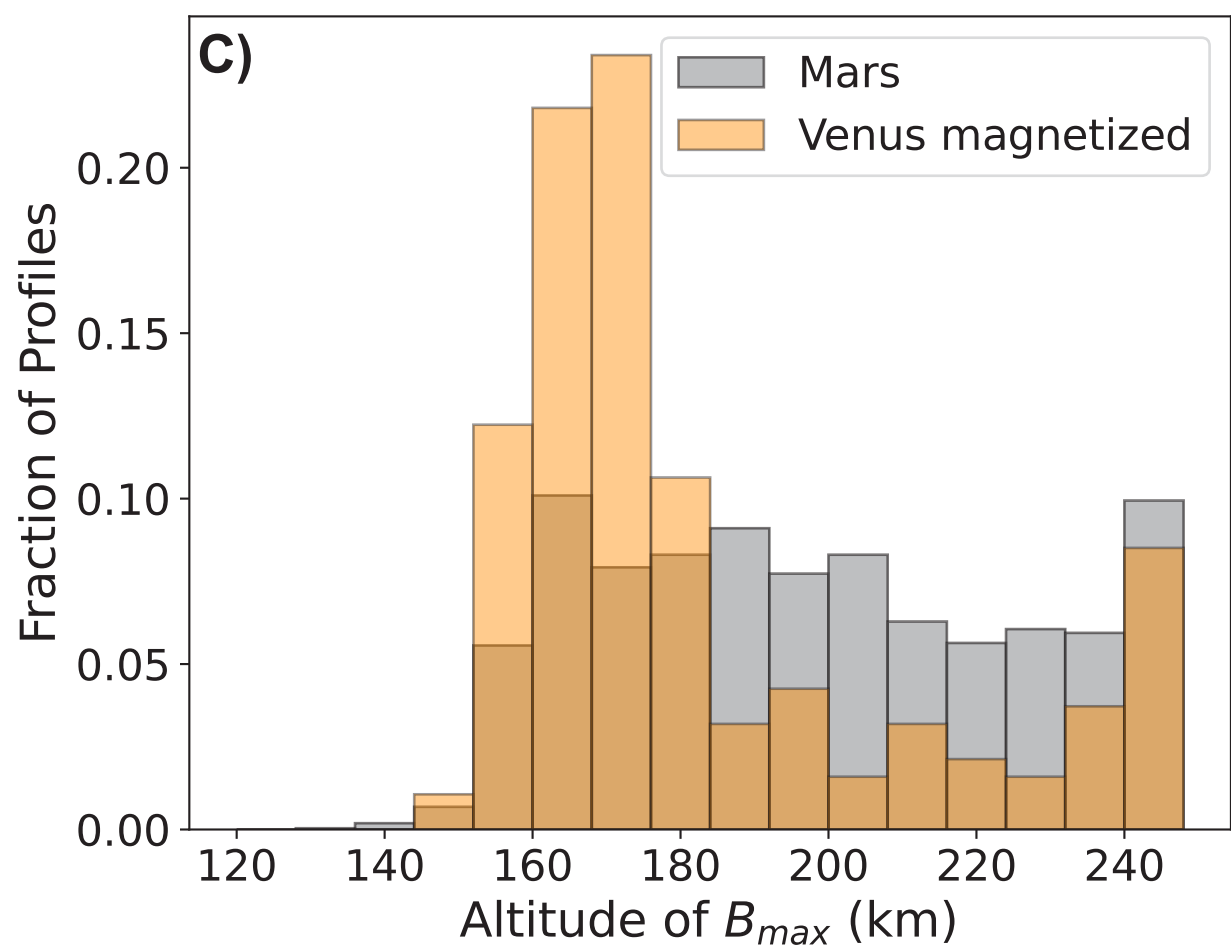
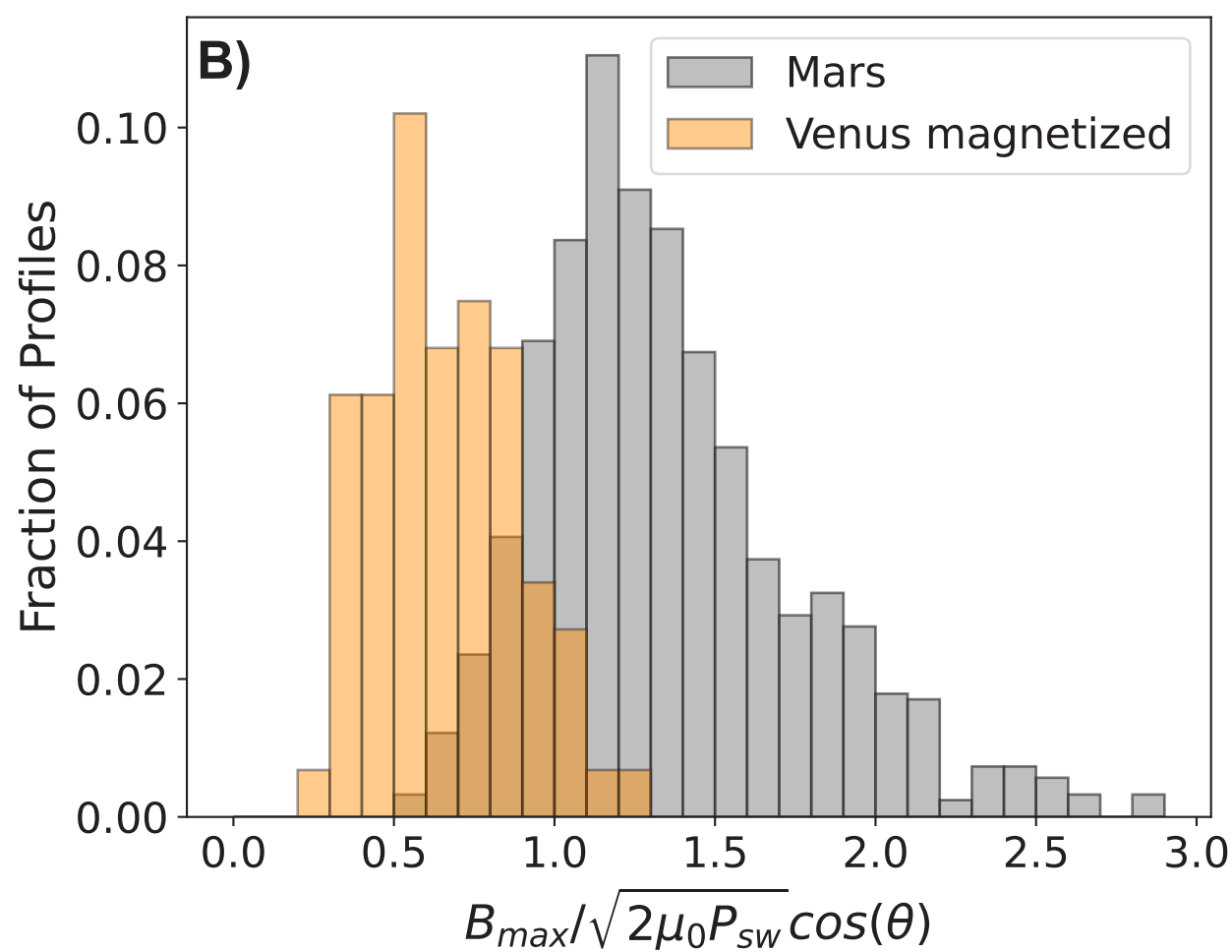
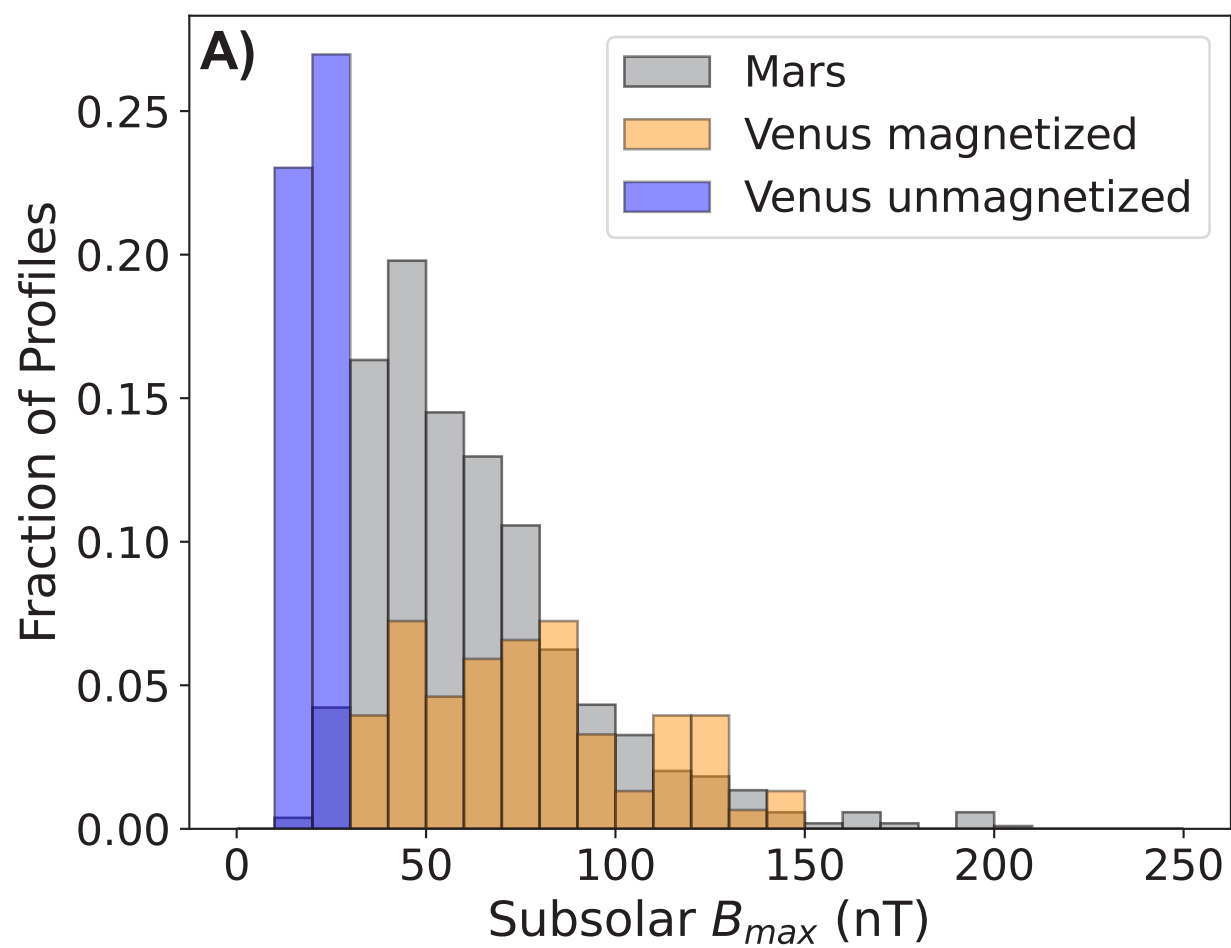
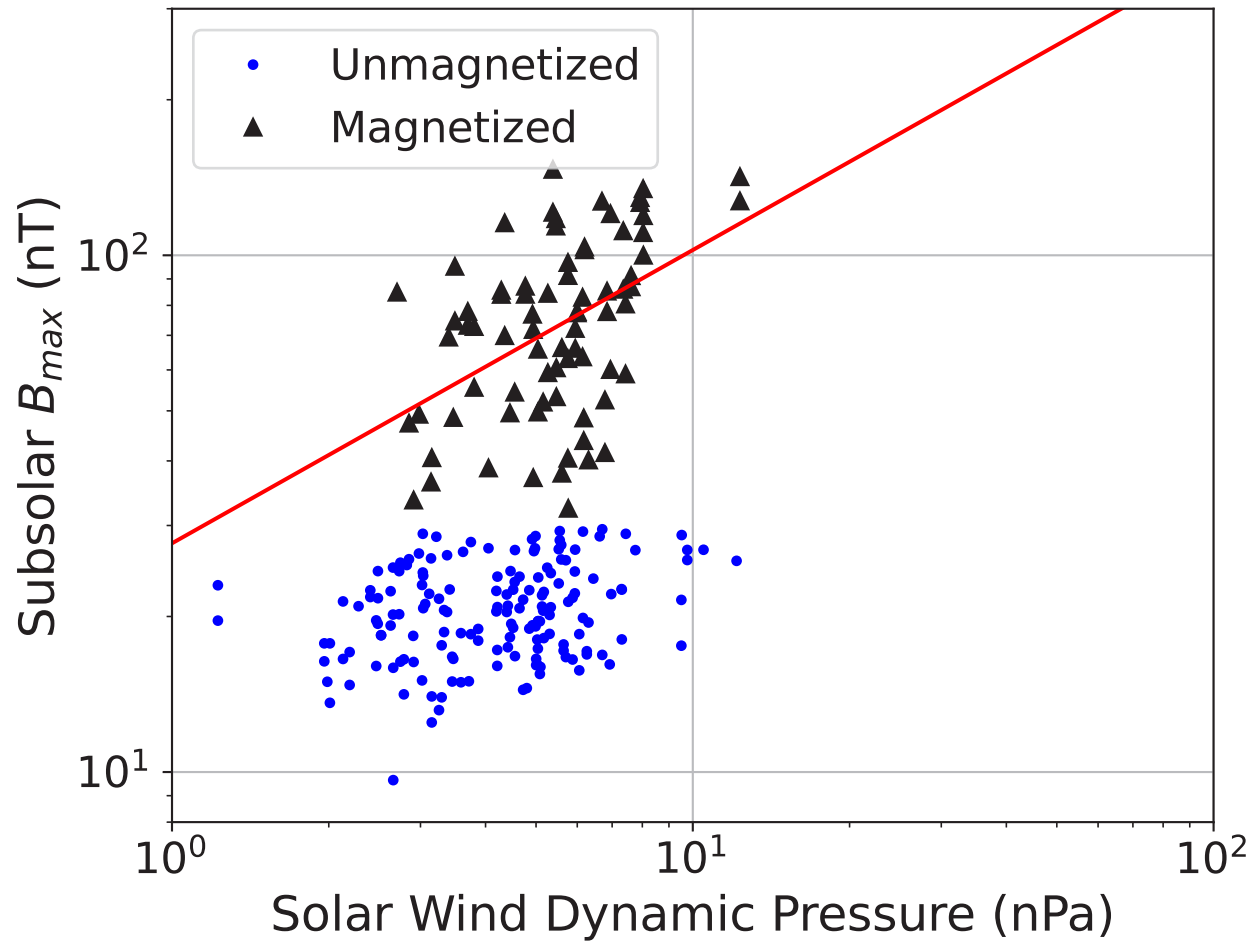
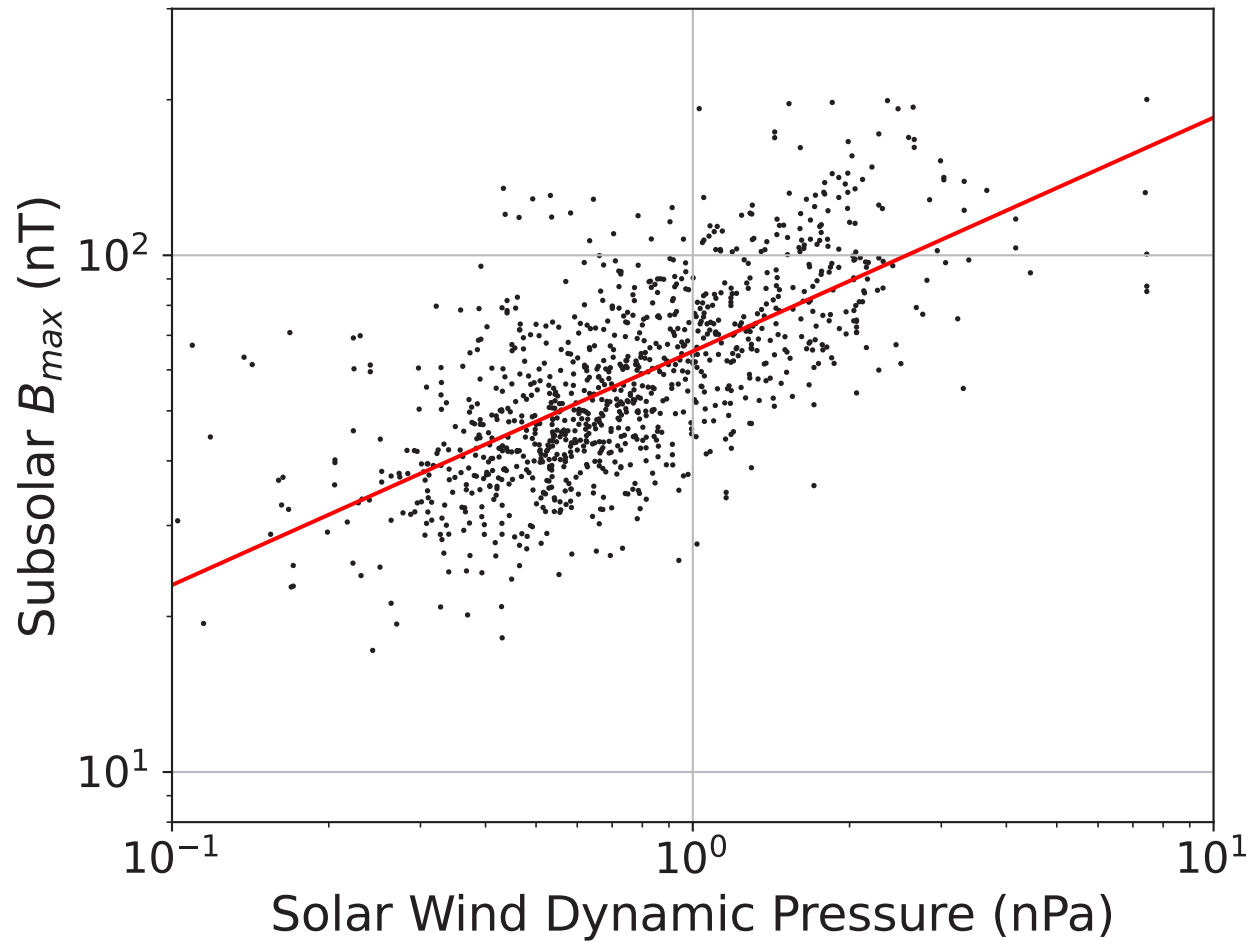


Figure 7.

Venus



Mars



Properties of Mars' Dayside Low-Altitude Induced Magnetic Field and Comparisons with Venus

Susanne Byrd¹, Zachary Girazian¹, Suranga Ruhunusiri²

¹Department of Physics and Astronomy, University of Iowa, Iowa City, IA

²Laboratory for Atmospheric and Space Physics, University of Colorado, Boulder, Boulder, CO, USA

Key Points:

- Unlike Venus, the induced magnetic field profiles at Mars are unable to be categorized into magnetized and unmagnetized states.
- At both planets, the solar zenith angle dependence of the induced field strength is controlled by the shape of the magnetic pileup boundary.
- Induced fields at Mars are stronger than expected if assuming the fields form to achieve pressure balance with the oncoming solar wind.

Corresponding author: Susanne Byrd, susbyrd@uiowa.edu

Abstract

Mars and Venus have atmospheres but lack large-scale intrinsic magnetic fields. Consequently, the solar wind interaction at each planet results in the formation of an induced magnetosphere. Our work aims to compare the low-altitude (< 250 km) component of the induced magnetic field at Venus and Mars using observations from Pioneer Venus Orbiter (PVO) and Mars Atmosphere and Volatile Evolution (MAVEN). The observations from Mars are restricted to regions of weak crustal magnetism. At Venus, it has long been known the vertical structure of the induced magnetic field profiles have recurring features that enable them to be classified as either magnetized or unmagnetized. We find the induced field profiles at Mars are more varied, lack recurring features, and are unable to be classified in the same way. The solar zenith angle dependence of the low-altitude field strength at both planets is controlled by the shape of the magnetic pileup boundary. Also, because the ionospheric thermal pressure at Venus is often comparable to the solar wind dynamic pressure, the induced fields are weaker than required to balance the solar wind by themselves. By contrast, induced fields at Mars are stronger than required to achieve pressure balance. Lastly, we find the induced fields in the magnetized ionosphere of Venus have a weaker dependence on solar wind dynamic pressure than the induced fields at Mars. Our results point to planetary properties, such as planet-Sun distance, having a major effect on the properties of induced fields at nonmagnetized planets.

1 Introduction

A magnetosphere is a region of space around a planetary body where charged particles are deflected by the body's magnetic field. For bodies with active intrinsic field generation, this region is usually large (e.g., ~ 10 planetary radii on the sun-facing side for Earth). For bodies without active intrinsic field generation, this region is smaller (< 1 planetary radii) and an induced magnetosphere forms as the magnetic field of the solar wind interacts with the electrically conductive ionosphere (Bertucci et al., 2011). As it encounters the obstacle, an electric current is induced in the ionosphere (Daniell Jr & Cloutier, 1977; Ramstad, 2020). The induced magnetosphere that results from this interaction tends to balance the dynamic pressure from the oncoming solar wind (Luhmann et al., 2004). Typically, an induced field is much weaker than an intrinsic global field. Induced magnetospheres occur on bodies that have an atmosphere but lack a dynamo-generated global magnetic field. Both Venus and Mars fall into this category as unmagnetized planets containing atmospheres, and thus both planets have induced magnetospheres. In this paper, we focus on understanding and comparing the structure and variability of the low-altitude (< 250 km) induced magnetic fields of Venus and Mars.

The Pioneer Venus Orbiter (PVO) is the only spacecraft to have consistently measured the low-altitude induced magnetic fields at Venus. Analyses of the PVO data confirmed that Venus has a magnetic field induced solely by interaction with the solar wind (Luhmann & Russell, 1983). They also found most vertical profiles of the induced magnetic field strength can, based on their features, be classified as either magnetized or unmagnetized (Luhmann et al., 1980; Luhmann & Cravens, 1991). When the solar wind pressure exceeds the peak ionospheric thermal pressure, the planet's induced field is classified as being in a magnetized state. In the magnetized state, the vertical profile contains a local minimum near 200 km and a local maximum near 170 km with peak field strengths up to 150 nT. Alternatively, when the solar wind pressure is less than the peak ionospheric thermal pressure, the ionosphere is in an unmagnetized state (Luhmann & Cravens, 1991). In the unmagnetized state, the ionosphere excludes most of the external field and the low-altitude induced field strength is weaker (< 30 nT). These profiles lack distinct maxima or minima at low altitudes, but instead contain many small-scale (~ 10 km) spikes characterized as flux ropes (Elphic et al., 1980; Phillips et al., 1984a; Elphic & Russell, 1983).

Some basic characteristics of the low-altitude field strengths in the magnetized ionosphere of Venus have also been reported. The low-altitude field strength was found to decrease with increasing solar zenith angle (SZA) (Luhmann & Cravens, 1991). Additionally, the field strength was found to increase with increasing solar wind dynamic pressure (Luhmann et al., 1980; Kar & Mahajan, 1987). Both of these variations are expected if pressure balance is satisfied across the near-space environment and the induced field is required to balance the dynamic pressure of the oncoming solar wind (Luhmann & Cravens, 1991; Sánchez-Cano et al., 2020). Starting in the pristine solar wind and moving inward, the dominant pressure terms are as follows: the dynamic pressure in the solar wind, the plasma thermal pressure in the sheath, the magnetic pressure in the magnetic pileup region, and the sum of the plasma thermal pressure and induced magnetic pressure below the magnetic pileup boundary. Essentially, the perpendicular component of the solar wind dynamic pressure is ultimately converted into magnetic pressure in the magnetic pileup region.

Mars Global Surveyor (MGS) provided the first comprehensive magnetic field measurements at Mars, discovering the total field is a combination of induced fields and crustal fields that are scattered across the planet (Connerney et al., 2001; Brain, 2003). However, MGS was unable to measure the induced magnetic field at low altitudes. Arriving at Mars in 2014, the Mars Atmosphere and Volatile EvolutioN (MAVEN) mission became the first spacecraft to routinely measure low-altitude magnetic fields. Recently, Fang et al. (2023) analyzed low-altitude magnetic field data from MAVEN. They found the induced field strength on the dayside is usually around 15-50 nT, decreases with increasing SZA, and increases with increasing solar wind dynamic pressure. Huang et al. (2023) found the vertical profiles often resemble a reversed “L”: above ~ 200 km the field has a constant value, and below ~ 200 km the field abruptly decreases in strength. Several studies have also examined the ubiquitous small scale features (10-50 km) present in the observed magnetic field profiles, including waves, slabs, flux ropes, and flux tubes (Hamil et al., 2022; Bowers et al., 2021; Cravens et al., 2023). These structures are thought to form through a variety of processes such as variations in the upstream solar wind, global plasma dynamics, and plasma instabilities.

Models have been used in attempt to reproduce the observed low-altitude magnetic field profiles at both planets. For Venus, models from the PVO era (Cloutier, 1984; Cravens et al., 1984; Luhmann et al., 1984; Shinagawa & Cravens, 1988; Luhmann & Cravens, 1991) and more recent iterations (Y. Ma et al., 2020, 2023), have been quite successful at reproducing the observed large-scale magnetic fields present in the magnetized ionosphere. They are able to reproduce several features of the magnetized profiles, including the local minimum near 200 km and the local maximum near 170 km (Cravens et al., 1984; Phillips et al., 1984b; Cloutier, 1984; Shinagawa & Cravens, 1988). Similar models for the induced field at Mars have been somewhat successful at reproducing the observed profiles (Shinagawa & Cravens, 1989; Y. J. Ma et al., 2017; Fang et al., 2018; Huang et al., 2023). Generally, however, the observed induced field profiles at Mars have more small-scale features that models are unable to fully reproduce.

In these models, the evolution of the induced magnetic field, B_{ind} , is described by the magnetic diffusion equation (Luhmann & Cravens, 1991):

$$\frac{\partial B_{ind}}{\partial t} = \nabla \times (u \times B_{ind}) - \nabla \times (\eta_m \nabla \times B_{ind}) \quad (1)$$

where t is time, u is the plasma flow speed, and η_m is the magnetic diffusivity. The first term in Equation 1 represents the convection of magnetic flux with plasma flow. The second term represents the diffusion or dissipation of the magnetic field as the electrical currents associated with the field are dampened through collisions (Luhmann & Cravens, 1991). At the top of the ionosphere, which is sometimes called the magnetic pileup bound-

ary or ionopause (Espley, 2018), densities are so low that the first term dominates and the draped solar wind field is convected into the ionosphere by downward flowing plasma. As the field is convected downward, the diffusion term eventually takes over as increased ion-neutral collisions between the induced current and neutral molecules causes the field to dissipate. The vertical structure of the induced magnetic field profile is, to first order, controlled by these processes. An interesting aspect of this picture is that variations in upstream solar wind conditions, such as a change in dynamic pressure, will not have an immediate affect in the low-altitude induced field because the effects take time to propagate through the sheath and into the ionosphere (Luhmann et al., 1984; Y. Ma et al., 2020; Hamil et al., 2022; Cravens et al., 2023).

In this work, our aim is to compare the structure and variability of the low-altitude induced magnetic fields at Venus and Mars. Our focus is on large scale structures as opposed to the small-scale structures like flux ropes. Our primary goals are to (1) investigate if the vertical structure of the induced magnetic field profiles at Mars can, like at Venus, be classified as magnetized or unmagnetized; (2) compare the induced field strengths at each planet and investigate if they are consistent with pressure balance, and (3) determine if the low-altitude induced magnetic field strengths vary with SZA and solar wind dynamic pressure in similar ways.

2 Data and Method

2.1 Pioneer Venus Orbiter

PVO collected the bulk of its low-altitude in situ measurements between December 1978 and July 1980 when its orbital period was 24 hours, and periapsis altitude was maintained near 160 km for nearly 700 orbits (Brace & Kliore, 1991). During this time, the periapsis segment evolved to cover a wide range of local times and solar zenith angles, but stayed near mid-latitudes throughout (10°S-40°N).

For magnetic field data, we use the low resolution magnetometer (OMAG) observations that have 12-second time resolution (C. T. Russell et al., 1980). The files contain the magnetic field vector, spacecraft altitude, solar zenith angle, and latitude of each observation. Each orbit is split into an inbound and outbound segment and the observations are trimmed to only include altitudes below 500 km. For upstream solar wind data, we use the upstream measurements from PVO that were obtained when PVO was located outside the bow shock. The IMF vector was measured by OMAG and the solar wind density and velocity were measured by the Plasma Analyzer instrument (Intriligator et al., 1980). The data are provided as hourly averages but we assign a single value to each half-orbit (inbound and outbound) by taking the solar wind measurement closest in time to the low-altitude magnetic field (periapsis) measurement. Periapsis segments without a solar wind measurement within 10 hours were not included. The dataset provides solar wind proton densities and velocities from which we calculate the dynamic pressure using $P_{sw} = \rho V^2$ where P_{sw} is the solar wind dynamic pressure, ρ is the solar wind mass density, and V is the bulk flow velocity.

2.2 MAVEN

The Mars low-altitude in situ measurements cover October 2014 through August 2020 when MAVEN's orbital period was 4.5 hours and periapsis altitude varied between ~ 150 -200 km. A handful of the observations come from times when periapsis was lowered down to ~ 125 km for week-long "deep dip" campaigns (Jakosky et al., 2015). The location of MAVEN's periapsis segment slowly evolves throughout the mission, covering a wide range of latitudes, local times, and SZAs. For magnetic field data, we use the Key Parameter (KP) data products. The KP data are a bundle that includes measurements from every MAVEN in situ instrument along with spacecraft ephemeris informa-

163 tion, all on a uniformly sampled 4-second time grid. The KP files are compiled from the
 164 instrument’s fully calibrated Level 2 data products. As with the Venus data, each or-
 165 bit is split into an inbound and outbound segment and trimmed to only include obser-
 166 vations at an altitude below 500 km.

167 For solar wind data, we use observations from MAVEN’s Magnetometer (MAG)
 168 and Solar Wind Ion Analyzer (SWIA) that were obtained while MAVEN was outside the
 169 bowshock. The data are derived using the method described in (Halekas et al., 2017),
 170 which provides averages of solar wind properties for each orbit. The SWIA observations
 171 contain the solar wind proton density and velocity which are used to calculate the so-
 172 lar wind dynamic pressure. Periapsis segments without a solar wind measurement within
 173 10 hours were not included. However, many of the orbits do not have upstream solar wind
 174 measurements within 10 hours of the periapsis observations. To fill these gaps, we use
 175 the Ruhunusiri et al. (2018) solar wind proxy model, which predicts upstream solar wind
 176 conditions based on MAVEN observations in the sheath. Of the 2625 MAVEN profiles
 177 in the final dataset, 1151 were assigned upstream conditions based on SWIA observa-
 178 tions, 1069 were assigned from the proxy model, and 405 could not be assigned.

179 **2.3 Caveats**

180 When comparing results derived from the MAVEN and PVO observations, several
 181 differences between the two datasets must be considered. First, the PVO data were ob-
 182 tained during the maximum of Solar Cycle 21 (Brace & Kliore, 1991), while the MAVEN
 183 data were obtained during the declining phase of the rather weak Solar Cycle 24 (Lee
 184 et al., 2017). Second, the PVO periapsis is confined to mid-latitudes, while the MAVEN
 185 periapsis covers latitudes between 75° N and 75° S (see Figure 1). Additionally, because
 186 the spacecraft moves both vertically and horizontally during each periapsis pass, the struc-
 187 tures we observe in the magnetic field profiles may not strictly be in the vertical direc-
 188 tion.

189 Differences between the planets themselves must also be kept in mind when com-
 190 paring results from the two planets. For example, Mars has rather pronounced seasons
 191 due to its eccentric orbit and 25° axial tilt, while Venus has no seasons because of its cir-
 192 cular orbit and $< 3^\circ$ axial tilt. Other differences to consider include, but are not lim-
 193 ited to, planetary rotation rate, the presence of crustal magnetic fields at Mars but not
 194 Venus, planetary size, and planet-Sun distance.

195 **2.4 Method**

196 The vertical structure of the induced magnetic field profiles at Venus can gener-
 197 ally be categorized into one of two states: ”magnetized” or ”unmagnetized”. We cate-
 198 gorize the Venus profiles in this manner based on the descriptions in Luhmann and Cravens
 199 (1991). If the global minimum of a trimmed magnetic field profile is below 300 km, and
 200 the profile has low-altitude (< 250 km) maximum field strength greater than 30 nT, it
 201 is classified as magnetized. If a profile has a low-altitude magnetic field strength greater
 202 than 50 nT, it is also classified as magnetized. Alternatively, If a profile has a low-altitude
 203 maximum field strength less than 30 nT, it is classified as unmagnetized. A small num-
 204 ber of profiles remain categorized because they do not match either criteria.

205 Figure 3 shows six examples of Venus magnetic field profiles observed by PVO. The
 206 examples in the left column show magnetized profiles. They contain a peak below 200
 207 km, a wide minimum near 200-250 km, and a nearly-constant topside. These features
 208 are all absent in unmagnetized profiles, examples of which are shown in the right col-
 209 umn of Figure 3. Instead, the unmagnetized profiles are nearly featureless, lacking dis-
 210 tinct maxima or minima, and have weaker field strengths at nearly all altitudes.

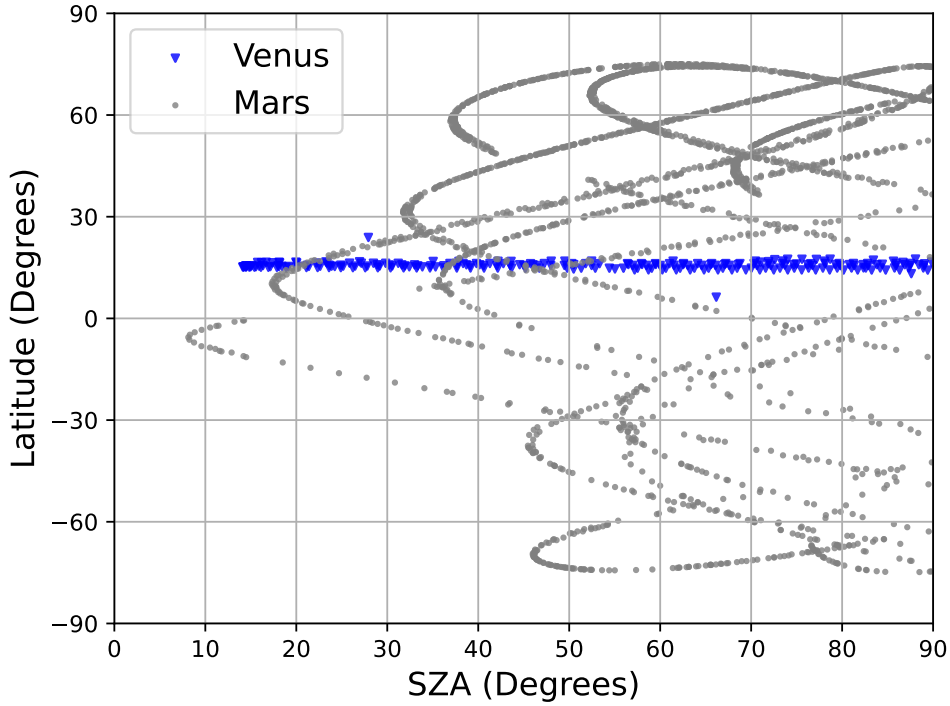


Figure 1: The latitudes and solar zenith angles at periapsis for the orbits used in this study, demonstrating the observational coverage of PVO (blue triangles) and MAVEN (gray circles) are quite different.

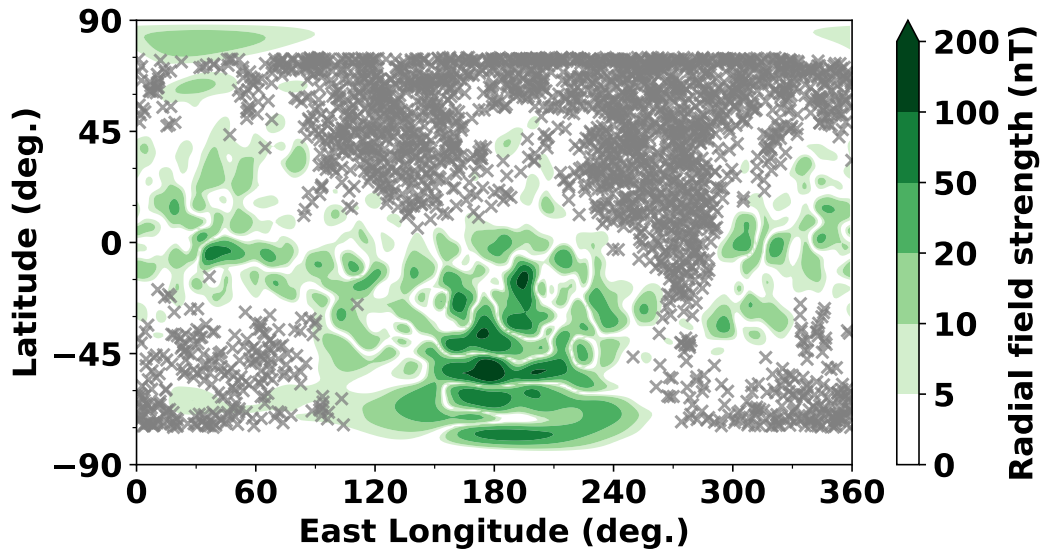


Figure 2: Locations of the MAVEN observations used in our analysis. Grey X's show locations of low-altitude maximum magnetic field strengths (B_{max}) for each inbound and outbound profile. Green contours are a map of the Martian radial crustal field strength at 400 km (Morschhauser et al., 2014). These locations are chosen because they are from weak crustal field regions, making them more comparable to Venus.

Figure 4 shows six examples of magnetic field profiles observed by MAVEN. These profiles are much more complicated than profiles from Venus and they lack recognizable features that would allow them to be sorted easily into two categories. This issue will be explored further in Section 3.1.

Since we are interested in comparing the strength and variability of the low-altitude induced fields at Venus and Mars, we focus our analysis on the maximum magnetic field strength below 250 km altitude (B_{max}). To derive B_{max} for both inbound and outbound segments of an orbit, we locate the maximum field strength below 250 km. This altitude cutoff of 250 km was chosen because it will capture the low-altitude peaks around 170 km in the magnetized profiles at Venus (Luhmann & Cravens, 1991), and be flexible enough to capture peaks in the Mars profiles at a wide range of altitudes. The B_{max} derived from each Venus profile is marked in Figure 3. For magnetized profiles, B_{max} is the field strength at the location of the low-altitude peak near 170 km. For unmagnetized profiles, B_{max} is the maximum field strength below 250 km, but is not at the location of any specific feature. The same method is used to extract B_{max} from the Mars profiles, which are marked in Figure 4. Since the vertical structure varies much more from profile to profile, the derived B_{max} is not extracted from a recurring distinct feature, as in the case of the magnetized Venus profiles.

We note that there are several cases when the location of the derived B_{max} is either at the bottom of the profile (periapsis) or at the top of the profile (near the top altitude cutoff of 250 km). For cases when the derived B_{max} is near the top of the profile, the low-altitude field strength never exceeds the field strength at 250 km. Examples of this case can be seen in Figures 3E and 4B. For these, B_{max} is likely overestimated because our method does not pick any low-altitude feature that has a local maximum below 250 km. For cases when B_{max} is near periapsis, the derived B_{max} likely underestimates the true local maximum in the low-altitude magnetic field profile because the true maximum may reside below periapsis where there are no observations. Examples of this case can be seen in Figure 3C and 4D. With these caveats in mind, we include these cases in our final dataset.

Another important consideration is the crustal magnetic fields at Mars that are not at Venus. We wish to remove these crustal fields from our analysis to enable a more direct comparison between the two planets, focusing solely on the induced component of the magnetic field. The Morschhauser et al. (2014) empirical model of crustal magnetic field strength is used to omit MAVEN observations where the crustal field strength is comparable to the induced field strength. More concretely, we exclude any profiles that have $B_{crust}/B_{max} > 0.2$ where B_{crust} is the crustal field strength at the location of B_{max} . Figure 2 shows the locations of B_{max} that remain after applying this crustal field filtering. It demonstrates the chosen B_{max} 's are confined to outside the crustal field regions.

To focus on the dayside interaction region, in our final dataset we only use profiles that have B_{max} at $SZA < 90^\circ$. In total, the final filtered dataset for Venus includes 475 magnetic field profiles of which 188 are categorized as magnetized, 260 as unmagnetized, and 27 as uncategorized. Of the 188 magnetized profiles, 39 have B_{max} at the bottom of the profile and 25 have B_{max} at the top altitude cutoff of 250 km. Of the 260 unmagnetized profiles, 6 have B_{max} at the bottom of the profile and 30 have B_{max} at 250 km. The final filtered dataset for Mars includes 2625 profiles. Of these, 220 have B_{max} at the bottom of the profile and 112 have B_{max} at the top altitude cutoff of 250 km.

3 Analysis

3.1 Categorizing the Magnetic Field Profiles

As discussed in Section 2.4 and shown in Figure 3, the induced magnetic field profiles at Venus have recurring vertical structures that can generally be categorized as ei-

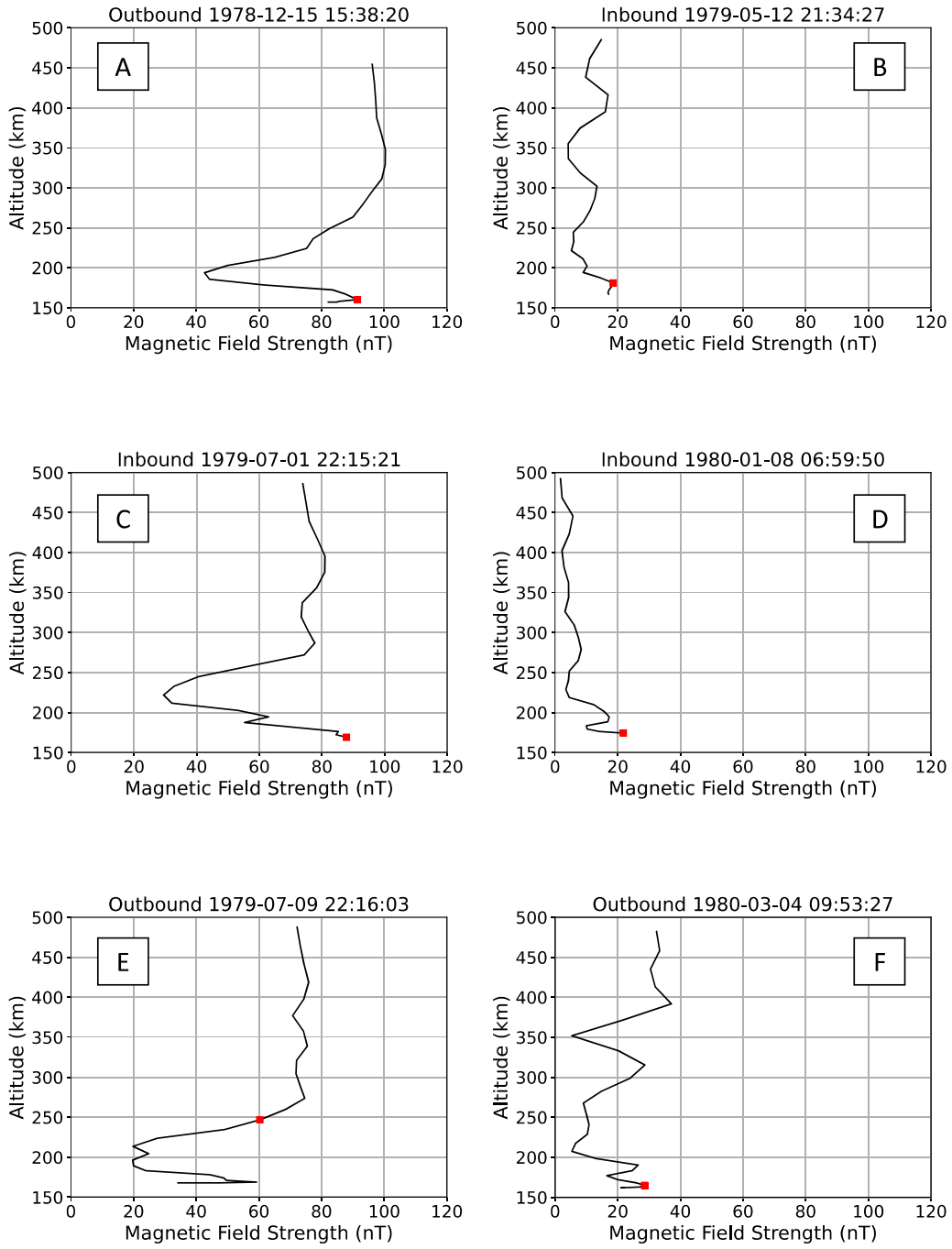


Figure 3: Examples of magnetic field profiles from Venus with magnetized states in the left column and unmagnetized states in the right column. The squares mark the derived B_{max} for each profile.

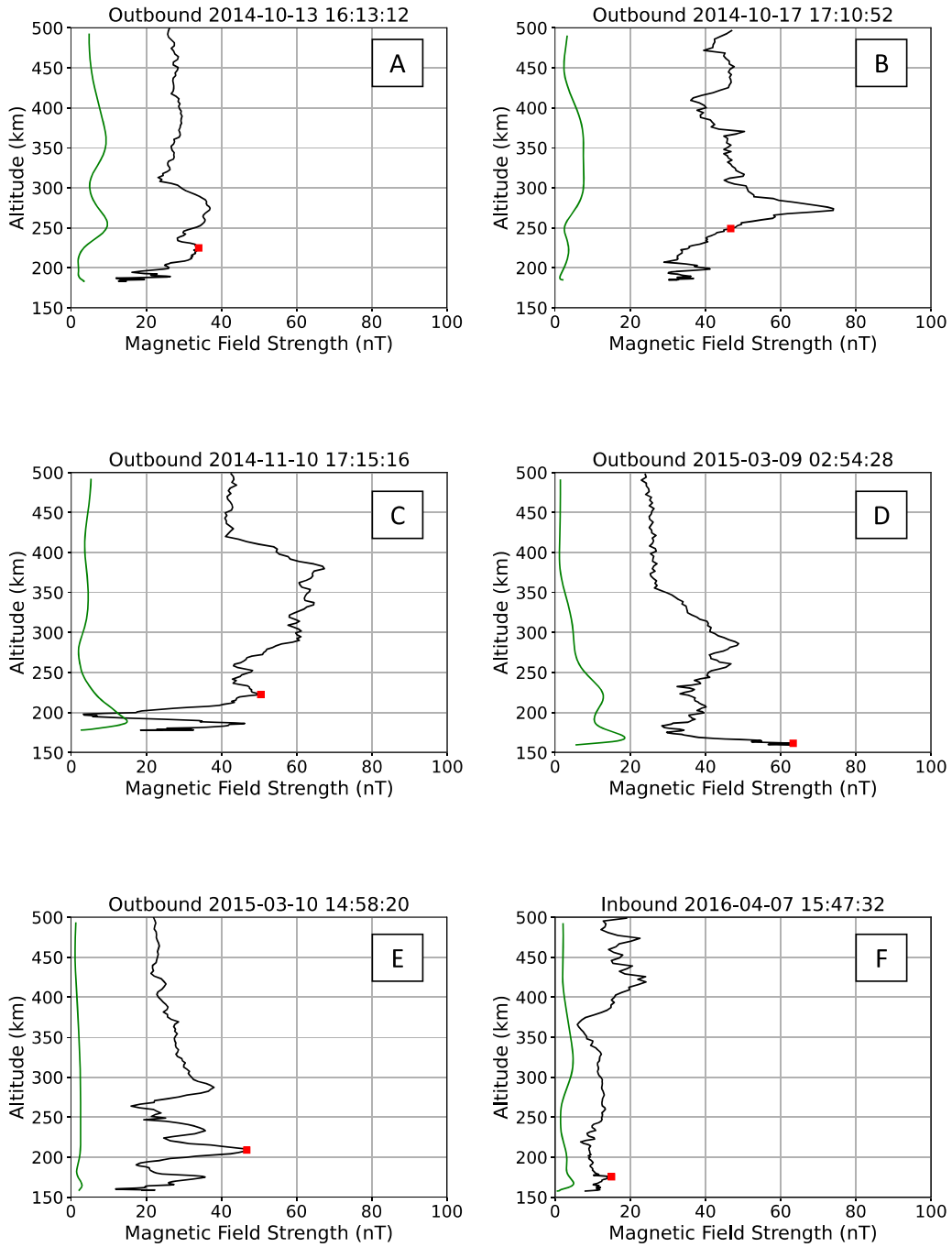


Figure 4: Examples of magnetic field profiles from Mars. The black lines are the measured magnetic field from MAVEN and the green lines are the crustal magnetic field strength from the Morschhauser et al. (2014) crustal field model. The red squares mark the derived B_{max} for each profile.

ther “magnetized” or “unmagnetize” (Luhmann & Cravens, 1991). Using our classification criteria, we find $\sim 40\%$ of the profiles can be classified as magnetized and $\sim 55\%$ can be classified as unmagnetized. These percentages are loosely consistent with the occurrence rates reported by Luhmann et al. (1980), who categorized 30% as magnetized and 70% as unmagnetized. However, they used somewhat different classification criteria.

We attempted to categorize the Mars profiles based on visual inspection but quickly found they could not be categorized into Venus-like magnetized and unmagnetized vertical structures. This is demonstrated in Figure 4, which shows the Mars profiles lack distinct features that would enable them to be easily categorized. In particular, they lack a consistent minimum near 300 km or a clear single low-altitude peak, features that are present in the Venus magnetized profiles. Instead, the Mars profiles are more varied and have more complex small-scale structures (tens of kilometers). These structures are present even when the crustal field component is much lower than induced field strength.

We conclude the vertical structure of the induced magnetic fields at Mars are too varied to be classified into simple magnetized and unmagnetized states. Further, it is generally accepted that Mars is magnetized more often than Venus, meaning the ionospheric thermal pressure is usually insufficient to exclude the external field from penetrating into the ionosphere (Zhang & Luhmann, 1992; Chu et al., 2021; Holmberg et al., 2019; Sánchez-Cano et al., 2020). Profiles resembling the magnetized ionosphere of Venus, such as the profile shown in Figure 4C, do exist but are quite rare.

Although the induced magnetic field profiles at Mars are unable to be categorized into simple states like at Venus, there are some reoccurring features that are worth reporting. First, the profiles often have a distinct prominent peak between 250-300 km. Examples of such profiles can be seen in Figure 4A, B, and D. Some profiles have many peaks, such as the one shown in Figure 4E. These multiple peaks at low altitudes may be due to a combination of both horizontal and vertical variations in the magnetic field strength (the spacecraft trajectory is not strictly vertical). Generally, magnetized profiles at Venus lack such a complicated structure.

Neither the complicated multi-peaked structures, nor a peak between 250-300 km were predicted by the earliest MHD models (Shinagawa & Cravens, 1989). More recent MHD studies that include the time-dependent effects of changing solar wind conditions do predict more complicated structures including a peak between 250-350 km (Y. J. Ma et al., 2014, 2017). The peaks are caused by vertical gradients in the downward plasma flow speed as a result of solar wind pressure variations on hour long timescales. Solar wind variations may be responsible for some of these small scale features (Cravens et al., 2023), but other processes such as plasma instabilities and global plasma dynamics likely play a role (Hamil et al., 2022).

3.2 Solar Zenith Angle Variations

To first order, we expect pressure balance to be maintained through the space environment. Given this assumption, the maximum induced magnetic field strength should depend on the solar wind dynamic pressure and the ionospheric thermal pressure. To achieve pressure balance, higher solar wind dynamic pressures should lead to stronger induced fields, while higher ionospheric thermal pressures should be able to exclude the solar wind field more efficiently, resulting in weaker induced fields. Mathematically, if pressure balance is satisfied throughout the low-altitude ionosphere then

$$P_{sw} \cos^2(\chi) = P_{th} + P_B \quad (2)$$

307 where $P_{sw}\cos^2\chi$ is the normal component of the solar wind dynamic pressure (Crider
 308 et al., 2003), χ is SZA, P_{th} is the ionospheric thermal pressure, and $P_B = B_{ind}^2/2\mu_o$
 309 is the induced magnetic field pressure. If we also assume $P_B \gg P_{th}$, which is often the
 310 case at Mars (Holmberg et al., 2019; Sánchez-Cano et al., 2020), then we expect the in-
 311 duced field strength to approximately follow

$$B_{ind} = (2\mu_o P_{sw})^{1/2} \cos(\chi) \quad (3)$$

312 where μ_o is the vacuum permeability. This equation predicts that, when magnetized ($P_B >$
 313 P_{th}), the induced magnetic field strength should be approximately proportional to co-
 314 sine of the SZA. We examine this prediction for both Venus and Mars.

315 Figure 5 shows B_{max} plotted against SZA for both planets. The Venus observa-
 316 tions are separated into their magnetized and unmagnetized classifications, but not sep-
 317 arated based on solar wind dynamic pressure because of data scarcity. The Mars obser-
 318 vations are sorted into groups based on solar wind dynamic pressure since the induced
 319 field will increase with increasing solar wind pressure (see Section 3.4). The data are binned
 320 along the SZA axis using uneven bin sizes so that each bin has a comparable number of
 321 data points.

322 At Venus the maximum field strengths of the unmagnetized profiles do not have
 323 a SZA dependence and are around 20 nT, which is consistent with previous studies (Elphic
 324 et al., 1984). The low field strengths are expected because, when unmagnetized, the ex-
 325 ternal magnetic field is excluded from the ionosphere by the high ionospheric thermal
 326 pressure, and thus the induced field strength is not expected to be driven by the solar
 327 wind pressure. In these cases $P_B \ll P_{th}$ so Eq. 3 is not applicable and we do not ex-
 328 pect any cosine dependence. In contrast, the maximum field strengths of the magnetized
 329 profiles decrease with increasing SZA up to a SZA of $\sim 65^\circ$. The bin-averaged maximum
 330 field strength decreases from ~ 80 nT near the subsolar point to ~ 40 nT near 65° SZA.
 331 This is consistent with previous work which has shown that this SZA trend is approx-
 332 imately satisfied in the magnetized Venus ionosphere, but the analysis was conducted
 333 with few observational data points (C. Russell et al., 1983).

334 Similarly, the maximum field strengths at Mars decrease from ~ 70 nT (35 nT) at
 335 the subsolar point to ~ 40 nT (25 nT) around 75° SZA during high (low) solar wind dy-
 336 namic pressure. There is also clear separation between the dynamic pressure bins, with
 337 higher maximum field strengths occurring during higher solar wind dynamic pressures,
 338 as predicted by Equation 3. The solar wind dynamic pressure trends at both planets will
 339 be further explored in Section 3.4.

340 The dotted lines shown in Figure 5 are fits to the data using SZA for χ in Equa-
 341 tion 3. Specifically, we fit the binned averages to $B_{max} = B_0 \cos(\chi)$ where B_0 is a fit
 342 parameter that represents the subsolar induced field strength. In both cases, the data
 343 are poorly fit. We suggest this deviation from the prediction is a consequence of SZA
 344 being only an approximation of the angle between the solar wind bulk flow velocity and
 345 the obstacle. We refit the data after replacing χ with θ , where θ is the angle between
 346 the solar wind flow and the MPB (Crider et al., 2003). For Venus we use the MPB shape
 347 found by Xu et al. (2021) and for Mars we use the MPB shape given in Vignes et al. (2000).
 348 The fits are markedly improved when using θ in place of SZA. It is especially apparent
 349 at Mars that the trend follows the shape of the MPB rather than of cosine of SZA. The
 350 fit parameter (B_0) for Venus is 79.5 ± 0.9 . The fit parameters for Mars are 79.2 ± 0.4 , 51.7 ± 2.0 ,
 351 and 40.1 ± 1.4 for the high, medium, and low solar cases, respectively.

352 From these two plots we conclude low-altitude maximum field strength follows the
 353 predicted cosine trend (Eq. 3) up to at least 60° when in a magnetized state, but only
 354 if the angle between the solar wind flow and the MPB is used (θ). However, near the ter-

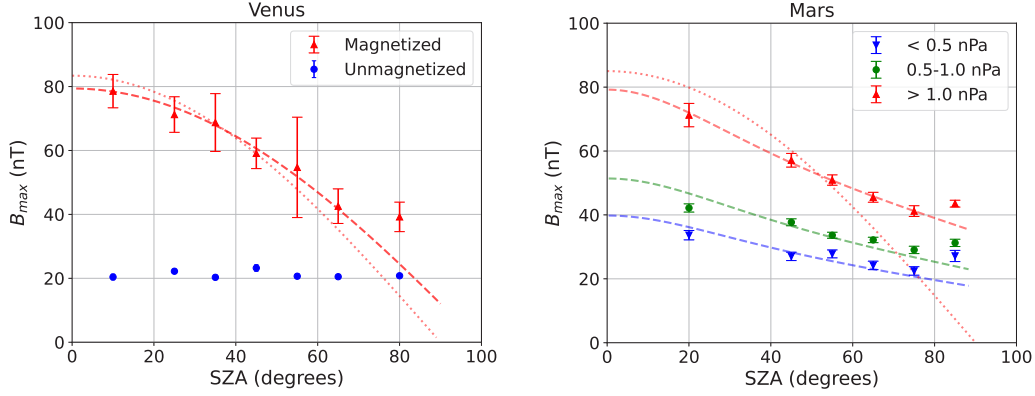


Figure 5: The solar zenith angle (SZA) variation of B_{max} for Venus (left) and Mars (right). The dotted lines are fits to $B_{max} = B_0 \cos(\chi)$ (see Equation 3) using SZA for χ . The dashed lines are fits using θ (the angle between the solar wind flow and the magnetic pileup boundary) in place of χ (Vignes et al., 2000; Xu et al., 2021). The Venus data are sorted into magnetized and unmagnetized cases while the Mars data are sorted into solar wind dynamic pressure bins. Error bars show the standard error in each bin. The solar zenith angle bins for Venus have edges at 0° , 20° , 30° , 40° , 50° , 60° , 70° , and 90° . The SZA bins for Mars have edges at 0° , 40° , 50° , 60° , 70° , 80° , and 90° .

355 minator B_{max} is higher than predicted at both planets. We currently do not have an ex-
 356 planation for this observed deviation.

3.3 Peak Magnetic Field Distributions

357
 358 In Figure 6A, we plot histograms of B_{max} with the Venus data separated into mag-
 359 netized and unmagnetized categories (Section 3.1). All the B_{max} values from Mars and
 360 all the magnetized B_{max} values from Venus are corrected to the subsolar point by di-
 361 viding them by $\cos(\theta)$. Only B_{max} values at $\text{SZA} < 60^\circ$ are included (Section 3.2). The
 362 histogram of the unmagnetized B_{max} values at Venus form a sharp peak around 20 nT,
 363 which is the typical magnitude of the induced field when unmagnetized. The histogram
 364 of the magnetized B_{max} values at Venus form a much wider distribution, but demon-
 365 strates the clear demarcation between magnetized and unmagnetized states. The mag-
 366 netized distribution has a mean of $77.8 (\pm 29.2)$ nT and a median of 75.7 nT. Compar-
 367 atively, the distribution of the Mars B_{max} values has a mean of $62.9 (\pm 29.4)$ nT and a
 368 median of 55.7 nT.

369 At the subsolar point, Equation 3 predicts $B_{max} = (2\mu_0 P_{sw})^{1/2}$ (Fang et al., 2023).
 370 Since P_{sw} scales as the inverse square of the planet-Sun distance, we expect larger B_{max}
 371 values at Venus than Mars, which is confirmed in Figure 6. Given the inverse square law,
 372 Equation 3 predicts $\frac{B_{max,Venus}}{B_{max,Mars}} \simeq \frac{1.5\text{AU}}{0.7\text{AU}} \simeq 2.1$. However, the observed ratio is only 1.2
 373 if using the means of the distributions (77.8 nT/ 62.9 nT), or 1.4 if using the medians (75.7
 374 nT/ 55.7 nT). If we account for the crustal field component at Mars, that is at most 20%
 375 of B_{max} (in most cases is less than 10% of B_{max}), then the observed ratio is at most 1.75
 376 ($1.4/0.8$), still implying the observed ratio is smaller than the prediction of 2.2.

377 To explore why the ratio is smaller than predicted, Figure 6B shows a comparison
 378 of the observed and predicted B_{max} . In particular, the histograms show the ratio between
 379 the observed B_{max} and the predicted B_{max} for each profile. Only observations with SZA
 380 $< 60^\circ$ are included. The Venus ratios are usually less than one, having a mean of 0.66

(± 0.22) nT. A possible explanation is that Equation 3 relies on two assumptions: (1) pressure balance throughout the space environment and (2) the ionospheric thermal pressure is negligible compared to the magnetic pressure. At Venus, the second assumption is often not satisfied (Luhmann et al., 1987) leading to a reduction in the induced field strength via Equation 2.

At Mars, the ratios are usually greater than one, with a mean of 1.38 (± 0.22) nT. If we consider a 20% crustal field component, the mean would decrease to at least 1.1, still implying the induced field strengths at Mars are somewhat larger than predicted by Equation 3. Since the second assumption is usually satisfied at Mars (Holmberg et al., 2019; Chu et al., 2021; Sánchez-Cano et al., 2020), it might be expected that Equation 3 is a good predictor of the maximum induced field strength. A possible explanation for why B_{max} is usually larger than the prediction is the presence of small-scale features in the magnetic field profile. These small scale features are much more prevalent at Mars than at Venus. They result in small-scale spikes and bumps that can lead to a higher B_{max} than predicted. These small scale structures arise from a variety of processes, such as waves, rotations, plasma instabilities (Hamil et al., 2022; Cravens et al., 2023).

Lastly, Figure 6c shows histograms of the altitude where B_{max} is observed. At Venus, the altitude of the low-altitude maximum induced field, when magnetized, is consistently around 170 km. There are rarer cases where the altitude of B_{max} is much higher, including a number of profiles with the altitude bin in the highest histogram bin near 250 km. These are the edge cases discussed in Section 3.3 and are profiles similar to Figure 3E. The peak altitude at Mars is typically between 160-200 km, but the distribution is much wider than the distribution at Venus. The distribution is likely wider because of seasonal variations in the upper atmosphere of Mars, which causes constant pressure levels to rise and fall over the year owing to the changing insolation from Mars' elliptical orbit.

3.4 Solar Wind Dynamic Pressure

It is expected that with increasing solar wind pressure, the induced field strength will increase. Assuming pressure balance across the magnetic pileup boundary and into the ionosphere, and negligible ionospheric thermal pressure, the induced field strength should vary as the square root of the solar wind dynamic pressure (Eq. 3). Previous work has shown that the magnetic field at the MPB does respond in this manner to solar wind dynamic pressure variations (Crider et al., 2003; Xu et al., 2021). Below the MPB, we still expect the induced field to increase with increasing dynamic pressure because the fields at the MPB are convected downward into the ionosphere.

Figure 7 shows the dependence B_{max} on solar wind dynamic pressure. The magnetized Venus data, and the Mars data, are corrected to the subsolar point by dividing them by $\cos(\theta)$ (see Section 3.2). The plot only contains data with $\text{SZA} < 60^\circ$. We fit a power law to the observations: $B_{max} = B_0 P_{sw}^n$ where B_0 is the best-fit subsolar B_{max} and n is the best-fit exponent. B_{max} increases with solar wind pressure for both Venus (when magnetized) and Mars with power law exponents $n = 0.57 \pm 0.13$ and $n = 0.45 \pm 0.02$ respectively. These are consistent with each other within error, however the Venus fit has significant uncertainty due to having much fewer data points and a more narrow range of solar wind pressure coverage compared to Mars. The R-squared value of the fits is 0.2 for Venus (magnetized) and 0.6 for Mars.

The coefficient B_0 of the power law fit for Venus (magnetized) is 27.7 ± 6.1 whereas the coefficient for Mars is 65.2 ± 0.7 . This implies that for a solar wind pressure of 1 nPa, Mars would have a higher induced field, which is expected since Venus tends to exclude the external magnetic field more effectively than Mars (consistent with figure 6c). However, Venus is more likely to experience higher solar wind dynamic pressure since it is closer to the Sun. As a result, the average B_{max} for Venus (when magnetized) is higher than at Mars (see Section 3.3).

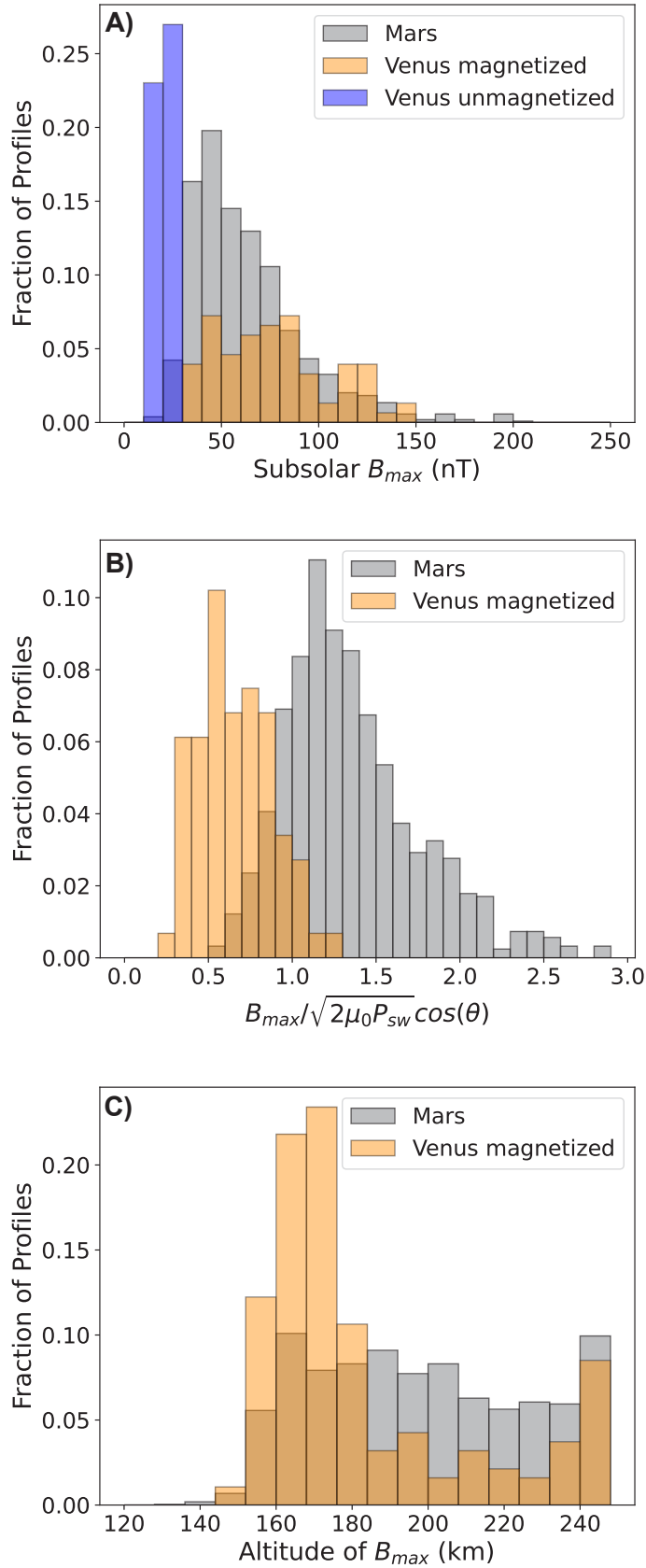


Figure 6: (A) Histograms of B_{max} , the maximum low-altitude field strength. (B) Ratios of the observed B_{max} and the B_{max} predicted by Equation 3. (C) Histograms of the altitude of B_{max} .

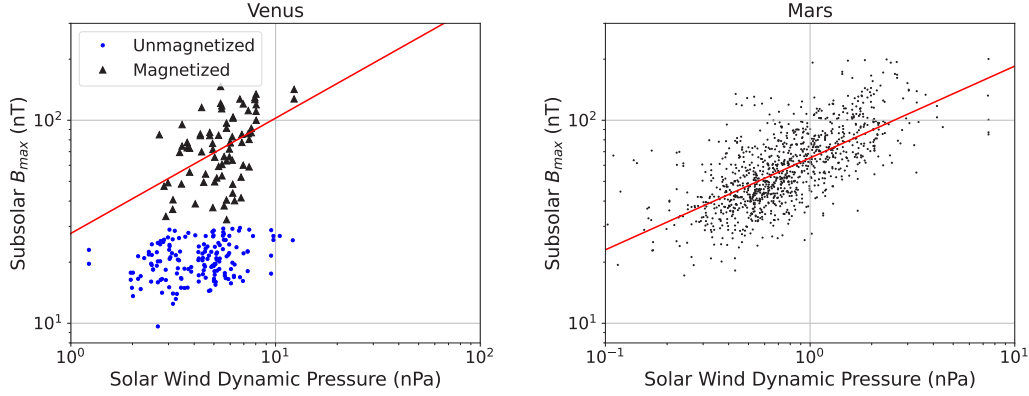


Figure 7: The variation of B_{max} with solar wind dynamic pressure for Venus (left) and Mars (right). For Venus, values derived from magnetized profiles are plotted as black triangles and values derived from unmagnetized profiles are plotted as blue circles. The red lines are power law fits with derived exponents of 0.57 ± 0.13 for Venus (magnetized) and 0.45 ± 0.02 for Mars.

432 The induced field strength of the unmagnetized ionosphere of Venus has virtually
 433 no dependence on solar wind dynamic pressure. The best-fit exponent is zero and the
 434 R-squared value is 0.01. This lack of dependence on solar wind pressure is expected be-
 435 cause, when unmagnetized, the solar wind magnetic field is excluded from low altitudes
 436 by the ionospheric thermal pressure.

437 4 Discussion and Conclusions

438 In this study, we compare low-altitude induced magnetic fields at Venus and Mars.
 439 Our main results are as follows:

- 440 1. The magnetic field profiles at Venus and Mars have different altitude structures.
 441 The magnetized profiles at Venus have distinct, identifiable features, namely a peak
 442 in magnetic field around 170 km, a wide minimum around 200 km, and a nearly
 443 constant topside above 250 km. But the Mars profiles lack these distinct, repeat-
 444 able large-scale features that would allow them to be classified into magnetized
 445 and unmagnetized categories like Venus.
- 446 2. The maximum low-altitude magnetic field strength (B_{max}) in the unmagnetized
 447 ionosphere of Venus has no dependence on SZA. The B_{max} in the magnetized iono-
 448 sphere of Venus, and the B_{max} at Mars, have a SZA dependence where $B_{max} \propto$
 449 $\cos(\theta)$ where θ is the angle between the solar wind velocity and the MPB normal
 450 vector (Eq. 3). However, at both planets, B_{max} is larger near the terminator than
 451 this trend predicts.
- 452 3. The mean Venus B_{max} (77.8 nT) is greater than the mean Mars B_{max} (62.9 nT)
 453 which is expected since Venus is exposed to higher solar wind pressures. When
 454 comparing B_{max} with the prediction from Eq. 3 — which is derived assuming pres-
 455 sure balance is maintained and $P_{th} \ll P_B$ — the B_{max} at Venus (magnetized)
 456 is lower than predicted by a factor of 0.66. The B_{max} at Mars, alternatively, is
 457 higher than predicted by a factor between 1.1 and 1.38.
- 458 4. When unmagnetized, Venus B_{max} has no dependence on solar wind dynamic pres-
 459 sure (P_{sw}). When magnetized, Venus B_{max} has a dependence of $B_{max} \propto (P_{sw})^{0.57 \pm 0.13}$,
 460 which is potentially consistent with the prediction from Equation 3 of an expo-

461 nent of 0.5. However, the fit is poor and the dynamic pressure can only account
 462 for 20% of the variation in B_{max} . The Mars B_{max} , in contrast, has a dependence
 463 of $B_{max} \propto (P_{sw})^{0.45 \pm 0.02}$, and the dynamic pressure can account for 60% of the
 464 variation in B_{max} .

465 The vertical structure of the magnetic field profiles at Mars is highly varied and
 466 inconsistent, in contrast with the Venus profiles which tend to have the same recurring
 467 large-scale features. A likely explanation is the ubiquitous presence of small-scale struc-
 468 tures in the magnetic field profiles at Mars, which are much less common in the mag-
 469 netized ionosphere of Venus. This explanation was also put forth by Huang et al. (2023)
 470 to explain the varied magnetic field profiles at Mars. They attributed the varied struc-
 471 tures to time-dependent variations in the up stream solar wind, such as variations in the
 472 solar wind dynamic pressure. The vertical structure of the Venus magnetic field profiles
 473 can be successfully reproduced by models, even under steady solar wind conditions (Luhmann
 474 et al., 1984; Cravens et al., 1984; Shinagawa & Cravens, 1988; Luhmann & Cravens, 1991).
 475 However, models have been less successful at reproducing the vertical structure of the
 476 Mars profiles. Additional physical processes likely need to be included to capture the small-
 477 scale structures (Hamil et al., 2022; Cravens et al., 2023).

478 We find both similarities and differences between the low-altitude magnetic field
 479 strengths. The main similarity arises between Mars and the magnetized ionosphere of
 480 Venus, providing further evidence that the ionosphere of Mars is magnetized most of the
 481 time (Sánchez-Cano et al., 2020). In particular, the low-altitude field strengths have the
 482 same SZA dependence, including higher than expected fields near the terminator. Fur-
 483 ther, at both planets the SZA variation of the low-altitude field strengths are modeled
 484 best when the angle between solar wind velocity and the normal vector of the MPB is
 485 used in Equation 3 (as opposed to SZA). In other words, since the low-altitude magnetic
 486 fields are convected downward from the MPB (Equation 1), the shape of the MPB con-
 487 trols how the strength of the low-altitude induced fields vary across the dayside iono-
 488 sphere.

489 Major differences include higher induced field strengths in the magnetized ionosphere
 490 of Venus (means of 77.8 nT vs. 62.9 nT), which is expected given Venus is exposed to
 491 higher solar wind dynamic pressures due to its proximity to the Sun. Additionally, when
 492 magnetized, the low-altitude field at Venus is weaker than predicted under the assump-
 493 tions of pressure balance and $P_{th} \ll P_B$ (Eq. 3). This is consistent with the fact that
 494 the assumption of $P_{th} \ll P_B$ is often unsatisfied at Venus because the ionospheric ther-
 495 mal pressure is often comparable to or greater than the solar wind dynamic pressure, es-
 496 pecially during the PVO observations at solar maximum (Luhmann, 1986; Zhang & Luh-
 497 mann, 1992). Consequently, the induced magnetic pressure does not have to be as large
 498 as the solar wind pressure to achieve pressure balance (Eq. 2).

499 In contrast, on Mars, low-altitude field strengths are higher than predicted by Equa-
 500 tion 3, even after accounting for possible contributions from crustal fields. One possi-
 501 ble explanation is again related to small scale features that are common at Mars but not
 502 at Venus. These observed small scale features may be either spatial (Hamil et al., 2022)
 503 or temporal (Huang et al., 2020) variations, and are likely driven by processes such as
 504 varying solar wind conditions, large-scale plasma dynamics, plasma instabilities, or cur-
 505 rent sheets (Hamil et al., 2022). The small scale features, such as the localized layers seen
 506 in Figure 4E, can increase the maximum low-altitude field strength so that is larger than
 507 predicted by Equation 3.

508 The increased presence of small-scale structures at Mars may be related to the con-
 509 vection and diffusion timescales, which characterize the time for the low-altitude induced
 510 fields to form and dissipate (Eq. 1). Recent calculations suggest the convection and dif-
 511 fusion timescales are on the order of a few hours at Venus (Y. Ma et al., 2020), but only
 512 on the order of tens of minutes at Mars (Huang et al., 2020). Given the timescales at

Mars can be shorter than the time it takes for MAVEN complete a low-altitude peria-
 sis pass (~ 10 minutes), it is possible some of the observed small-scale features are caused
 by temporal variations in the upstream solar wind, as suggested by Huang et al. (2020).
 However, these calculations are somewhat uncertain because they are strongly controlled
 by vertical plasma velocities, which are small (tens of m/s) and have not been directly
 measured (Y. Ma et al., 2020).

Taken together, our results reveal some interesting similarities and differences be-
 tween the induced magnetic fields at Venus and Mars. They point to how planetary prop-
 erties, such as planet-Sun distance, can affect the structure and variability of induced
 fields at unmagnetized planets. Being closer to the Sun, Venus has a higher ionospheric
 thermal pressure that is often comparable to or greater than the solar wind dynamic pres-
 sure (at least at solar maximum during the PVO observations). Consequently, it exhibits
 a dichotomy of magnetized and unmagnetized states, and in each state the induced field
 strength has a different dependence on SZA and solar wind dynamic pressure. Mars, be-
 ing further from the Sun, has a lower ionospheric thermal pressure (from reduced solar
 EUV flux) and so the ionosphere is magnetized most of the time and does not exhibit
 a dichotomy of states. Further, the shape of the MPB controls the SZA variation of the
 induced fields at both planets, when in a magnetized state. This work focuses exclusively
 on weak crustal field regions at Mars, and future work focusing on strong crustal fields
 regions may reveal even more interesting differences between the low-altitude induced
 magnetic fields at Venus and Mars.

5 Open Research

The data used in this work are publicly archived. The Venus magnetometer data
 can be found at <https://pds-ppi.igpp.ucla.edu/search/view/?f=yes&id=pds://PPI/PVO-V-OMAG-4--SCCOORDS-24SEC-V2.0> and the Venus upstream solar wind data
 can be found at <https://cdaweb.gsfc.nasa.gov/cgi-bin/eval1.cgi>. The Mars Key
 Parameters data can be found at <https://lasp.colorado.edu/maven/sdc/public/data/sci/kp/> and the Mars upstream solar wind data can be found at <https://homepage.physics.uiowa.edu/~jhalekas/drivers.html>. The derived maximum low-altitude
 magnetic field strengths are publicly archived at <https://zenodo.org/uploads/10278080>
 for both Venus and Mars.

Acknowledgments

This work was supported by NASA grant 80NSSC21K0147 which was funded through
 the Solar System Workings program. S. Byrd received additional support from the NASA
 Iowa Space Grant Consortium and the John and Elsie Mae Ferentz Undergraduate Re-
 search Fund.

References

- Bertucci, C., Duru, F., Edberg, N., Fraenz, M., Martinecz, C., Szego, K., & Vais-
 berg, O. (2011). The induced magnetospheres of Mars, Venus, and Titan. *Space Sci. Rev.*, *162*, 113–171.
- Bowers, C. F., Slavin, J. A., DiBraccio, G. A., Poh, G., Hara, T., Xu, S., &
 Brain, D. A. (2021). MAVEN Survey of Magnetic Flux Rope Proper-
 ties in the Martian Ionosphere: Comparison With Three Types of For-
 mation Mechanisms. *Geophys. Res. Lett.*, *48*(10), e2021GL093296. doi:
<https://doi.org/10.1029/2021GL093296>
- Brace, L. H., & Kliore, A. J. (1991). The structure of the Venus ionosphere. *Space
 Sci. Rev.*, *55*, 81–163. doi: 10.1007/BF00177136
- Brain, D. A. (2003). Martian magnetic morphology: Contributions from the solar

- 561 wind and crust. *Journal of Geophysical Research*, 108(A12), 1424. doi: 10.
562 .1029/2002JA009482
- 563 Chu, F., Girazian, Z., Duru, F., Ramstad, R., Halekas, J., Gurnett, D. A., . . . Kopf,
564 A. J. (2021). The dayside ionopause of Mars: Solar wind interaction, pressure
565 balance, and comparisons with Venus. *Journal of Geophysical Research: Plan-*
566 *ets*, 126(11), e2021JE006936. doi: <https://doi.org/10.1029/2021JE006936>
- 567 Cloutier, P. A. (1984). Formation and dynamics of large-scale magnetic structures
568 in the ionosphere of Venus. *Journal of Geophysical Research: Space Physics*,
569 89(A4), 2401-2405.
- 570 Connerney, J. E. P., Acuña, M. H., Wasilewski, P. J., Kletetschka, G., Ness, N. F.,
571 Rème, H., . . . Mitchell, D. L. (2001). The global magnetic field of Mars
572 and implications for crustal evolution. *Geophysical Research Letters*, 28(21),
573 4015–4018. doi: 10.1029/2001GL013619
- 574 Cravens, T. E., Hamil, O., Renzaglia, A., Ledvina, S. A., & Howard, S. K. (2023).
575 Fourier analysis of magnetic fields in the ionosphere of Mars. *Journal of Geo-*
576 *physical Research: Space Physics*, 128(4), e2022JA031044.
- 577 Cravens, T. E., Shinagawa, H., & Nagy, A. F. (1984). The evolution of large-scale
578 magnetic fields in the ionosphere of Venus. *Geophysical Research Letters*,
579 11(3), 267–270. doi: 10.1029/GL011i003p00267
- 580 Crider, D. H., Vignes, D., Krymskii, A. M., Breus, T. K., Ness, N. F., Mitchell,
581 D. L., . . . Acuña, M. H. (2003). A proxy for determining solar wind dynamic
582 pressure at Mars using Mars Global Surveyor data. *J. Geophys. Res.*, 108,
583 1461, 10.1029/2003JA009875. doi: 10.1029/2003JA009875
- 584 Daniell Jr, R., & Cloutier, P. (1977). Distribution of ionospheric currents induced
585 by the solar wind interaction with Venus. *Planetary and Space Science*, 25(7),
586 621–628.
- 587 Elphic, R. C., Brace, L. H., Theis, R. F., & Russell, C. T. (1984). Venus dayside
588 ionospheric conditions - Effects of ionospheric magnetic field and solar EUV
589 flux. *Geophys. Res. Lett.*, 11, 124–127. doi: 10.1029/GL011i002p00124
- 590 Elphic, R. C., & Russell, C. T. (1983). Magnetic flux ropes in the Venus ionosphere:
591 Observations and models. *Journal of Geophysical Research: Space Physics*,
592 88(A1), 58-72. doi: 10.1029/JA088iA01p00058
- 593 Elphic, R. C., Russell, C. T., Slavin, J. A., & Brace, L. H. (1980). Observations
594 of the dayside ionopause and ionosphere of Venus. *Journal of Geophysical Re-*
595 *search*, 85(A13), 7679. doi: 10.1029/JA085iA13p07679
- 596 Espley, J. R. (2018). The martian magnetosphere: Areas of unsettled terminol-
597 ogy. *Journal of Geophysical Research: Space Physics*, 123(6), 4521-4525. doi:
598 10.1029/2018JA025278
- 599 Fang, X., Ma, Y., Luhmann, J., Dong, Y., Brain, D., Hurley, D., . . . Jakosky, B.
600 (2018). The Morphology of the Solar Wind Magnetic Field Draping on the
601 Dayside of Mars and Its Variability. *Geophysical Research Letters*, 45(8),
602 3356–3365. doi: <https://doi.org/10.1002/2018GL077230>
- 603 Fang, X., Ma, Y., Luhmann, J., Dong, Y., Halekas, J., & Curry, S. (2023). Mars
604 global distribution of the external magnetic field and its variability: Maven
605 observation and MHD prediction. *Journal of Geophysical Research: Space*
606 *Physics*, 128(9), e2023JA031588. doi: 10.1029/2023JA031588
- 607 Halekas, J. S., Ruhunusiri, S., Harada, Y., Collinson, G., Mitchell, D. L., Mazelle,
608 C., . . . Jakosky, B. M. (2017, January). Structure, dynamics, and seasonal
609 variability of the Mars-solar wind interaction: MAVEN Solar Wind Ion An-
610 alyzer in-flight performance and science results. *Journal of Geophysical Re-*
611 *search: Space Physics*, 122(1), 547–578. doi: 10.1002/2016JA023167
- 612 Hamil, O., Cravens, T. E., Renzaglia, A., & Andersson, L. (2022). Small scale
613 magnetic structure in the induced martian ionosphere and lower magnetic
614 pile-up region. *Journal of Geophysical Research: Space Physics*, 127(4),
615 e2021JA030139. doi: <https://doi.org/10.1029/2021JA030139>

- 616 Holmberg, M. K. G., André, N., Garnier, P., Modolo, R., Andersson, L., Halekas,
617 J., ... Mitchell, D. L. (2019). MAVEN and MEX Multi-instrument Study
618 of the Dayside of the Martian Induced Magnetospheric Structure Revealed by
619 Pressure Analyses. *Journal of Geophysical Research: Space Physics*, *124*(11),
620 8564–8589. doi: 10.1029/2019JA026954
- 621 Huang, J.-P., Cui, J., Hao, Y.-Q., Guo, J.-P., Wu, X.-S., Niu, D.-D., & Wei, Y.
622 (2020). Solar and Magnetic Control of Minor Ion Peaks in the Dayside Mar-
623 tian Ionosphere. *Journal of Geophysical Research: Space Physics*, *125*(8),
624 e2020JA028254. doi: <https://doi.org/10.1029/2020JA028254>
- 625 Huang, J.-P., Hao, Y.-Q., Lu, H.-Y., & Cui, J. (2023). Variability of draped inter-
626 planetary magnetic field in the subsolar martian ionosphere. *The Astrophysical*
627 *Journal*, *955*(1), 48.
- 628 Intriligator, D. S., Wolfe, J. H., & Mihalov, J. D. (1980, January). The Pi-
629 oneer Venus Orbiter Plasma Analyzer Experiment. *IEEE Transactions*
630 *on Geoscience and Remote Sensing*, *GE-18*(1), 39–43. doi: 10.1109/
631 TGRS.1980.350258
- 632 Jakosky, B. M., Lin, R. P., Grebowsky, J. M., Luhmann, J. G., Mitchell, D. F., Beu-
633 telschies, G., ... Zurek, R. (2015, December). The Mars Atmosphere and
634 Volatile Evolution (MAVEN) Mission. *Space Science Reviews*, *195*(1-4), 3–48.
635 doi: 10.1007/s11214-015-0139-x
- 636 Kar, J., & Mahajan, K. K. (1987). On the response of ionospheric magnetisation
637 to solar wind dynamic pressure from pioneer venus measurements. *Geophysical*
638 *Research Letters*, *14*(5), 507–510. doi: 10.1029/GL014i005p00507
- 639 Lee, C. O., Hara, T., Halekas, J. S., Thiemann, E., Chamberlin, P., Eparvier, F.,
640 ... Jakosky, B. M. (2017, March). MAVEN observations of the solar cycle
641 24 space weather conditions at Mars. *Journal of Geophysical Research: Space*
642 *Physics*, *122*(3), 2768–2794. doi: 10.1002/2016JA023495
- 643 Luhmann, J. G. (1986, September). The solar wind interaction with Venus. *Space*
644 *Science Reviews*, *44*(3), 241–306. doi: 10.1007/BF00200818
- 645 Luhmann, J. G., & Cravens, T. E. (1991). Magnetic fields in the ionosphere of
646 Venus. *βr*, *55*, 201–274. doi: 10.1007/BF00177138
- 647 Luhmann, J. G., Elphic, R. C., Russell, C. T., Mihalov, J. D., & Wolfe, J. H. (1980,
648 November). Observations of large scale steady magnetic fields in the dayside
649 Venus ionosphere. *Geophysical Research Letters*, *7*(11), 917–920. doi: 10.1029/
650 GL007i011p00917
- 651 Luhmann, J. G., Ledvina, S. A., & Russell, C. T. (2004). Induced magneto-
652 spheres. *Advances in Space Research*, *33*(11), 1905–1912. doi: 10.1016/
653 j.asr.2003.03.031
- 654 Luhmann, J. G., & Russell, C. T. (1983). Magnetic fields in the ionospheric holes
655 of venus: Evidence for an intrinsic field? *Geophysical Research Letters*, *10*(5),
656 409–411. Retrieved from [https://agupubs.onlinelibrary.wiley.com/
657 doi/abs/10.1029/GL010i005p00409](https://agupubs.onlinelibrary.wiley.com/doi/abs/10.1029/GL010i005p00409) doi: [https://doi.org/10.1029/
658 GL010i005p00409](https://doi.org/10.1029/
658 GL010i005p00409)
- 659 Luhmann, J. G., Russell, C. T., & Elphic, R. C. (1984). Time scales for the de-
660 cay of induced large-scale magnetic fields in the venus ionosphere. *Journal of*
661 *Geophysical Research: Space Physics*, *89*(A1), 362–368. doi: [https://doi.org/10
662 .1029/JA089iA01p00362](https://doi.org/10.1029/JA089iA01p00362)
- 663 Luhmann, J. G., Russell, C. T., Scarf, F. L., Brace, L. H., & Knudsen, W. C.
664 (1987). Characteristics of the Marslike limit of the Venus-solar wind in-
665 teraction. *Journal of Geophysical Research*, *92*(A8), 8545. doi: 10.1029/
666 JA092iA08p08545
- 667 Ma, Y., Combi, M. R., Tenishev, V., Shou, Y., & Bougher, S. (2023). The effects
668 of the upper atmosphere and corona on the solar wind interaction with venus.
669 *Journal of Geophysical Research: Space Physics*, *128*(4), e2022JA031239.
670 (e2022JA031239 2022JA031239) doi: <https://doi.org/10.1029/2022JA031239>

- 671 Ma, Y., Toth, G., Nagy, A., Luhmann, J., & Russell, C. (2020). Formation and Evo-
 672 lution of the Large-Scale Magnetic Fields in Venus' Ionosphere: Results From
 673 a Three Dimensional Global Multispecies MHD Model. *Geophysical Research*
 674 *Letters*, *47*(11), e2020GL087593. doi: 10.1029/2020GL087593
- 675 Ma, Y. J., Fang, X., Nagy, A. F., Russell, C. T., & Toth, G. (2014). Martian iono-
 676 spheric responses to dynamic pressure enhancements in the solar wind. *J. Geo-*
 677 *phys. Res.*, *119*(2), 1272–1286. doi: 10.1002/2013JA019402
- 678 Ma, Y. J., Russell, C. T., Fang, X., Dong, C. F., Nagy, A. F., Toth, G., ... Jakosky,
 679 B. M. (2017). Variations of the Martian plasma environment during the ICME
 680 passage on 8 March 2015: A time-dependent MHD study. *J. Geophys. Res.*,
 681 *122*(2), 1714–1730. doi: 10.1002/2016JA023402
- 682 Morschhauser, A., Lesur, V., & Grott, M. (2014, June). A spherical harmonic
 683 model of the lithospheric magnetic field of Mars. *Journal of Geophysical Re-*
 684 *search: Planets*, *119*(6), 1162–1188. Retrieved 2019-12-04, from [http://](http://doi.wiley.com/10.1002/2013JE004555)
 685 doi.wiley.com/10.1002/2013JE004555 doi: 10.1002/2013JE004555
- 686 Phillips, J. L., Luhmann, J. G., & Russell, C. T. (1984a). Growth and maintenance
 687 of large-scale magnetic fields in the dayside Venus ionosphere. *Journal of*
 688 *Geophysical Research: Space Physics*, *89*(A12), 10676–10684. Retrieved from
 689 [https://agupubs-onlinelibrary-wiley-com.proxy.lib.uiowa.edu/doi/](https://agupubs-onlinelibrary-wiley-com.proxy.lib.uiowa.edu/doi/abs/10.1029/JA089iA12p10676)
 690 [abs/10.1029/JA089iA12p10676](https://agupubs-onlinelibrary-wiley-com.proxy.lib.uiowa.edu/doi/abs/10.1029/JA089iA12p10676) doi: 10.1029/JA089iA12p10676
- 691 Phillips, J. L., Luhmann, J. G., & Russell, C. T. (1984b). Growth and mainte-
 692 nance of large-scale magnetic fields in the dayside venus ionosphere. *Journal*
 693 *of Geophysical Research: Space Physics*, *89*(A12), 10676–10684. doi: 10.1029/
 694 [JA089iA12p10676](https://doi.org/10.1029/JA089iA12p10676)
- 695 Ramstad, R. (2020). The global current systems of the Martian induced magneto-
 696 sphere. *Nature Astronomy*, *4*, 7.
- 697 Ruhunusiri, S., Halekas, J. S., Espley, J. R., Eparvier, F., Brain, D., Mazelle, C., ...
 698 Jakosky, B. M. (2018). An Artificial Neural Network for Inferring Solar Wind
 699 Proxies at Mars. *Geophysical Research Letters*, *45*(20), 10,855–10,865. doi:
 700 [10.1029/2018GL079282](https://doi.org/10.1029/2018GL079282)
- 701 Russell, C., Luhmann, J., & Elphic, R. (1983). The properties of the low altitude
 702 magnetic belt in the venus ionosphere. *Advances in Space Research*, *2*(10), 13–
 703 16.
- 704 Russell, C. T., Snare, R. C., Means, J. D., & Elphic, R. C. (1980). Pioneer venus
 705 orbiter fluxgate magnetometer. *IEEE Transactions on Geoscience and Remote*
 706 *Sensing, GE-18*(1), 32–35. doi: 10.1109/TGRS.1980.350256
- 707 Shinagawa, H., & Cravens, T. E. (1988). A one-dimensional multispecies magneto-
 708 hydrodynamic model of the dayside ionosphere of Venus. *Journal of Geophys-*
 709 *ical Research*, *93*(A10), 11263. doi: 10.1029/JA093iA10p11263
- 710 Shinagawa, H., & Cravens, T. E. (1989, June). A one-dimensional multispecies
 711 magnetohydrodynamic model of the dayside ionosphere of Mars. *Journal*
 712 *of Geophysical Research: Space Physics*, *94*(A6), 6506–6516. Retrieved
 713 2019-12-04, from <http://doi.wiley.com/10.1029/JA094iA06p06506> doi:
 714 [10.1029/JA094iA06p06506](https://doi.org/10.1029/JA094iA06p06506)
- 715 Sánchez-Cano, B., Narvaez, C., Lester, M., Mendillo, M., Mayyasi, M., Holmstrom,
 716 M., ... Durward, S. (2020). Mars' ionopause: A matter of pressures. *Jour-*
 717 *nal of Geophysical Research: Space Physics*, *125*(9), e2020JA028145. doi:
 718 <https://doi.org/10.1029/2020JA028145>
- 719 Vignes, D., Mazelle, C., Rme, H., Acuña, M. H., Connerney, J. E. P., Lin, R. P.,
 720 ... Ness, N. F. (2000). The solar wind interaction with mars: Locations and
 721 shapes of the bow shock and the magnetic pile-up boundary from the obser-
 722 vations of the mag/er experiment onboard mars global surveyor. *Geophysical*
 723 *Research Letters*, *27*(1), 49–52. doi: <https://doi.org/10.1029/1999GL010703>
- 724 Xu, Q., Xu, X., Zhang, T. L., Rong, Z. J., Wang, M., Wang, J., ... Luo, L. (2021).
 725 The Venus Express observation of Venus' induced magnetosphere boundary

726 at solar maximum. *Astron. Astrophys.*, 652, A113. doi: 10.1051/0004-6361/
727 202141391
728 Zhang, M. H. G., & Luhmann, J. G. (1992). Comparisons of peak ionosphere pres-
729 sures at Mars and Venus with incident solar wind dynamic pressure. *J. Geo-*
730 *phys. Res.*, 97, 1017–1025. doi: 10.1029/91JE02721